

*OPERANDO* X-RAY ANALYSIS OF BATTERY MATERIALS

A Dissertation

Presented to the Faculty of the Graduate School

of Cornell University

in Partial Fulfillment of the Requirements for the Degree of

Doctor of Philosophy

by

Katharine Elizabeth Silberstein

August 2015

© 2015 Katharine Elizabeth Silberstein

# *OPERANDO* X-RAY ANALYSIS OF BATTERY MATERIALS

Katharine Elizabeth Silberstein, Ph.D.

Cornell University 2015

Batteries can store energy from alternative, intermittent sources via chemical reactions for later use in electronics, transportation, and grid load leveling. Most commercial rechargeable batteries are based on lithium ion intercalation into layered metal oxides, the mechanism of which is fairly well understood. To move forward in the development of novel electrode materials versus lithium, deeper insight into heretofore unexplored methods of charge storage must be gained. X-ray diffraction (XRD) and X-ray absorption spectroscopy (XAS) are invaluable techniques for studying the atomic structure of molecules, materials, and systems relevant to electrochemical energy storage. The broad purpose of this dissertation work is to observe and understand the structural changes that occur within materials that are cycled electrochemically in a lithium-ion battery (LIB).

A specially designed coin cell allows for the investigation of chemical changes as observed with X-rays within the LIB as a function of the state of charge. This cell design has been used to study germanium nanowire anodes and anthraquinone-based cathodes at the Cornell High Energy Synchrotron Source (CHESS). The fully assembled coin cell is aligned in the beamline and connected to a galvanostat. Powder X-ray diffraction patterns or X-ray absorption spectra are then collected at regular

intervals as lithium ions enter and leave the structure under operating battery conditions. The resultant data give insight to the complexity of the mechanisms of solid-state interactions with lithium ions, and the following chapters will expand upon this. Briefly, germanium nanowires lithiate heterogeneously, preferentially into amorphous regions, and their crystalline cores can be maintained for a few cycles if the voltage cutoff limit is kept above 0.3V vs. Li/Li<sup>+</sup>. Also, for the organic cathodes, reversible crystallographic changes are observed that demonstrate that structural reorganization occurs to accommodate the coordination of positive charge within a reduced molecular crystal. The original contribution to knowledge from this body of work is that crystalline domains need not be maintained in an electrochemically stable system. These and other in-depth mechanistic *operando* studies presented herein provide a unique view of dynamic battery systems and guide future investigations.

## BIOGRAPHICAL SKETCH

Katharine Silberstein was born in Buffalo, New York, as the youngest of three girls. She loved the snow, and was sad to leave it in 2000 when her family moved to central New Jersey. Thankfully, Katie adjusted well. She took leadership positions in many musical, literary, and academic extracurricular activities throughout her secondary education, and she graduated third in her high school class.

Katie then attended MIT, where she obtained an S.B. in chemistry with a minor in literature. While in college, Katie continued to be very involved in many groups, including her sorority Sigma Kappa and the MIT Wind Ensemble. After brief stints of research in the Field and Peters chemistry labs at MIT, Katie joined the Bawendi lab, where her work on quantum dot synthesis and characterization sparked her interest in pursuing a Ph.D. in chemistry. Immediately after graduation, Katie spent the summer at École Polytechnique in France studying metal phosphide nanoparticle catalysis. A mere 72 hours after returning to America, Katie moved to Ithaca to begin her graduate life at Cornell University.

The majority of her Ph.D. work has been focused on using *operando* X-ray absorption spectroscopy and X-ray diffraction to analyze molecules, materials, and systems relevant to lithium-ion batteries. Through this research, she has elucidated the molecular mechanisms that lead to bulk charge storage within novel materials.

Outside of lab, Katie plays the trumpet in the Ithaca Concert Band and enjoys reading and spending time with family and friends.

Dedicated to Mom, Dad, Steph, and Jenn

## ACKNOWLEDGEMENTS

There are several people without whom the work presented in this dissertation would not be possible. I would like to thank:

- Prof. Abruña for allowing me to join his group and conduct this research;
- My committee members, Profs. Brock and DiSalvo, for their intellectual support;
- Financial support through the CHESS grant numbers NSF DMR-936384 and DMR-1332208;
- Drs. Jacob Ruff, Darren Dale, Ken Finkelstein, and Detlef Smilgies for beamline support at CHESS;
- Dr. Michael Lowe for teaching me the ways of the synchrotron and Dr. Jie Gao the ways of battery assembly;
- My collaborators on the germanium project, Prof. Tobias Hanrath and Ben Richards;
- Dr. Weidong Zhou for synthesizing anthraquinone derivatives and Dr. Emil Lobkovsky for determining the single crystal structure of the electrocrystallization product;

- Prof. Serena DeBeer for helpful discussions about X-ray spectroscopy;
- My collaborators on the ionomer SAXS project, Johary Rivera-Melendez, Kristina Hugar, James McKone, and Jennifer Wierman;
- Rebecca Potash for assisting with *operando* coin cell preparation;
- My collaborator in life, James Pastore;
- All of my family and friends for their love and encouragement along the way.

## TABLE OF CONTENTS

BIOGRAPHICAL SKETCH	iii
DEDICATION	v
ACKNOWLEDGEMENTS	vi
TABLE OF CONTENTS	viii
LIST OF FIGURES	xii
CHAPTER 1: INTRODUCTION	
1-1. Motivation for Battery Research	1
1-2. Structure-Property Relationships	3
1-3. <i>Operando</i> Methods – Pros and Cons	4
1-4. Dissertation Overview	5
CHAPTER 2: EXPERIMENTAL METHODS	
2-1. Electrochemical Techniques	8
2-2. Film Preparation	8
2-3. X-Ray Methods	10
2-4. Software	14

CHAPTER 3: ELECTROCHEMICAL LITHIATION-INDUCED  
POLYMORPHISM OF ANTHRAQUINONE DERIVATIVES OBSERVED BY  
OPERANDO X-RAY DIFFRACTION

3-1. Introduction	16
3-2. Experimental Details	19
3-3. Results	24
3-4. Discussion	31
3-5. Conclusions	32

CHAPTER 4: EX-SITU APPROACHES TO ISOLATE ANTHRAQUINONE'S  
LITHIATED PHASE

4-1. Introduction	36
4-2. Experimental Details	37
4-3. Results	40
4-4. Discussion	46
4-5. Conclusions	47

CHAPTER 5: *OPERANDO* X-RAY SCATTERING AND SPECTROSCOPIC ANALYSIS OF GERMANIUM NANOWIRE ANODES IN LITHIUM-ION BATTERIES

5-1. Introduction	49
5-2. Experimental Details	52
5-3. Results	58
5-4. Discussion	72
5-5. Conclusions	75

CHAPTER 6: EXPERIMENTAL AND CALCULATED X-RAY ABSORPTION ANALYSIS OF LITHIUM-SULFUR SPECIES TO SUPPORT *OPERANDO* STUDIES

6-1. Introduction	78
6-2. Experimental Details	79
6-3. Results	80
6-4. Discussion	84
6-5. Conclusions	85

## CHAPTER 7: APPLICATION OF X-RAY METHODS TO CHARACTERIZE ENERGY STORAGE MATERIALS IN GENERAL

7-1. Introduction	87
7-2. Lithium Vanadium Oxide Insertion	87
7-3. Cerium Dioxide Lattice Strain	92
7-4. Small-Angle X-Ray Scattering of Ionomer Films	96
7-5. Collaborative Synchrotron Efforts	101

## CHAPTER 8: CONCLUSIONS AND FUTURE WORK

8-1. Organics	104
8-2. Inorganics	105
8-3. Publications	106

## LIST OF FIGURES

**Figure 2-1:** Exploded schematic of a 2032 coin cell modified for *operando* X-ray measurements.

10

**Figure 2-2:** Flow of *operando* XRD data workup.

12

**Figure 3-1:** Cyclic voltammograms of anthraquinone derivatives under investigation.

21

**Figure 3-2:** Galvanostatic cycling of anthraquinone derivatives under investigation.

22

**Figure 3-3:** Galvanostatic cycling of DCAQ with different sets of diffraction peaks labeled as described in the preceding paragraph.

25

**Figure 3-4:** Galvanostatic cycling of DCAAQ.

27

**Figure 3-5:** Diffraction patterns from DCIAQ powder, background, and cell.

28

**Figure 3-6:** Galvanostatic cycling of DCIAQ.

29

**Figure 3-7:** Galvanostatic cycling AQ with voltage held at 1.7V vs Li/Li<sup>+</sup> at the end.

30

**Figure 4-1:** Electrocrystallization chronopotentiometry vs Ag/Ag<sup>+</sup>.

39

**Figure 4-2:** Reaction schematic of chemical reduction of anthraquinone.

39

**Figure 4-3:** Powder XRD patterns of AQ that had been in contact with a lithium source.

41

**Figure 4-4:** XRD pattern of sample that had been held at low voltage with AQ plotted beneath to indicate which peaks remained from AQ (background scatter from glass capillary).

42

**Figure 4-5:** Powder XRD comparison of the pattern that arises at low voltages in a battery; AQ; and the electrocrystallized product.

43

**Figure 4-6:** Single crystal structure of electrocrystallization product as **(A)** a single entity with the perchlorate ion in proximity and **(B)** as a linear chain.

44

**Figure 4-7:** Demonstration of the significant change in packing between **(A)** the electrocrystallization product and **(B)** AQ, both displayed along the a-axis.

45

**Figure 4-8:** Comparison of XRD patterns from chemically reduced AQ and the known diffraction pattern of AQ.

46

**Figure 5-1:** Scanning electron micrograph of as-prepared germanium nanowires.

52

**Figure 5-2:** Raman scattering from a sample of Ge nanowires.

53

**Figure 5-3:** Transmission electron micrograph of a single germanium nanowire, illustrating the amorphous shell and crystalline core of the wires.

54

**Figure 5-4:** Overlaid EXAFS data in k-space,  $k^2$ -weighted, for full discharge. Each colored line is a different spectrum. Fourier transformation was carried out on data from  $k=3.000$  to  $9.983$  since the data become noisy after  $k=10$ .

56

**Figure 5-5:** Selected Ge K-edge XANES spectra from the cell cycled to  $0.01V$ , illustrating the shift in the absorption edge and in the “white line” peak position. The scan number for each XANES spectrum is consistent with the EXAFS spectra in Figure 15-14B.

57

**Figure 5-6:** Second derivative of selected Ge K-edge absorption spectra from the cell cycled to 0.01V. Each  $E_0$  was selected from its  $y = 0$  intercept. The scan number for each spectrum is consistent with the EXAFS spectra in Figure 15-14B.

57

**Figure 5-7: (A)** Ge(111) peak at the beginning and end of a 60mA/g rate discharge. **(B)** Intensity of Ge(111) peak plotted with the corresponding discharge profile at 100mA/g rate.

59

**Figure 5-8: (A)** XRD data for a germanium nanowire battery over the course of a full discharge/charge cycle. **(B)** Corresponding voltage profile. **(C)** Calculated XRD patterns of known Ge-Li alloy phases.

62

**Figure 5-9:** XRD patterns of germanium nanowire battery over the course of two full discharge/charge cycles.

63

**Figure 5-10:** Phase analysis of each diffraction pattern from two full discharge/charge cycles. Dashed lines indicate the points at which the voltage reaches its minimum throughout the cycling. The electrochemistry is the same as in Figure 5-9.

64

**Figure 5-11:** XRD patterns for a germanium nanowire battery over the course of two discharge/charge cycles to 0.3V showing the persistence of the Ge diffraction peaks.

66

**Figure 5-12:** Phase analysis of each diffraction pattern over the course of two discharge/charge cycles to 0.3V. The lithiated phases are presented on an expanded scale. Dashed lines indicate the points at which the voltage reaches its minimum throughout the cycling. The electrochemistry is the same as in Figure 5-11.

67

**Figure 5-13:** Fourier-transformed EXAFS region at Ge K-edge over the course of a full discharge/charge cycle at current densities of **(A)** 100mA/g and **(B)** 143 mA/g.

69

**Figure 5-14:** Fourier-transformed EXAFS region at Ge K-edge over the course of **(A)** the initial and **(B)** two successive discharge/charge cycles to 0.3V.

70

**Figure 5-15:**  $E_{\max}$  (black),  $E_0$  (red), and cell potential (blue) of the XANES region corresponding to the absorption spectra that contributed to **(A)** Figure 15-13B and **(B)** Figure 15-14B, respectively.

71

**Figure 5-16:** Extended galvanostatic cycling data with voltage cutoff ranges of 3V to **(A)** 0.01V and **(B)** 0.3V.

72

**Figure 6-1:** XANES spectra of binary mixtures of  $\text{Li}_2\text{S}$  and  $\text{S}_8$  powders.

81

**Figure 6-2:** XANES spectra of 1M mixtures of  $\text{Li}_2\text{S}$  and  $\text{S}_8$  powders in TEGDME.

82

**Figure 6-3:** **(A)** Calculated XANES spectra of  $\text{S}_2^-$  (blue)  $\text{S}_2^{2-}$  (red), **(B)**  $\text{S}_3^-$  (green), and  $\text{S}_3^{2-}$  (purple) species.

83

**Figure 6-4:** Calculated XANES spectra of the  $\text{S}_2^{2-}$  (blue),  $\text{S}_3^{2-}$  (red), and  $\text{S}_4^{2-}$  (green) species.

84

**Figure 7-1:** *Operando* XRD of  $\text{Li}_3\text{VO}_4$  battery cycling to 0V vs  $\text{Li}/\text{Li}^+$  at 0.1C.

89

**Figure 7-2:** Zoomed-in region of *operando* XRD of  $\text{Li}_3\text{VO}_4$  battery cycled to 0V versus  $\text{Li}/\text{Li}^+$  at 1C.

90

**Figure 7-3:** *Operando* XRD of  $\text{Li}_3\text{VO}_4$  discharged and then held at 0V versus Li.

91

**Figure 7-4:** Peak assignment of the first (black pattern, green lines) and last (red pattern, blue lines) scan of Figure 7-3, based on the cell parameters reported above.

91

**Figure 7-5:** Shifts as a function of state-of-charge for **(A)** the  $\text{Li}_3\text{VO}_4$  (101) peak and **(B)** the Cu (111) peak.

93

**Figure 7-6:** *Operando* XRD of CeO<sub>2</sub> powder on copper foil.  
95

**Figure 7-7:** Sequential phase fraction analysis of CeO<sub>2</sub> with lattice-expanded Li<sub>x</sub>CeO<sub>2</sub>.  
95

**Figure 7-8:** 1D plots of SAXS data from **(A)** phosphonium and **(B)** ammonium freestanding ionomer membranes.  
98

**Figure 7-9:** SAXS plots in d-spacing of freestanding membranes of ammonium ionomer and Nafion (inset) with differing pretreatments.  
99

**Figure 7-10:** GISAXS plots, in Q-spacing, of *in situ* hydration of ionomer thin films of ammonium and Nafion (inset) as a function of increasing time/degree of water uptake.  
100

## CHAPTER 1

### INTRODUCTION TO DISSERTATION

#### **1-1. Motivation for Battery Research**

Considering the geopolitical push to more environmentally-benign methods of electricity generation, there is an equal drive to improve energy storage technology. With many alternative, intermittent energy generation technologies such as solar cells, wind turbines, and hydroelectric plants, we need a way to capture and redeliver the electricity when the sun is not shining, the wind is not blowing, or the water is not flowing. We have to keep the electrons flowing! Batteries are therefore important for large-scale grid applications to support a non-fossil fuel-based economy.

Also, batteries keep us running. Modern man cannot survive (or at least it seems) without portable electronics. Everyone is glued to phones, tablets, MP3 players, laptops. Hearing aids, pacemakers, and other medical devices improve the quality of life. Developments in battery-powered transportation are exciting. If electrical energy could not be stored in chemical bonds or electrochemical double layers, we would be in a very tough position. Because batteries are so prevalent in daily life, they must be safe, inexpensive, and durable.

Lithium has been the anode material of choice in recent years because it has the most reducing potential of all metals. It is light and relatively abundant. The issue of dendrite formation as a safety problem is being investigated in some chemical

engineering laboratories. To overcome or to avoid dealing with it, battery manufacturers pre-lithiate graphitic carbon to avoid having metallic lithium in the cell. Intercalation processes are generally non-stoichiometric and do not disturb extant planarity<sup>1</sup>. For ideal capacity, one would use lithium foil as an infinite reservoir. Lithiated metal oxides, such as  $\text{LiCoO}_2$  and  $\text{LiMn}_2\text{O}_4$ , are the workhorse cathode materials. Their mechanism of charge storage – lithium (de)intercalation – is fairly well understood. To further the development of next-generation lithium-ion batteries, we must investigate and understand new classes of materials.

Organic small molecules can cover points of concern of cost, safety, and durability. If we could gain a better understanding of how they change structure under electrochemical conditions, we could use synthetic methods to modify the starting structure for a better-working organic battery. The  $\text{Li}^+$  cation has very rich complexation chemistry and is most likely to coordinate with  $\text{O}^2$ .

Nanoscale materials are also of interest for use in batteries because there may be real benefit for using very small particles in electrode materials. Processing could be streamlined, and properties not present or evident in the bulk could be accessed, especially the accommodation of stress and strain due to the high aspect ratio. Silicon and germanium nanowires are popular because of their high theoretical capacity.

The lithium-sulfur system is of interest because of its low cost. The electrochemical reaction mechanism is complicated with several comproportionation reactions of different polysulfide species. To tease out the chemical identity of the

intermediate species, we can study standards and correlate to the signals we obtain. Computational methods also lend some validity to our assignments of features.

## **1-2. Structure-Property Relationships**

Lithium-ion batteries (LIBs) are nearly ubiquitous in the portable energy storage landscape. Despite great advances, many of the mechanistic details of charge storage processes remain elusive. Our interests lie in understanding what is occurring, at the atomic/molecular scales, that leads to the macroscopic property of charge storage.

Thinking about molecules without relation to surroundings is not the best way to understand a system. Atoms and molecules have certain structures, and when they pack together, they make bigger structures. We care about how and why higher-order structures form and what their implications are in terms of bulk characteristics. Deeper physical understanding of these materials will allow for their use in the design of more efficient devices.

There are many routes by which to relate molecular structure to bulk electrochemical properties. Computationally, one can determine the theoretical electrochemical potential of a certain molecule's redox reactions. One can also apply a constant current or voltage (and measure the output voltage or current, respectively) while collecting other data to relate the information to the state of charge. Such

techniques include NMR, Raman/infrared spectroscopy, and X-ray scattering/spectroscopy.

Using my unique blend of interests, I have embarked on a structural study of materials at the forefront of battery research using X-ray techniques in order to shed some light on the mechanistic details of charge storage at the cathode and anode in organic and inorganic systems and to uncover nonlinear correlations between property and structure. Our predictive methods focus on species in solution via cyclic voltammetry or in vacuum via computation. To better understand the mechanism of charge storage, we must probe inside of a working electrochemical cell.

### **1-3. *Operando* X-Ray Methods**

Here at Cornell, we have a synchrotron in our backyard that generates high energy X-rays with sub-angstrom wavelengths that interact with atoms and molecules. X-rays, therefore, have been our probe of choice for interrogating battery systems. By collecting diffraction and absorption data as a battery cycles, we can track metastable intermediates and phase transitions in real time as a function of state-of-charge.

In Young's double-slit experiment, human intervention collapsed the wave-particle duality of light into one distinct form. By observing the phenomenon, they changed the result. In *operando* methods, there is always the concern that such an occurrence is possible. Really, there is no way to prove or disprove it. The only option we have is to keep observing and comparing to other methods to ensure consistency.

## 1-4. Dissertation Overview

The following chapters will cover various aspects of my graduate research:

Chapter 2 lays out the general framework of the experimental and analytical methods and software used to collect the data herein. More specific details for each experiment will also be included in its respective chapter.

Chapter 3 covers *operando* X-ray diffraction of anthraquinone derivatives as the cathode in lithium-ion batteries.

Chapter 4 delineates the many ex-situ attempts to obtain data on the lithiated form of anthraquinone. These include solution-based electrocrystallization; chemical reduction; and isolation of discharged electrode films.

Chapter 5 is a slightly expanded version of the manuscript I wrote regarding the *operando* XRD/XAS analysis done on germanium nanowires as the anode in lithium-ion batteries.

Chapter 6 explains lithium-sulfur XAS data collection and spectral calculation.

Chapter 7 collects the several side projects I did into one place:  $\text{Li}_3\text{VO}_4$  insertion; ceria lattice strain; ionomer SAXS. I also delineate other synchrotron projects to which I contributed in some way.

Chapter 8 gives my reflections on insights gained and possibilities for future work that can draw upon what I have accomplished here.

## REFERENCES

- 
1. Boehm, H.-P.; Setton, R.; Stumpp, E. *Pure & Appl. Chem.* **1994**, *66*, 1893–1901.
  2. Olsher, U.; Izatt, R.; Bradshaw, J.; Dalley, N. *Chem. Rev.* **1991**, *91*, 137–164.

## CHAPTER 2

### EXPERIMENTAL METHODS

#### 2-1. Electrochemical Techniques

*2-1-1. Cyclic voltammetry.* Solution-based cyclic voltammetry (CV) in a three-electrode configuration was used in this work to confirm the electrochemical viability of the organic molecules (Chapter 3). The working electrode was either glassy carbon or platinum; the counter electrode was a coiled platinum wire; and the reference electrode was Ag/Ag<sup>+</sup>. A linear potential sweep was applied and the resultant current was measured. If the redox couple under investigation was air-sensitive, CV measurements were performed in an argon-filled glove box.

*2-1-2. Galvanostatic cycling.* The majority of the electrochemical work done in this research was galvanostatic in a two-electrode configuration, most often in a 2032 coin cell. That is, a constant current density was applied to the working electrode and the resultant potential versus a lithium counter/reference electrode was measured as a function of time. Potential limits were imposed in order to prevent deleterious reactions.

#### 2-2. Sample Preparation

*2-2-1. Organic freestanding electrodes.* A 6:3:1 mass ratio of active material: carbon black: polymer binder was used. The active material was ground to a fine powder by

itself for 20 minutes. Then carbon black was added and mixed together for another 20 minutes. Polytetrafluoroethylene (PTFE) was worked into the powder until glossy and malleable, with ethanol added dropwise to solubilize the Teflon. The film was rolled out between two pieces of weigh paper until uniformly thin, and then it was dried overnight at 50°C in a vacuum overnight to remove solvent and any trace water. Electrodes were punched with a 7/16” die and pumped into the argon –filled glove box for coin cell preparation.

*2-2-2. Inorganic cast electrodes.* For inorganic electrode materials, doctor blading was the film preparation method of choice. Because the inorganic materials were more electronically conductive than the organics, a 7:2:1 mass ratio of active material:carbon black:binder was mixed with *N*-methyl-2-pyrrolidinone (NMP) as the solvent. Three pieces of Scotch tape were used to guide the razor blade to spread the ink evenly on copper foil. The film was dried under a heat lamp for a few hours before spending the night in the vacuum oven to remove any trace water.

*2-2-3. Coin cell preparation.* Coin cells were assembled in an argon-filled glove box by stacking the components in the following order: cathode casing; working electrode film; five drops of electrolyte; Celgard 2320 separator; two drops of electrolyte; lithium metal; porous nickel foam as a conformal spacer; and anode casing. The stack was sealed using a manual battery crimper (Hohsen). Components of the *operando* coin cells were prepared prior to assembly. A 3mm diameter hole was drilled through the center of each commercial stainless steel coin cell anode and cathode casing, and

125 $\mu$ m Kapton windows were affixed to the outside with high vacuum epoxy (TorrSeal). Holes were also drilled through the nickel foam spacer and the lithium metal in order to remove as much non-active material as possible from the beam path (Figure 2-1).

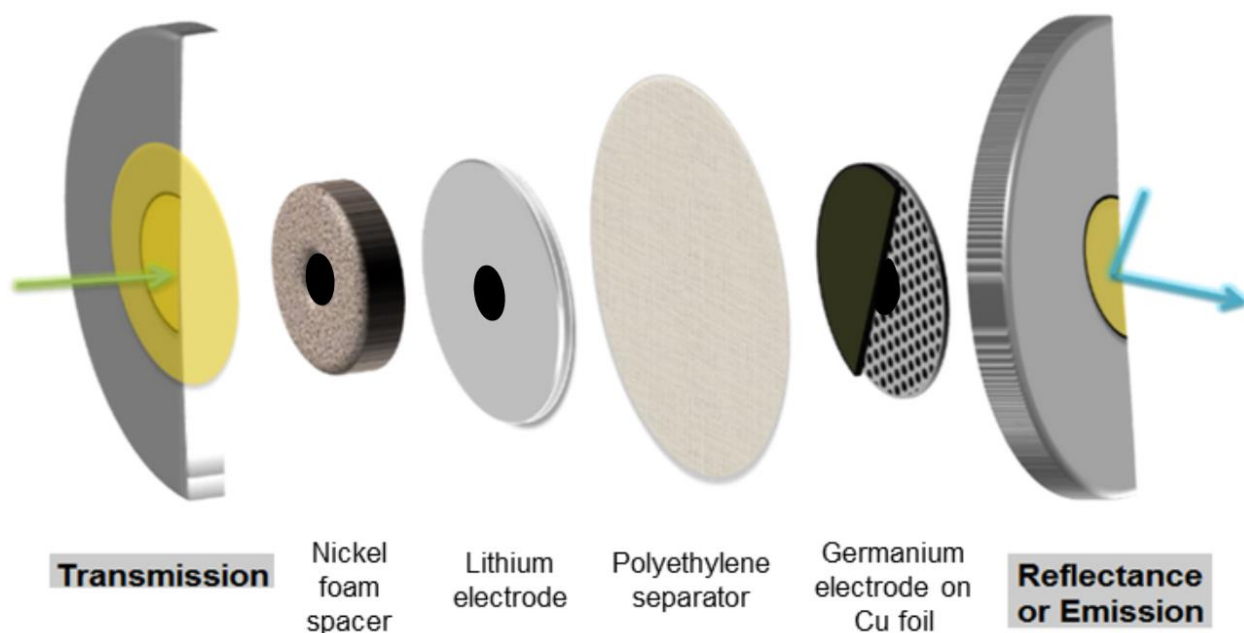


**Figure 2-1:** Exploded schematic of a 2032 coin cell modified for *operando* X-ray measurements.

### 2-3. X-Ray Methods

*2-3-1. Benchtop vs. synchrotron.* One might ask, “Isn’t it good enough to use a lab diffractometer for powder X-ray diffraction?” While you generally do not have to reserve time several months in advance on a benchtop diffractometer, the benefits of synchrotron X-ray sources far outweigh the inconvenience of waiting for the next

beamtime. The high flux of X-ray generated by the synchrotron greatly reduces the timescale required to collect quality datasets, and the high degree of collimation improves resolution of peaks and other meaningful signals. These factors lead to the possibility of real-time, real-situation measurements.

When rapid access was required for screening the products of an ex-situ attempt (Chapter 4), the DiSalvo lab diffractometer with Bragg-Brentano geometry and a Cu K $\alpha$  source was used. Powder samples were packed into a flat-plate low-background holder and Kapton was sealed around air-sensitive samples with vacuum grease.

*2-3-2. Diffraction.* At the Cornell High Energy Synchrotron Source (CHESS), XRD data were collected at stations A2 and F3 on a 2D area detector as rings. Fit2D was used to integrate the rings radially in order to obtain a 1D plot of intensity versus scattering angle or d-spacing. Each diffraction pattern was normalized to the counts recorded in an upstream ion chamber at the time of acquisition to account for the time dependence of the incident beam intensity. To eliminate image hangover from the detector, a dark image was obtained after each diffraction snapshot. In addition, a background diffraction pattern was collected from a coin cell containing all components except for the organic active component. The dark images were then subtracted from each scan, and the resulting points were each divided by the background points to accentuate the sample diffraction peaks. For ease of

concomitant examination of state of charge and diffraction pattern, the processed XRD patterns were plotted as a contour plot versus voltage profile (Figure 2-2).

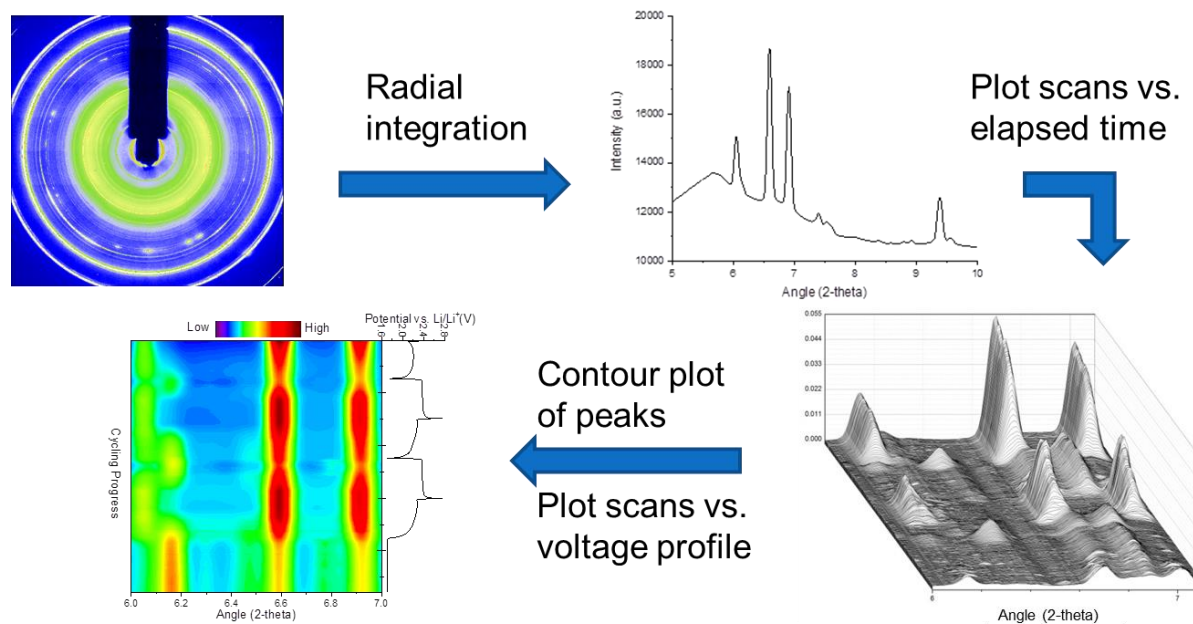


**Figure 2-2:** Flow of *operando* XRD data workup.

2-3-3. *Absorption.* XAS data were collected in transmission mode via ion chambers at CHESS stations C1 and F3 about from 100eV below to 600eV above the absorption edge of the element under investigation, except in the case of sulfur (Chapter 6), where we collected only XANES spectra. Sample ORCA input files used to calculate XANES spectra of polysulfide species are presented below:

Single point:

```
#Single Point BP86/TZVP Calculation of S2(2-)  
! UKS BP86 def2-TZVP def2-TZVP/J SP  
! TightSCF Grid4 NoFinalGrid NormalPrint PAL8
```

```
%cosmo epsilon 7.9  
end
```

```
%maxcore 4000
```

```
%SCF Directresetfreq 1  
DIIS MaxEq 15  
end  
Shift Shift 0.5  
Erroff 0.1  
end  
MaxIter 500  
end
```

```
* xyz -2 1  
S -9.141740 6.661986 0.000000  
S -6.952935 6.661986 0.000000  
*
```

The results were then fed into a calculation of the sulfur K-edge excitations:

```
#SK BP86/TZVP Calculation of S22-  
! UKS BP86 def2-TZVP def2-TZVP/J SP MOREAD NOITER  
! TightSCF Grid4 NoFinalGrid NormalPrint PAL8
```

```
%cosmo epsilon 7.9  
end
```

```
%maxcore 4000
```

```
%moinp "s22_2.gbw"
```

```
%tddft NRoots 10  
MaxDim 300  
XASLoc[0] = 0, 1  
XASLoc[1] = 0, 1  
OrbWin[0] = 0, 1, -1, -1  
OrbWin[1] = 0, 1, -1, -1  
DoQuad true  
end
```

```
* xyz -2 1  
S -9.141740 6.661986 0.000000  
S -6.952935 6.661986 0.000000  
*
```

## 2-4. Software

Without access to the following software packages, this research would not have been possible:

- Mercury, VESTA, and CrystalMaker for visualizing crystal structures and predicting powder diffraction patterns;

- Fit2D and ImageJ for visualizing 2D diffraction data and radially integrating the data to generate 1D diffraction patterns;
- CMPR and FullProf for indexing unit cells, fitting peaks, and determining profile parameters;
- GSAS/EXPGUI for sequential Rietveld refinement of diffraction patterns;
- The Demeter suite of programs – Atoms, Hephaestus, Athena, and Artemis – for predicting, processing and fitting EXAFS spectra;
- ORCA for predicting XANES spectra;
- Spec, Matlab, Python (pymca), Origin, and Mathematica for collecting, processing, and plotting diffraction and absorption data;
- VersaStudio and EC-Lab for performing electrochemical measurements in lab and at the synchrotron;
- JANA (charge flipping), Fox (Monte Carlo, not dependent on cell), and EXPO (direct methods) for attempting to solve crystal structures by powder diffraction.

## CHAPTER 3

# ELECTROCHEMICAL LITHIATION-INDUCED POLYMORPHISM OF ANTHRAQUINONE DERIVATIVES OBSERVED BY *OPERANDO* X-RAY DIFFRACTION

### 3-1. Introduction

Conventional lithium-ion batteries employ inorganic oxides (e.g.  $\text{LiCoO}_2$ ) and graphite ( $\text{LiC}_6$ ) as cathode and anode electrodes, respectively. The charge/discharge processes involve (de)/intercalation events which are known to be kinetically slow, resulting in low rates of charge and discharge (“C-rates”). An alternative, yet relatively unexplored, approach is the use of electroactive organic molecules (in place of the metal oxide) as the cathode in a lithium-ion battery (LIB). Through computational design and screening, combined with synthesis, organic molecules can be tuned over a broad parameter space to yield materials that can exchange multiple electrons per formula unit, leading to high gravimetric capacities. In addition, the formal potentials can be tuned so that theoretical energy densities in excess of 1,500 Wh/kg are possible<sup>1</sup>. In selecting an organic electrode candidate, the parameters of reduction potential versus lithium, theoretical capacity, and cyclability are considered.

The Tarascon group has driven the study of small molecule organics for battery applications. Of note are dilithium terephthalate<sup>2,3,4</sup> and ethoxycarbonyl<sup>5</sup>. Ex-situ X-ray diffraction of the lithiated molecules showed that structure changes had occurred,

but no further characterization was attempted. As noted by Burkhardt et al.<sup>6</sup>, elucidating the structure of molecular crystals is incredibly challenging due to the plethora of possible polymorphs. Still, density functional theory (DFT) is a powerful tool for determining reduction potentials versus lithium. Some groups have applied DFT to determine lithiated crystal structures, but they either do not take into account any change in molecular stacking<sup>7</sup> or space group<sup>8</sup>, both of which are extremely likely possibilities and clearly raise concerns about the validity of the results. Recently, Kang et al. employed DFT and Grand Canonical Monte Carlo (GCMC) methods to propose crystal structures for electrochemically-generated dilithium rhodizonate,  $\text{Li}_2\text{C}_6\text{O}_6$ , and related them to the experimental powder XRD patterns<sup>9</sup>. However, to our knowledge this is the only work, thus far, to attempt such comparative analysis. We fully concur with their assertion that solid-state interactions must be taken into account when determining the viability of a crystalline organic electrode material.

Quinones, in general, and anthraquinones, in particular, are attractive organic systems for electrical energy storage applications due to their ability to reversibly exchange multiple electrons per formula unit. Many groups have exploited the electrochemical activity of anthraquinone and related derivatives for organic-based energy storage materials: for flow cell applications<sup>10</sup>; polymer-bound<sup>11</sup>; hybridized to single-wall nanotubes<sup>12</sup>; metal-organic frameworks (MOFs)<sup>13</sup> and covalent-organic frameworks (COFs)<sup>14</sup>, among others. In general, such applications treat the anthraquinone (AQ) moiety as a single molecule, capable of undergoing two

reductions, one at each carbonyl, while structural considerations are largely neglected. While some work notes the impact lithium ion pairing has on anthraquinone's voltammetric response<sup>15,16</sup>, there is no characterization of the ion pair's identity. Other work notes that the AQ crystal structure reforms reversibly when recharged in a lithium battery<sup>17</sup>, but any demonstration of structural transformations during the charge/discharge processes is glaringly omitted.

Within the context of a real lithium-ion battery (LIB), we have observed that crystalline anthraquinone powders will reversibly change crystal packing as a function of state-of-charge (redox state) with well-defined voltage plateaus appearing concomitantly with new phases. *Operando* powder X-ray diffraction (XRD) is a powerful method for screening the structural stability of organic cathode candidates and for understanding electrochemically-induced structural transformations within organic systems. If we could fully describe these newly formed molecular crystals, we would be able to illuminate the mechanism by which the quinone moieties charge-compensate.

In this work, a family of four anthraquinones, with groups of differing electron-withdrawing ability, was selected for study by *operando* powder X-ray diffraction. The different electronic and structural aspects of these four derivatives should affect the coordination of lithium to the reduced species and, therefore, impact the packing of the lithiated structures. This analysis, which appears to be the most extensive ever done, can serve as a model for studying organic charge storage within

crystalline small-molecule candidates. One must keep in mind that solution-based methods cannot predict the solid-state reactivity. Also, with improved computational structure prediction, intermediate crystal structures will be able to be Rietveld-refined to fit powder diffraction data.

### 3-2. Experimental Details

*3-2-1. Materials.* Chemicals were purchased from Sigma-Aldrich and used without further purification unless otherwise noted.

*3-2-2. Synthesis.* AQ was recrystallized as previously described<sup>18</sup> and sublimed at 260°C under vacuum to ensure high purity. 1,5-dichloroanthraquinone (DCLAQ) was purified by sublimation at 220°C under vacuum.

DCLAQ (1.0 g, 3.6 mmol) and copper(I) cyanide (1 g, 10 mmol) were dispersed in *n*-methyl pyrrolidinone (NMP) (50 mL) and heated to 180°C under argon for 6 hours. The hot dark brown solution was poured onto ice (500mL), and the brown-green precipitate was filtered, washed with water and dried under vacuum. The copper complex was decomposed with 4 N nitric acid (100 mL) at 60 °C for 4 hours. The brown solid was filtered, washed with water and air-dried, giving a yellow-brown powder of 1,5-dicyanoanthraquinone (DCAQ) (0.82 g, 78%). Anal. calcd for C<sub>16</sub>H<sub>6</sub>N<sub>2</sub>O<sub>2</sub>: C, 74.42%; H, 2.34%; N, 10.85%; found: C, 74.16%; H, 2.66%; N, 10.53%.

DCAQ was dispersed in a solution of 70% H<sub>2</sub>SO<sub>4</sub> and the mixture was stirred at reflux for 3 hours, after which the hot solution was poured onto ice. The precipitate was collected by filtration, washed with water, and re-suspended in 200 mL of dichloromethane. This slurry was filtered, and the filtrate was dried under vacuum to give a brown powder of 1,5-dicarboxyanthraquinone, which was dispersed in a dimethyl formamide (DMF) solution of lithium t-butoxide to afford the lithiated dicarboxylic acid anthraquinone (DCAAQ). The lithiated form was synthesized so as to minimize the chances of side reactions from the acidic proton.

*3-2-3. Sample preparation.* For each of the four AQ derivatives under investigation, the organic crystals were ground into a fine powder using an agate mortar and pestle. The organic powder was then intimately mixed with Super-P Li carbon additive for conductivity and PTFE for malleability in a 6:3:1 ratio by mass, respectively. The mixture was rolled out as a thin film using ethanol to solubilize the Teflon binder. Electrode films were dried in a vacuum oven overnight at 50°C, and then 7/16" circular electrodes were punched for use in 2032-sized stainless steel coin cells. The electrolyte solution in the coin cells was 1M bis(trifluoromethanesulfonyl)imide (LiTFSI) in equal parts dioxolane to dimethoxyethane (DOL/DME). Cells were assembled in the same manner as the unaltered coin cells in an argon-filled glovebox with particular attention to exclusion of oxygen and water until experimental use.

3-2-3. *Electrochemical methods.* Cyclic voltammetry (CV) of 1mM solutions of each analyte (Figure 3-1) was conducted at room temperature in a three-compartment cell using a glassy carbon electrode (GCE) (5.0 mm diameter) working electrode, a coiled Pt wire counter electrode, and a silver/silver ion ( $\text{Ag}/\text{Ag}^+$ ) reference electrode. The electrolyte solution was 0.1M lithium perchlorate ( $\text{LiClO}_4$ ) in DMF. All measurements were performed in an argon-filled glove box to exclude moisture and oxygen. In all cases, the solution near the working electrode turned red as the molecules were reduced.

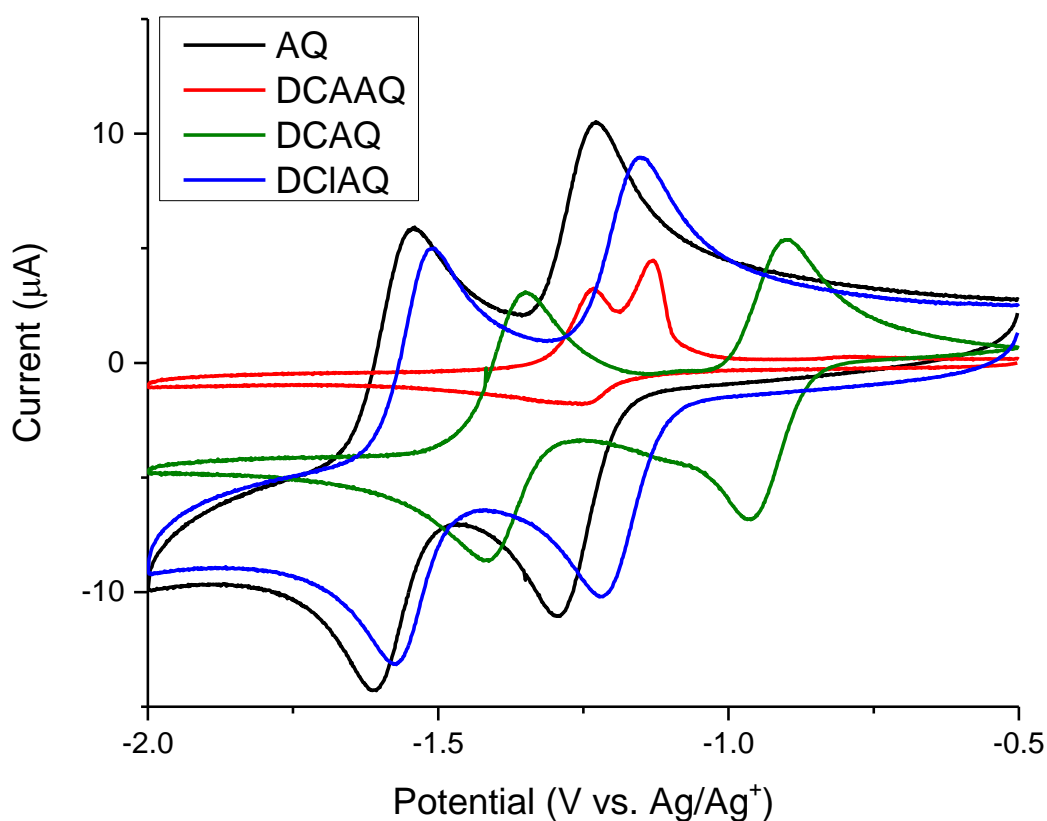


**Figure 3-1:** Cyclic voltammograms of anthraquinone derivatives under investigation.

Chronopotentiometric cycling of the as-prepared electrode films in unmodified coin cells (Figure 3-2) was carried out on an Arbin multichannel battery cyclier. A current density equivalent to a C-rate of 0.2C, based on the theoretical capacity of each molecule, was applied to each cell, and voltage ranges were determined from the CV experiments. For each *operando* powder XRD experiment, the modified coin cell was mounted in the X-ray beam path, attached to a VersaSTAT 3 potentiostat/galvanostat (Princeton Applied Research), and cycled galvanostatically with the same current density and voltage window as determined for the unmodified cells.

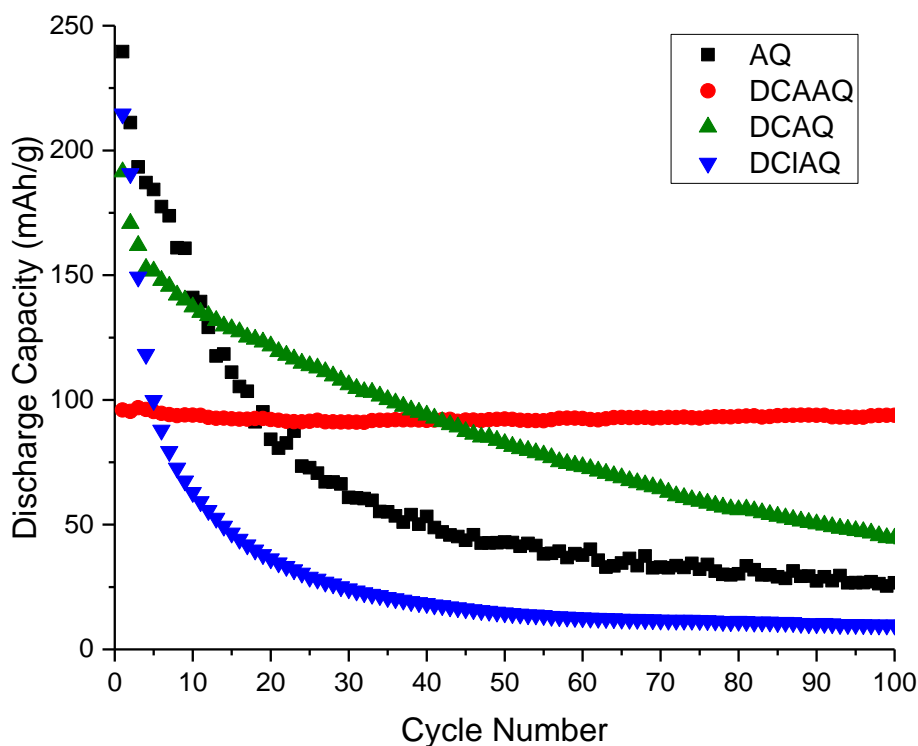


**Figure 3-2:** Galvanostatic cycling of anthraquinone derivatives under investigation.

*3-2-5. X-ray methods.* Powder X-ray diffraction patterns were collected at room temperature at the A2 station of CHESS. The incident energy was calibrated to the antimony K-edge, 30.491keV, or  $\lambda=0.406626\text{\AA}$  using a 2D amorphous silicon large-area detector (General Electric). The diffraction rings were integrated radially to produce 1D diffraction patterns using the software package Fit2D<sup>19</sup>.

*3-2-6. Computation.* The DFT methodology employed in this work to determine the reduction potentials (versus Li/Li<sup>+</sup>) of anthraquinone follows from previous work<sup>20</sup>. Briefly, the 6-31+G\*\* basis set was employed on optimized single molecules. The polarizable continuum model (PCM)<sup>21,22</sup> was employed using propylene carbonate (PC) as the solvent with a static relative permittivity of 64.9 and a dynamic relative permittivity of 2.02. The calculated voltages are listed in Table 3-1, along with the theoretical capacities, assuming two reductions, and the resulting theoretical energy density (energy density = capacity \* voltage of first reduction). Computational attempts on our part to determine molecular packing of the lithiated molecules were unsuccessful, though the lithium ion did bind to the oxygen in each of the lowest-energy structures.

**Table 3-1:** Theoretical capacities, predicted reduction potentials, and resultant energy densities of the four anthraquinone derivatives.

Molecule	Capacity (mAh/g)	Voltage vs. Li/Li+ (V)	Energy Density (Wh/kg)
Anthraquinone	257	2.2, 2.0	570
Dicyano-	208	2.6, 2.4	540
Dichloro-	193	2.3, 2.1	440
Lithiated dicarboxylic-	174	2.4, 2.2	420

### 3-3. Results

*3-3-1. DCAQ.* A crystal structure for DCAQ is known<sup>23</sup>, but the synthetic method used in this work yielded a different polymorph than the one previously described. Elemental analysis yielded the expected percentages of carbon, hydrogen, and nitrogen, though the percentages would be even closer if one of the quinones was already reduced to an alcohol (Anal. calcd. for  $C_{16}H_7N_2O_2$ : C, 74.13%; H, 2.72%; N, 10.81%). Attempts to index the powder XRD pattern of the material were unsuccessful and so an accurate initial structure could not be determined. The peaks initially present never returned upon subsequent cell cycling. These facts also support the existence of a semiquinone in the starting material, though further characterization would be required to confirm this. During the first discharge, new peaks grew in during the first voltage plateau. At low voltages, a third set of peaks arose, and they appeared to be due to slight lattice parameter changes, instead of a drastic symmetry change, compared to the previous phase. Upon recharge, the second set of peaks returned. At high voltages, a fourth set of peaks appeared that seemed to belong to a different space group. During the second cycle, the peaks proceeded reversibly from set 2 to 3 on the discharge and 2 to 4 on the recharge (Figure 3-3).

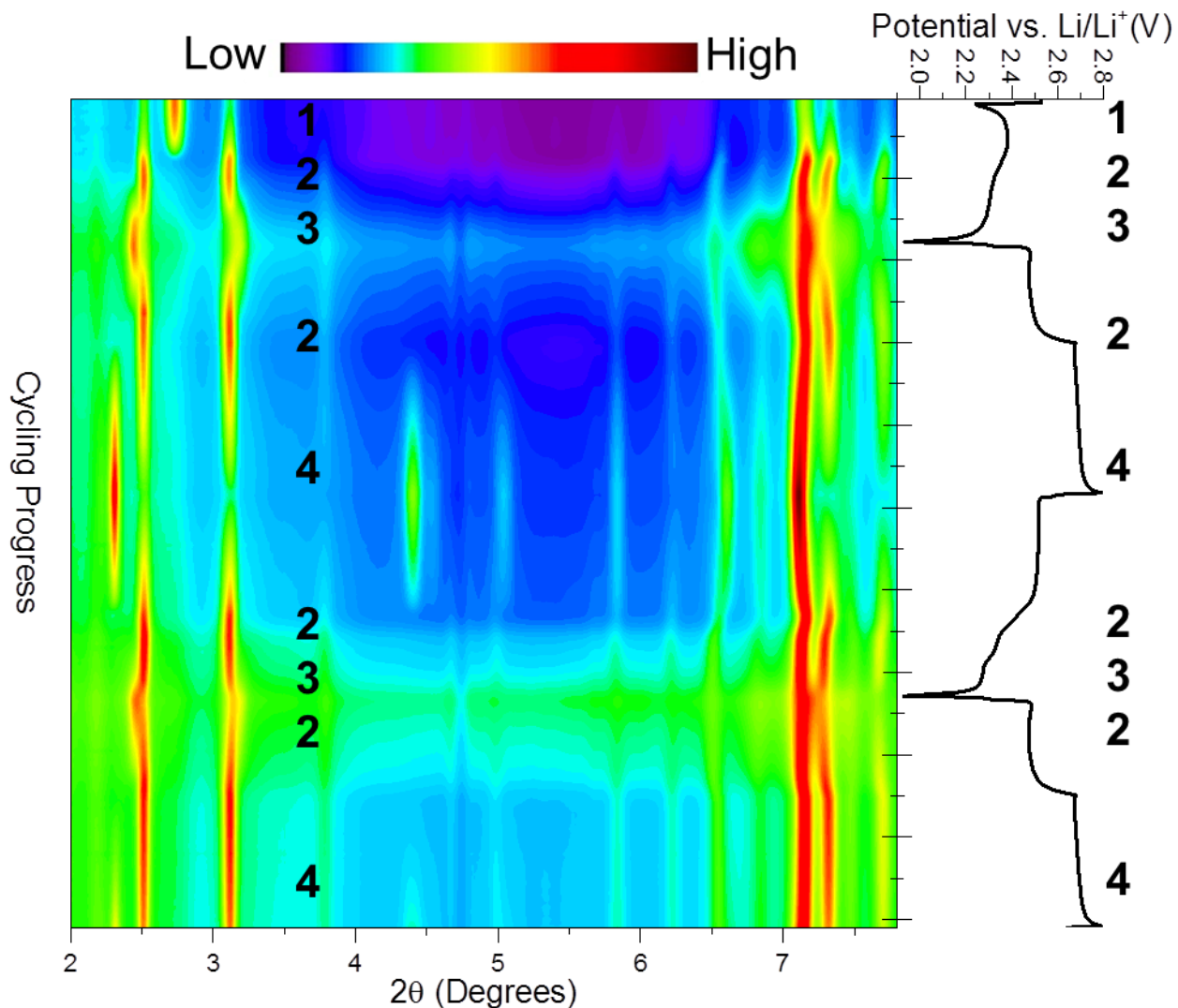


**Figure 3-3:** Galvanostatic cycling of DCAQ with different sets of diffraction peaks labeled as described in the preceding paragraph.

3-3-2. *DCAAQ*. Single crystals of the 1,5-dicarboxyanthraquinone prior to lithiation were recrystallized from DMF, mounted in inert oil, and transferred to the cold gas stream of the diffractometer. Crystal data.  $C_{16}H_8O_6 \cdot 2(C_3H_7NO)$ ,  $M = 442.42$ , monoclinic,  $a = 12.8170(11)$ ,  $b = 7.3554(6)$   $c = 11.1126(8)$  Å,  $\beta = 98.490(3)^\circ$ ,  $U = 1036.15(14)$  Å<sup>3</sup>,  $T = 173(2)$  K, space group  $P2_1/c$  (no. 14),  $Z = 2$ , 9942 reflections measured, 2563 unique ( $R_{int} = 0.0254$ ) which were used in all calculations. The final

wR(F<sub>2</sub>) was 0.1022 (all data). The lithiated dicarboxylate anthraquinone (DCAAQ) was indexed in McMaille<sup>24</sup> as monoclinic,  $a = 4.7597$ ,  $b = 14.1796$   $c = 8.3039$  Å,  $\beta = 101.091^\circ$ , space group P2<sub>1</sub> (no. 4).

The *operando* XRD patterns of DCAAQ displayed two intermediate phases, one midway through discharge and one at low voltages (Figure 3-4). Upon recharge, the patterns passed back through these phases, but meanwhile, a peak at 6.5° grew and the other peaks decreased in intensity. The initial phase was gone by the end of the third cycle, and several new peaks developed. Rather than distinct toggling between two phases, the new peak sets exhibited slight and gradual changes, indicating a solid solution reaction. The material was decomposing or dissolving compared to its initial diffraction pattern, though DCAAQ had the most stable cycling of the four derivatives explored (Figure 3-2). The persistence of an initial structure, therefore, is not necessary for stable cycling. In fact, the ability to form a phase more amenable to charge transfer might be important for cyclability. In this case, the presence of the carboxylic acid groups might act as stabilizers for a reorganized structure, likely from binding Li<sup>+</sup>.

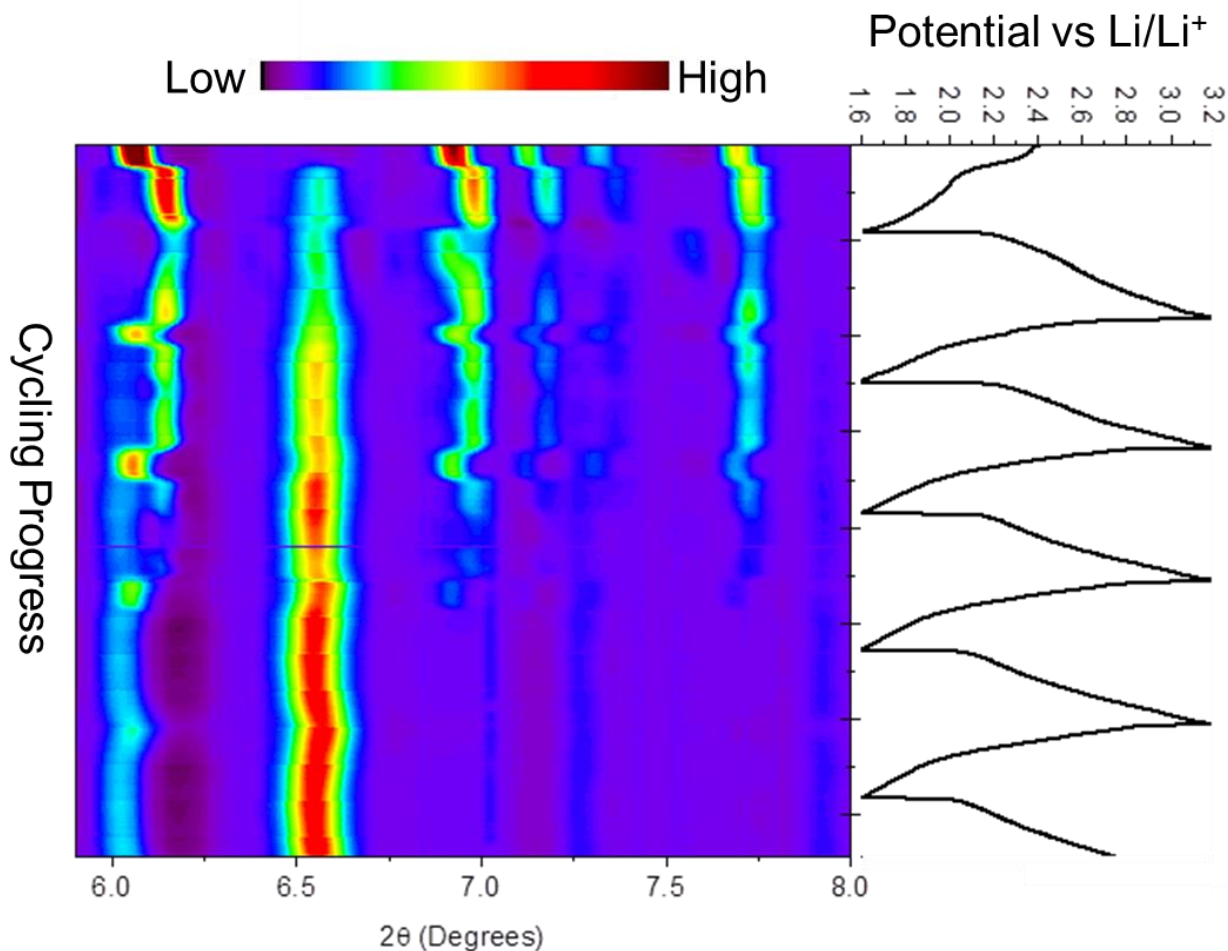


**Figure 3-4:** Galvanostatic cycling of DCAAQ.

3-3-3. *DClAQ*. The intent of studying dichloroanthraquinone (DClAQ) was to begin with a known crystal structure to simplify structure solution for the lithiated phase. Surprisingly, by the time the coin cell was positioned in the beampath, a crystal structure, significantly different from the phase-pure DClAQ, had developed. Even passive contact with the lithium electrolyte solution was enough to modify molecular packing (Figure 3-5). This change could be attributed to either solvent-induced polymorphism or decomposition to a different crystalline phase. Because chloride is a

good leaving group in organic chemistry, it is possible that one or both chloro groups were displaced. Either way, the new diffraction peaks could not be indexed.

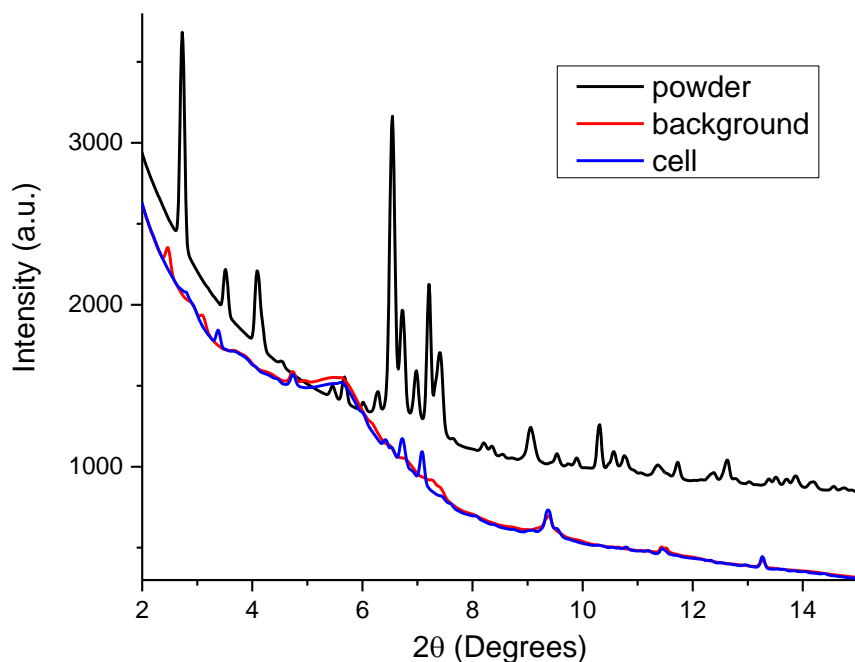


**Figure 3-5:** Diffraction patterns from DCIAQ powder, background, and cell.

Once this rearrangement occurred, the formal potential of the redox processes increased by 0.1V each as compared to the predicted values. Upon electrochemical cycling, the new phase persisted until a new plateau emerged in the discharge curve, at which point the diffraction pattern changed dramatically. The new peaks that arose at 2.2V during the first discharge became the predominant features. During the long plateau at 2.5V on the recharge, these new peaks slowly faded as the peaks from the beginning of the cycle returned, albeit with smaller intensity. As the electrochemical profile became jagged during the third recharge, diffraction peaks corresponding to yet another phase made a brief appearance (Figure 3-6).

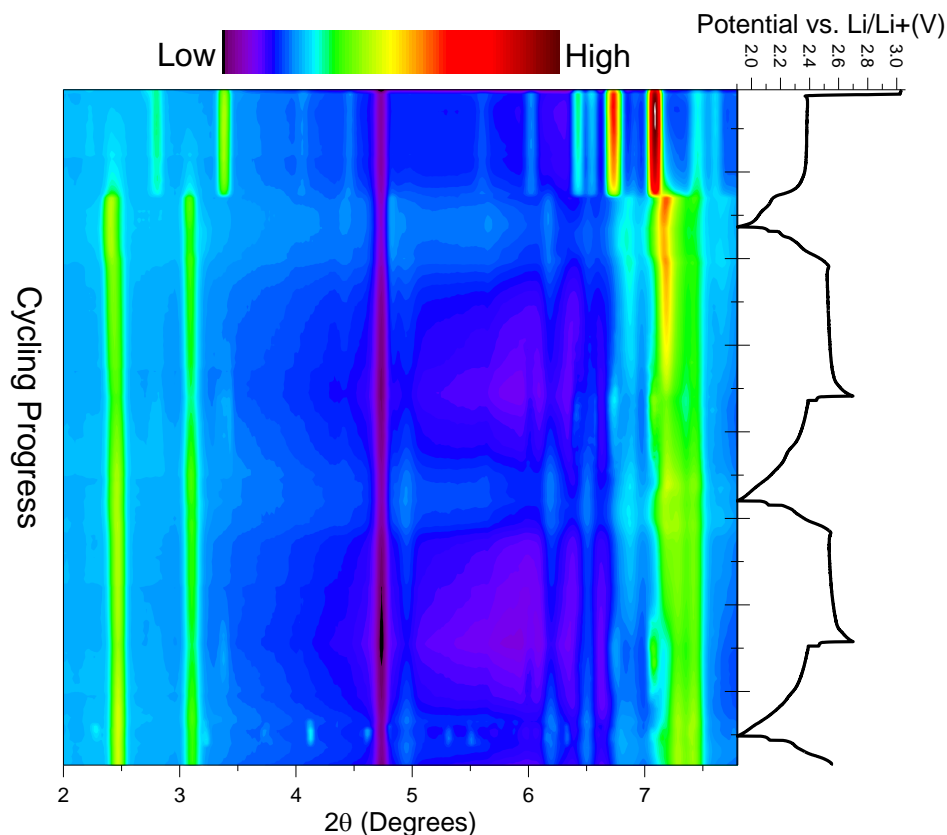


**Figure 3-6:** Galvanostatic cycling of DCIAQ.

3-3-4. *AQ*. Anthraquinone has a known crystal structure and it has the least complex molecular structure in this study, and so there was the greatest likelihood that the lithiated phase would be determined here. This time, the parent AQ peaks did not disappear in the coin cell. The AQ peak heights faded and new peaks grew in as the cell was discharged. With each cycle, the progression of new peaks differed slightly (Figure 3-7). Peaks that arose at low angle at the point of lowest discharge suggested that a crystal with orthorhombic symmetry formed. Notably, and as observed in the literature<sup>18</sup>, the original anthraquinone phase was regained at high voltage, indicating that the removal of the lithium was reversible.

When the coin cell was held at the low voltage cutoff (1.7V vs. Li/Li<sup>+</sup>), peaks from the new phase became more intense the longer the voltage was held. Since only about half of the theoretical capacity was achieved in these cells, it stands to reason that by holding the cell at lithiating potentials, more complete conversion of the active material was attained. Even with strong diffraction peaks, a new unit cell was not successfully indexed, and so we could not proceed to solving the crystal structure from powder diffraction. Many ex-situ efforts went into isolating the lithiated phases of anthraquinone, as will be explained in Chapter 4.

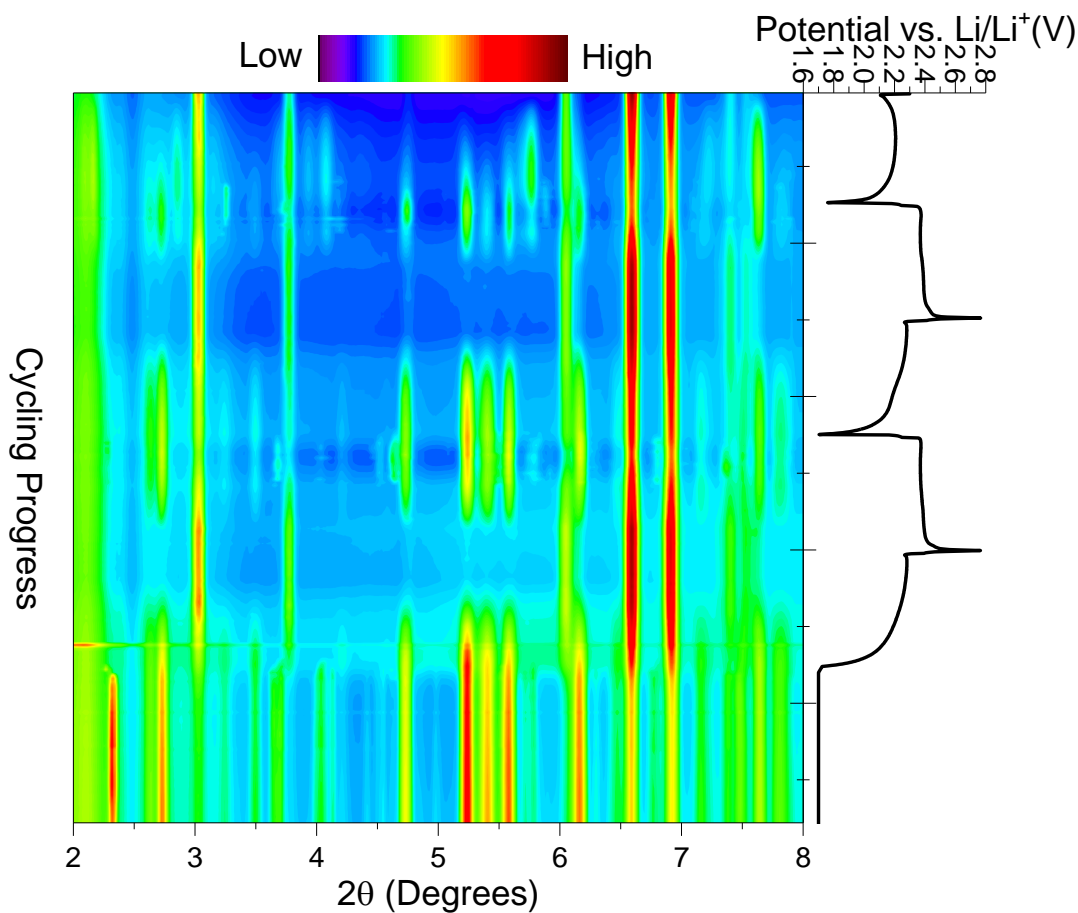


**Figure 3-7:** Galvanostatic cycling AQ with voltage held at 1.7V vs Li/Li<sup>+</sup> at the end.

### 3-4. Discussion

Even modest differences in the electron density on the external rings of the anthraquinone (from CN, COOLi, Cl, or H moieties) lead to mechanisms of solid-state charge storage observable by diffraction that are entirely different. Clearly, the system under investigation is inherently complex. Organic crystals are subject to a myriad of thermodynamic and kinetic factors that impact stacking and order. Electrochemical reactions further complicate the issue. The observed changes are not predictable currently, but they are self-consistent across many *operando* diffraction runs.

This work intends to illuminate the inherent contradiction present in the field of organic battery materials. Generally speaking, in order to test the viability of organic small molecules as electrode materials, powders of the organic candidate are mixed with conductive additive and cast as a film. The resultant electrochemical reaction occurs in the solid state, which we present here clearly. However, an overwhelming majority of researchers continue to describe the redox processes as occurring on a single molecule and to consider solution-based methods valid for screening candidate viability. This work is proof positive that a cyclic voltammogram, a cyclability plot, and a sketch of a proposed molecular mechanism do not a full story make.

At first glance, the task of assigning new crystal structures to the new peaks that arise from electrochemical lithiation seems straightforward. Peaks grow in and

decay concurrently with voltage output from the coin cell. However, the methodology is limited by the low symmetry and X-ray scattering power of organic molecules and the high background of the experimental setup. Peak overlap becomes insurmountable. To have enough peak separation to distinguish individual reflections from the organic crystals, the incident X-ray beam would need to have  $\lambda \approx 4\text{\AA}$ , or  $E \approx 3\text{keV}$ . Transmission through the  $250\mu\text{m}$  thickness of the Kapton windows of our modified coin cell would decrease from  $>99\%$  at  $30\text{keV}$  to  $1\%$  at  $3\text{keV}$ . Also, the upstream X-ray optics at CHESS are such that we would have at least two orders of magnitude less flux on our sample at the lower energy.

Furthermore, phase information is lost when analyzing powder diffraction as compared to single crystals. This makes it much more difficult to look for systematic absences that lead to determining the proper space group from a given set of diffraction peaks. Some indexing of the diffraction peaks via the programs TREOR, ITO, or DICVOL gave unit cells, but they were highly variable and unreliable. Further structural solution and refinement is impeded by the absence of a trustworthy unit cell.

### **3-5. Conclusions**

We have observed clear crystalline changes in tandem with electrochemistry for four anthraquinone derivatives in LIBs. It is important to note that the material that had the most stable electrochemical cycling performance (Li-DCAAQ) had diffraction

peaks that faded and other peaks that grew in upon cycling. This result was unexpected, and it challenges the current thinking about the need for reversible structural stability in a well-behaved battery system. The fact that we can see new peaks at low voltage gives credence to the claims that ion-pairing is occurring between lithium cations and anthraquinone anions. When utilizing organic crystals as the cathode material in lithium-ion batteries, one must certainly consider solid-state reactivity, especially the possibility of conversion reactions that lead to stabilization.

In the most straightforward case of the anthraquinone structural evolution, we found that the lithiated phase is crystalline, able to scatter, and reversibly formed. In order to solve this and other new crystal structures from powder diffraction, concerted computational and experimental efforts are required. Reasonable crystallographic models must be generated by exploring all possible packing conformations, including solvent and electrolyte coordination<sup>25</sup>, dimerization, or decomposition. If possible, reducing the inherent background contributions from the *operando* coin cell would lead to more accurate absolute peak intensities for Rietveld refinement of predicted lithiated phases. A major limitation of diffraction from organic materials is the peak overlap brought about by the low crystal symmetry, and diffraction theory has yet to advance to overcome this for complex systems. Even so, the diffraction experiments presented in this work give a phenomenological description of crystallographic changes that occur in anthraquinone-based organic crystals under the operating conditions of a lithium-ion battery.

## REFERENCES

1. Burkhardt, S. E.; Lowe, M. A.; Conte, S.; Zhou, W.; Qian, H.; Rodríguez-Calero, G.G.; Gao, J.; Hennig, R. G.; Abruña, H. D. *Energy Environ. Sci.* **2012**, *5*, 7176.
2. Armand, M.; Grugeon, S.; Vezin, H.; Laruelle, S.; Ribière, P.; Poizot, P.; Tarascon, J.-M. *Nat. Mater.* **2009**, *8*, 120–125.
3. Kaduk, J. A. *Acta Crystallogr. Sect. B Struct. Sci.* **2000**, *56*, 474–485.
4. Lee, H. H.; Park, Y.; Shin, K.-H.; Lee, K. T.; Hong, S. Y. *ACS Appl. Mater. Interfaces* **2014**, *6*, 19118–19126.
5. Walker, W.; Grugeon, S.; Mentre, O.; Laruelle, S.; Tarascon, J. M.; Wudl, F. *J. Am. Chem. Soc.* **2010**, *132*, 6517–6523.
6. Burkhardt, S. E.; Bois, J.; Tarascon, J. M.; Hennig, R. G.; Abruña, H. D. *Chem. Mater.* **2013**, *25*, 132–141.
7. Chen, Y.; Wu, Z.; Sun, S. *J. Phys. Chem. C* **2014**, *118*, 21813–21818.
8. Zhang, Y. Y.; Sun, Y. Y.; Du, S. X.; Gao, H. J.; Zhang, S. B. *Appl. Phys. Lett.* **2012**, *100*, 091905.
9. Kim, H.; Seo, D.-H.; Yoon, G.; Goddard, W. a; Lee, Y. S.; Yoon, W.-S.; Kang, K. *J. Phys. Chem. Lett.* **2014**, *5*, 3086–3092.
10. Huskinson, B.; Marshak, M. P.; Suh, C.; Er, S.; Gerhardt, M. R.; Galvin, C. J.; Chen, X.; Aspuru-Guzik, A.; Gordon, R. G.; Aziz, M. J. *Nature* **2014**, *505*, 195–198.
11. Song, Z.; Zhan, H.; Zhou, Y. *Chem. Commun.* **2009**, 448–450.
12. Lee, M.; Hong, J.; Kim, H.; Lim, H. D.; Cho, S. B.; Kang, K.; Park, C. B. *Adv. Mater.* **2014**, *26*, 2558–2565.
13. Zhang, Z.; Yoshikawa, H.; Awaga, K. *J. Am. Chem. Soc.* **2014**, *136*, 16112–16115.
14. DeBlase, C. R.; Silberstein, K. E.; Truong, T. T.; Abruña, H. D.; Dichtel, W. R. *J. Am. Chem. Soc.* **2013**, *135*, 16821–16824.

- 
15. Wain, A. J.; Wildgoose, G. G.; Heald, C. G. R.; Jiang, L.; Jones, T. G. J.; Compton, R. G. *J. Phys. Chem. B* **2005**, *109*, 3971–3978.
16. Tkalcec, M.; Filipovic, I.; Piljac, I. *Anal. Chem.* **1975**, *47*, 1773–1777.
17. Yao, M.; Yamazaki, S. I.; Senoh, H.; Sakai, T.; Kiyobayashi, T. *Mater. Sci. Eng. B Solid-State Mater. Adv. Technol.* **2012**, *177*, 483–487.
18. Stepputat, J.; Jung, G.; Wunderlich, H. U.S. Patent 3,907,836, Sep 23, 1975.
19. Hammersley, A. P.; Svensson, S. O.; Hanfland, M.; Fitch, A. N.; Hausermann, D. *High Pressure Research*, **1996**, *14*, 235–248.
20. Hernández-Burgos, K.; Burkhardt, S. E.; Rodríguez-Calero, G. G.; Hennig, R. G.; Abreuña, H. D. *J. Phys. Chem. C* **2014**, *118*, 6046–6051.
21. M. Cossi, N. Rega, G. Scalmani and V. Barone, *J. Comput. Chem.*, 2003, **24**, 669–81.
22. V. Barone and M. Cossi, *J. Phys. Chem. A*, 1998, **5639**, 1995–2001.
23. Armaghan, M.; Amini, M. M.; Ng, S. W. *Acta Crystallogr. Sect. E Struct. Reports Online* **2010**, *66*, o767.
24. Le Bail, A. *Powder Diffraction*, 2004, **19**, 249-254.
25. Bachman, J. E.; Curtiss, L. A; Assary, R. S. *J. Phys. Chem. A* **2014**, *118*, 8852–8860.

## CHAPTER 4

# EX-SITU APPROACHES TO ISOLATE ANTHRAQUINONE'S LITHIATED PHASE

### 4-1. Introduction

During my first year of graduate study, my work in the lab began with attempts to determine the crystal structure of anhydrous ethoxycarbonyl to fill in a gap in Tarascon's work<sup>1</sup>. They noted that, in order to advance the rational development of organic small molecules as electrode materials in secondary lithium batteries, structure-function relationships must be observed and understood. Though the researchers were able to determine the crystal structures of the tetrahydrated lithium 2,6-bis(ethoxycarbonyl)-3,7-dioxo-3,7-dihydro-s-indacene-1,5-bis(olate), the active material contained no coordinated water, and therefore the crystal structure was not representative. They were able to observe crystallographic changes throughout battery cycling of the anhydrous ethoxycarbonyl, but they could not be rationalized without the initial crystal structure.

My attempts to isolate anhydrous ethoxycarbonyl also proved fruitless, but I discovered an even larger gap in knowledge within the battery community: for organic-based solid-state electrode materials versus lithium, it is still unclear where lithiation occurs. We know that reduction and oxidation reactions occur based on the cyclic voltammetric and chronopotentiometric responses, but these experiments tell

us nothing about the structure of the charge-compensated molecule, and even less about how the lithiated molecules stack in the solid state. Is solvent or supporting electrolyte incorporated in the crystal structure? Does lithium bind at the oxygen as predicted by DFT (Section 3-2-6), or does it intercalate between  $\pi$ -stacked layers of anthracene?

I then embarked on an in-depth *operando* XRD study of anthraquinone (AQ) and three derivatives (Chapter 3) in which I observed several distinct electrochemically-induced polymorphs of these seemingly simple molecular crystals. The new structures, however, were anything but simple to understand. I was not satisfied with the mere observation of the change in diffraction patterns under operating conditions. I wanted to know how the molecules were rearranging under these constant-current (galvanostatic) conditions and where or if lithium cations were binding. Since I had collected many diffraction patterns in my research, none of which seemed to match any known phase, I decided I should approach the problem from another angle – namely, to isolate the lithiated phase of AQ for structure determination from powder diffraction (SDPD)<sup>2</sup> by any means necessary.

## 4-2. Experimental Details

4-2-1. *Passive anthraquinone-lithiating agent contact in solvent.* A 1:2 molar ratio of AQ:lithiating agent in minimal solvent was placed in a vial and stirred magnetically in an argon-filled glove box overnight before collecting XRD patterns on the DiSalvo

lab diffractometer (Cu K $\alpha$  wavelength). Also, AQ was pressurized directly against lithium metal in 1M LiPF<sub>6</sub> in EC:DEC within a Swagelok cell.

*4-2-2. Bulk electrolysis.* I held films of anthraquinone and other derivatives at low voltage, in the argon-filled glove box, in order to isolate the lithiated phase. I removed the lithiated films from the Swagelok cell, rolled them up, inserted them into glass capillary tubes, and sealed the opening with epoxy. We brought the filled and sealed capillaries to the A2 station at CHESS and measured their X-ray diffraction patterns ( $\lambda=0.495935\text{\AA}$ ).

*4-2-3. Electrocrystallization.* Electrocrystallization<sup>3,4</sup> was employed in an attempt to isolate single crystals of lithiated anthraquinone. A solution of 10mM AQ and 0.1M LiClO<sub>4</sub> in DMF was prepared. The working electrode was 3cm of electrolytically cleaned Pt wire. Pt counter and Ag/Ag<sup>+</sup> reference electrodes were used. A constant current density of 11  $\mu\text{A}/\text{cm}^2$  was applied until there was minimal change in the output cell potential (Figure 4-1).

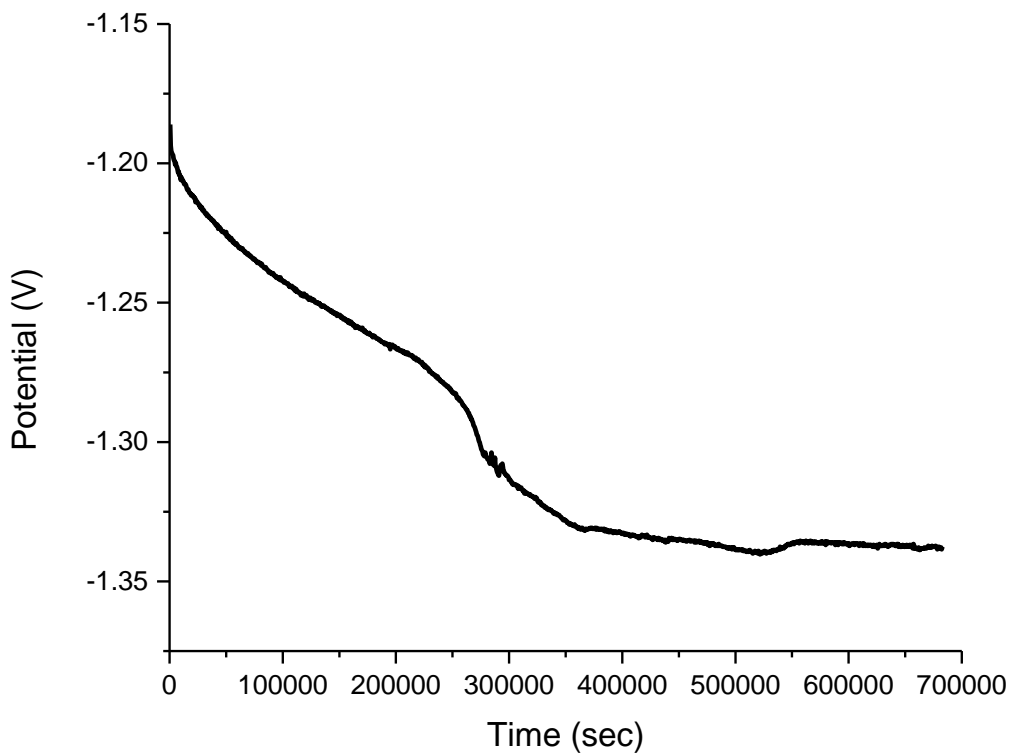


**Figure 4-1:** Electrocrystallization chronopotentiometry vs  $\text{Ag}/\text{Ag}^+$ .

4-2-4. *Chemical reduction.* The following reaction<sup>5</sup> was carried out via cannula technique because of the air-sensitivity of sodium dithionite. A 1:1:4 molar ratio of AQ: $\text{Na}_2\text{S}_2\text{O}_4$ :NaOH was stirred under nitrogen for 45 minutes at  $60^\circ\text{C}$ . The solution was neutralized with HCl (Figure 4-2).

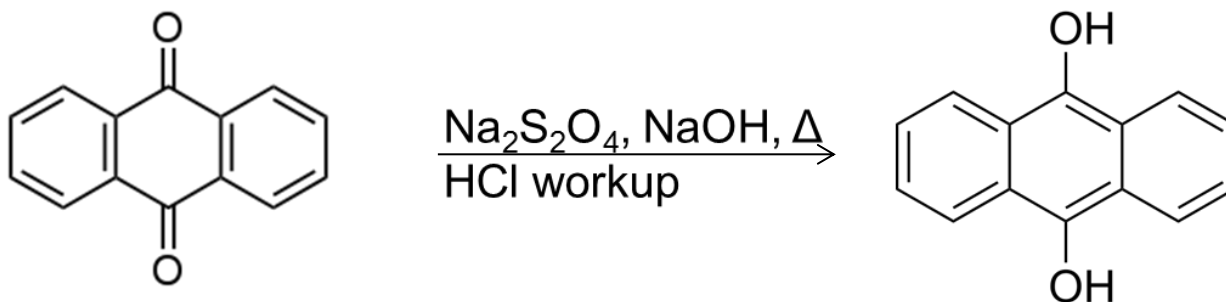


**Figure 4-2:** Reaction schematic of chemical reduction of anthraquinone.

### 4-3. Results

*4-3-1. Passive anthraquinone-lithating agent contact.* Some reaction did occur between AQ and the lithiating agent in all cases: Li metal in TEGDME turned pink; Li metal in THF turned green; and Li(HMDS)<sup>6</sup> in THF turned orange. Unfortunately, the powder patterns we collected did not match the peaks from the ostensibly lithiated phase (Figure 4-3). The sample that had contact with Li(HMDS) and no contact with air had the diffraction pattern most similar to the lithiated AQ phase from the coin cell (Figure 3-7), with its cluster of three mid-angle peaks, but the phases still did not match quite right. When AQ was pressed to lithium in the presence of electrolyte, the powder turned a dark red, a similar shade to what was observed near the electrode during solution cyclic voltammetry (Section 3-2-4). The reacted material was not ordered enough to obtain a single crystal, and by optical microscopy it appeared that only the surface had reacted with the lithium. It was not surprising that we did not get the phase we expected because the reaction was not being driven electrochemically.

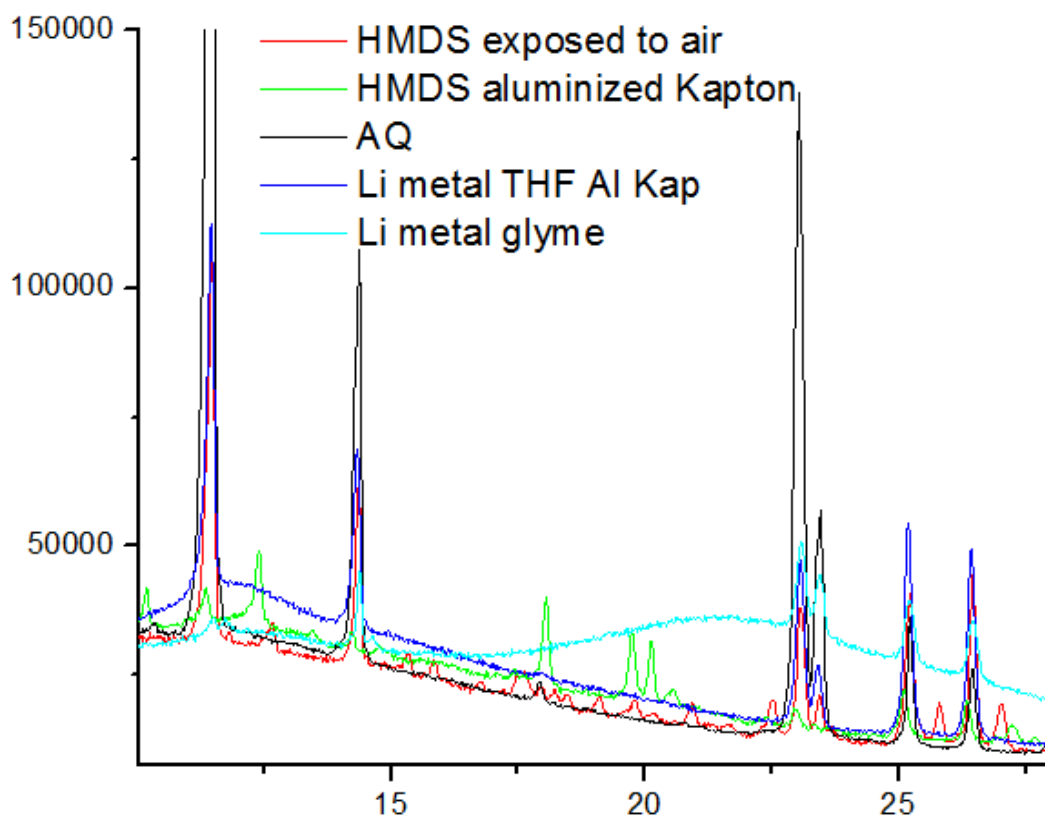


**Figure 4-3:** Powder XRD patterns of AQ that had been in contact with a lithium source.

4-3-2. *Bulk electrolysis.* The next idea was bulk electrolysis and subsequent isolation of the sample. Holding the coin cell at a low voltage for a long time was not enough to isolate the material in the beampath because of the high background of the cell, so I decided to try generating the phase in a Swagelok cell that could be disassembled easily. When analyzed at the beamline in capillaries, the distinctive three peaks that arose at low voltage were present in the diffraction patterns, but peaks from AQ remained (Figure 4-4). Samples had partially relaxed back to their original state or perhaps had not fully reacted in the first place. Peak indexing still gave highly variable results, even when the AQ peaks were ignored. This experimental approach

brought us the closest to accessing the reduced structure outside of the coin cell. Clearly, however, these reduced anthraquinone salts were metastable phases that needed to be observed in the environment in which they developed.

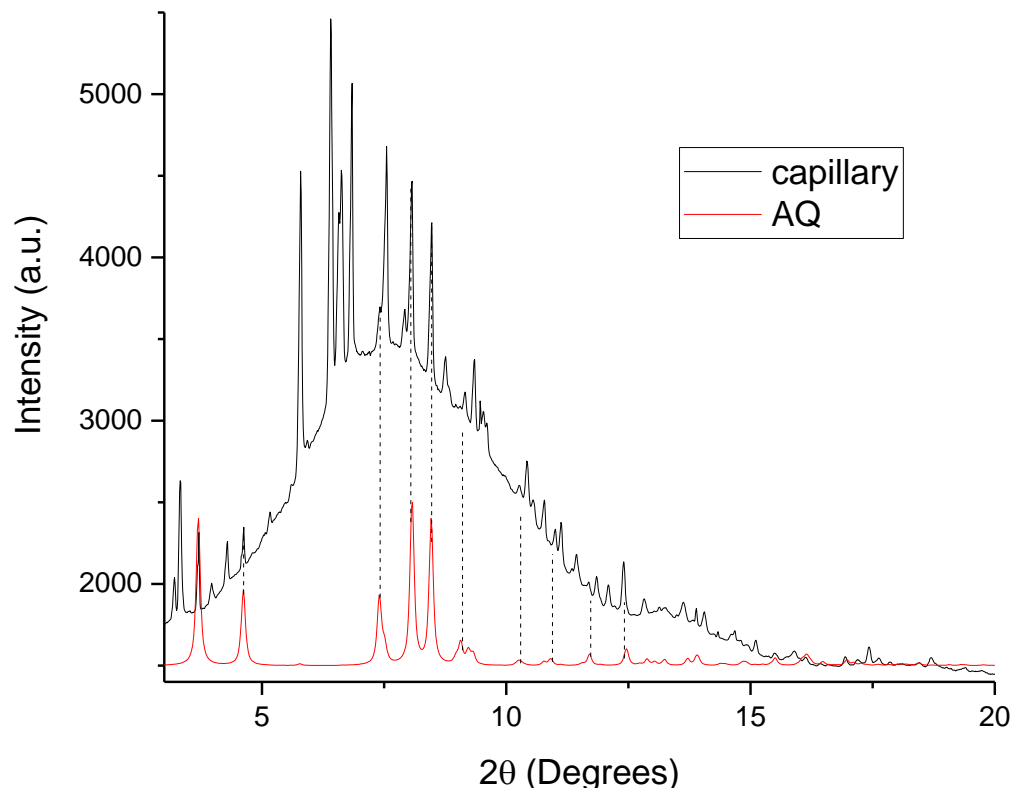


**Figure 4-4:** XRD pattern of sample that had been held at low voltage with AQ plotted beneath to indicate which peaks remained from AQ (background scatter from glass capillary).

*4-3-3. Electrocrystallization.* Generally, electrocrystallization is carried out on organic conductors such as TTF, TCNQ, and BEDT, to form superconducting charge-transfer complexes known as Bechgaard salts<sup>7</sup>. Since our material should become electronically conductive when reduced, electrocrystallization seemed like a viable way to access the lithiated structure. When the chronopotentiometric method was attempted, the solution turned a deep blood red, but no crystals were visible by

eye on the working electrode. Single crystals were isolated from a mixture of the red solution and THF and a structure was determined (Section 3-3-2). The predicted powder diffraction from this crystal structure did not match the peaks from the *operando* cycling, underlining the point that the growth and evolution of these lithiated organic crystals is highly dependent on solvent and chemical environment (Figure 4-5).

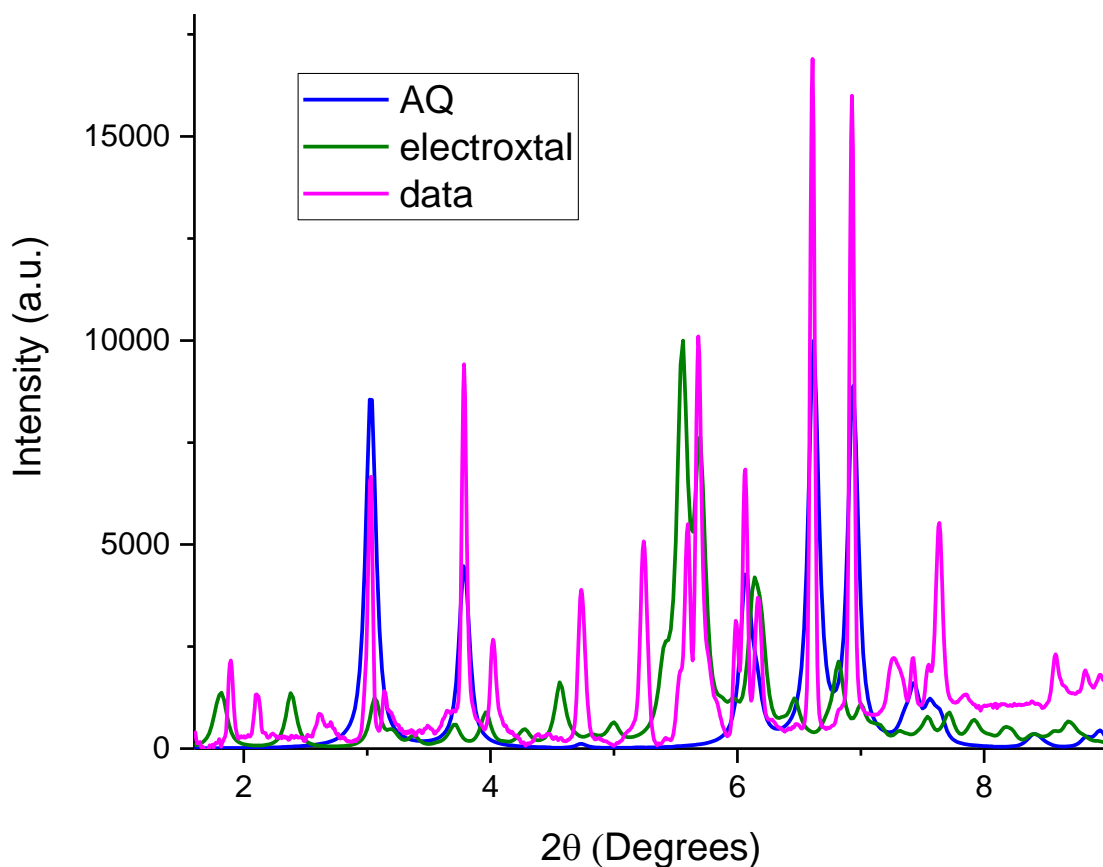
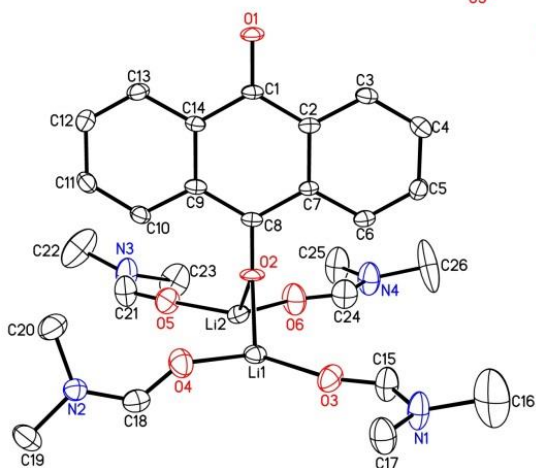


**Figure 4-5:** Powder XRD comparison of the pattern that arises at low voltages in a battery; AQ; and the electrocrystallized product.

Solvent and electrolyte incorporation occurred within this “1D coordination polymer”. The supporting electrolyte atomic positions were disordered (Figure 4-6).

The space group changed from  $P2_1/c$  to  $P2_12_12_1$  and the crystal symmetry increased from monoclinic to orthorhombic. The electrocrystallized product had a more linear packing of AQ anions (Figure 4-7A) as compared to the herringbone packing of neutral AQ (Figure 4-7B). Attempts with battery-like conditions were unsuccessful, most likely because the anthraquinone was not soluble enough in EC:DEC.

(A)



(B)

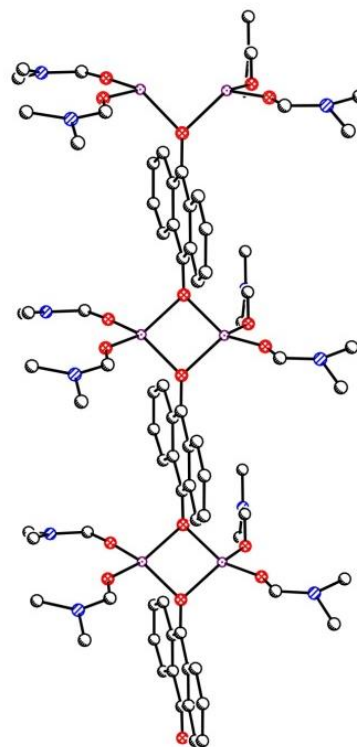


**Figure 4-6:** Single crystal structure of electrocrystallization product as (A) a single entity with the perchlorate ion in proximity and (B) as a linear chain.

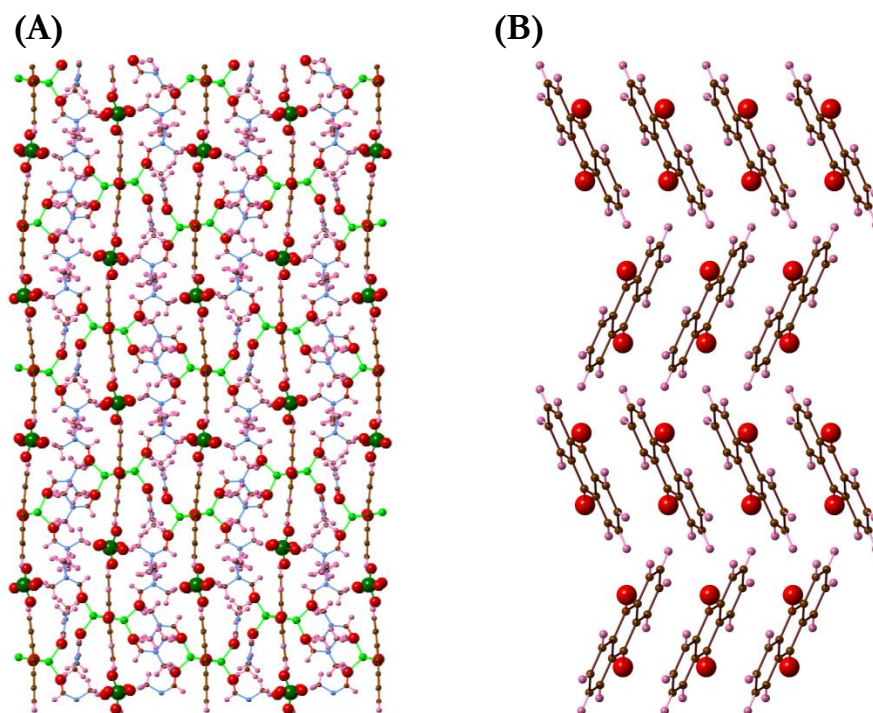


**Figure 4-7:** Demonstration of the significant change in packing between **(A)** the electrocrystallization product and **(B)** AQ, both displayed along the a-axis.

4-3-4. *Chemical reduction.* When chemically reduced, the AQ solution turned a deep blood red, a color change that seemed promising based on the other examples of possible reduction. The neutralization with HCl yielded a yellow-green powder. If I had reacted the hydroquinones with LiOH or Li<sub>2</sub>O<sup>8</sup>, it might have afforded the lithium salt, but the formation of water from the salt exchange might have led to a hydrated structure instead. At least in the mid-angle range there were peaks that possibly correlated to the reduced species (Figure 4-8). However, there is still a significant contribution from AQ, either unreacted or air-oxidized at the diffractometer.

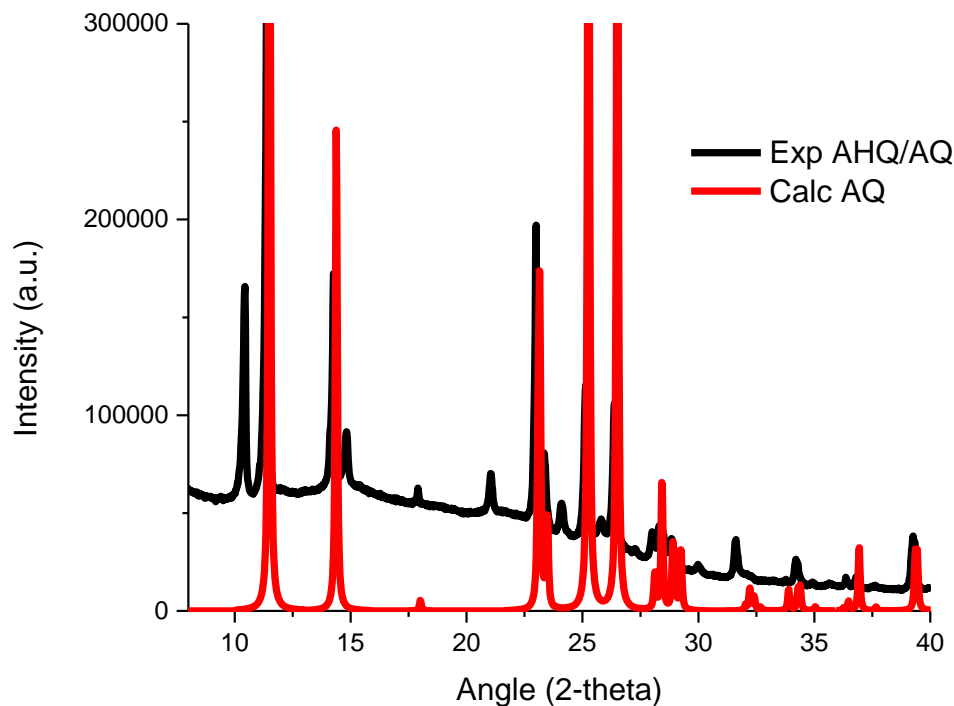


**Figure 4-8:** Comparison of XRD patterns from chemically reduced AQ and the known diffraction pattern of AQ.

#### 4-4. Discussion

There are many pitfalls to collecting adequate data for solving a crystal structure from a powder pattern – systematic and accidental absences, peak overlap, and low scattering power. In most of the cases brought up in this chapter, we have encountered an additional complication – we are not isolating the same material generated *in operando*! If we could collect diffraction data from the reduced AQ that has low background, high peak resolution, and no impurity peaks, we could stand a fighting chance. Robin Shirley famously wrote<sup>9</sup>, “Powder indexing works beautifully on good data, but with poor data it will usually not work at all.” Without a properly indexed unit cell, further structure determination cannot proceed. We also require a

good model of the crystal in order to do a Rietveld refinement. Without chemical intuition about the reduction complex structure, we have reached the edge of feasibility.

#### **4-5. Conclusions**

All of these ex-situ approaches to the lithiated species support the importance of *operando* studies. At least in the case of the single crystal isolated from the electrocrystallization reaction, solvent and supporting electrolyte are certainly incorporated within the crystal structure of the reduced anthraquinone.

Though apparent changes are visible in the *operando* data, the diffraction peaks do not have enough chemical specificity to indicate definite atomic placements. The organic redox-conductive molecules that were investigated here have just enough degrees of freedom to make a single crystal solution from powder diffraction intractable with the current data. Fortunately, the X-ray techniques I learned in undertaking this project were directly transferrable to other battery systems, as I will discuss in the following chapters.

## REFERENCES

- 
1. Walker, W.; Grugeon, S.; Mentre, O.; Laruelle, S.; Tarascon, J. M.; Wudl, F. *J. Am. Chem. Soc.* **2010**, *132*, 6517–6523.
  2. David, W. I. F.; Shankland, K. *Acta Crystallogr. A.* **2008**, *64*, 52–64.
  3. Ward, M. D. *Supramolecular Architecture*, ed. T. Bein, Am. Chem. Soc., Washington, DC, **1992**, *499*, 231–243.
  4. Montgomery, L. K. *Organic Conductors: Fundamentals and Applications*, ed. J.-P. Farges, CRC Press, New York, **1994**, *4*, 138-143.
  5. Cheek, G. T. *J. Electrochem. Soc.* **1982**, *129*, 2488.
  6. Lucht, B. L.; Collum, D. B. *Acc. Chem. Res.* **1999**, *32*, 1035–1042.
  7. Batail, P.; Boubekeur, K.; Fourmigué, M.; Gabriel, J.-C. P. *Chem. Mater.* **1998**, *10*, 3005–3015.
  8. Kaduk, J. A. *Acta Crystallogr. Sect. B: Struct. Sci.* **2000**, *56*, 474–485.
  9. Shirley, R. *NBS Spec. Publ.* **1980**, *567*, 361.

## CHAPTER 5

### OPERANDO X-RAY SCATTERING AND SPECTROSCOPIC ANALYSIS OF GERMANIUM NANOWIRE ANODES IN LITHIUM-ION BATTERIES

The majority of this work previously appeared in a peer-reviewed publication:

Silberstein, K. E.; Lowe, M. A.; Richards, B.; Gao, J.; Hanrath, T.; Abruña, H. D.

*Langmuir* **2015**, *31*, 2028–2035.

#### 5-1. Introduction

We chose to study germanium nanowires as an anode material in LIBs for several reasons. Conventionally, in LIBs, graphite serves as the anode (often opposite a lithiated metal oxide cathode such as  $\text{LiCoO}_2$ ) with a modest specific capacity of  $372 \text{ mAh/g}^1$ . Traveling down the column of the periodic table from carbon, we find silicon and germanium, both of which possess significantly higher theoretical capacities of  $4200$  and  $1600 \text{ mAh/g}$ , respectively. High-capacity anode materials will allow for a diminution of the amount of active material required in the cell, thereby decreasing the weight, volume, and cost of a commercial battery. Prior to battery efforts, researchers studied the kinetics of lithium diffusion in germanium because semiconducting materials were convenient for measuring resistivity and maintaining stable dislocations<sup>2,3,4</sup>. At  $400^\circ\text{C}$ , there are several thermodynamically accessible,

electrochemically reversible Ge-Li alloy phases, including  $\text{LiGe}$ ,  $\text{Li}_9\text{Ge}_4$ , and  $\text{Li}_{15}\text{Ge}_4$ , that form under chronopotentiometric conditions<sup>5</sup>.

More recently, the mechanism of lithium (de)insertion in silicon at room temperature has been studied by pair distribution function analysis and solid-state NMR spectroscopy<sup>6</sup>. These methods showed a transition from crystalline to amorphous silicon as lithium was inserted and removed electrochemically. At full depth of discharge,  $\text{Li}_{15}\text{Si}_4$  was formed, while at shallow depths of discharge (85mV versus  $\text{Li}/\text{Li}^+$ ), residual crystalline silicon persisted as nucleation sites for partial recrystallization upon cycling.

Early studies have shown that lithium ions have a higher diffusivity in single-crystalline germanium than in silicon<sup>7</sup>. *In situ* X-ray diffraction (XRD) and X-ray absorption spectroscopy (XAS) studies have been carried out on the electrochemical insertion of lithium into germanium in thin films<sup>8,9</sup> and crystalline micron-sized particles<sup>10</sup>, but thus far, such analysis has not been applied to nanowires.

Nanostructured germanium has captured the attention of many research groups for battery applications<sup>2,11,12,13,14,15,16,17</sup> because nanostructuring has been shown to mitigate the macroscopic mechanical stresses that arise from the lithium incorporation/removal processes that, in turn, lead to electrode pulverization. These studies show that, analogously to silicon, crystalline germanium is transformed to crystalline  $\text{Ge}_4\text{Li}_{15}$  upon full insertion of lithium, but that upon removal of lithium, germanium becomes amorphous. One of our objectives was to investigate whether

short-range (atomic-scale) order could be maintained within the germanium nanowires upon cycling to different depths of discharge.

A significant advantage of our experimental setup is that we can monitor structural and electrochemical changes within a real battery in real time throughout the course of charge and discharge. That is, we can carry out *operando* studies. High energy X-rays, generated at synchrotron sources, are useful for examining dynamic systems such as ours<sup>1</sup>. Our coin cell design limits the amount of non-active material in the beampath, so the high photon flux allows passage through other components of the battery with minimal interference and attenuation. Thus, we can use XRD to monitor changes in crystal structure within the germanium nanowires as a function of lithium incorporation (state-of-charge). Our work benefits from supplementing the XRD data with Fourier-transform extended X-ray absorption fine structure (EXAFS) analysis of XAS data. XRD provides direct information about crystalline phases within a system, while EXAFS yields information about domains that are crystalline, have short-range order, or are even amorphous. It should be noted that the foundational work on Fourier analysis of the extended fine structure region of X-ray absorption spectra was conducted on amorphous and crystalline germanium<sup>18</sup>. Analysis of the X-ray absorption near-edge structure (XANES) region of the absorption spectrum supplements the EXAFS data by providing information about average oxidation state and local geometry around the germanium photoabsorber<sup>19,20,21</sup>. Since the incident beam energy is tuned to the germanium K-

edge for XAS measurements, interference from other coin cell components is largely mitigated.

## 5-2. Experimental Details

*5-2-1. Synthesis of Germanium Nanowires.* Germanium nanowires were synthesized using a supercritical fluid—liquid—solid (SFLS) method, utilizing gold nanoparticles as seeds<sup>22</sup>. The nanowires were prepared by injecting 10.4 mL of a solution containing 320 mM diphenylgermane (Gelest), 3 nm dodecanethiol-capped gold nanoparticles at a Au:Ge ratio of 1:2000, and benzene into a 15mL stainless steel reactor. Typical reaction times were 20 minutes at 400°C and 34.5 MPa. The reaction produced 140 mg of Ge nanowires, corresponding to a 55% yield. Based on structural analysis using scanning electron microscopy (SEM), the nanowires had an average diameter of  $38 \pm 19$  nm (Figure 5-1).

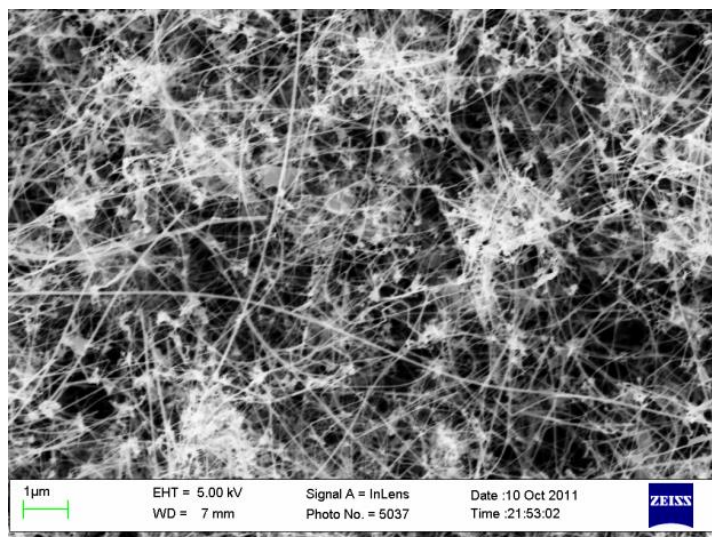


**Figure 5-1:** Scanning electron micrograph of as-prepared germanium nanowires.

In order to verify the degree of crystallinity of the as-prepared germanium nanowires prior to *operando* studies, Raman scattering (785nm incident radiation) was collected from a pristine sample within a  $\sim 1$  micron volume element. Based on shifts reported in the literature<sup>23</sup> (crystalline bulk germanium has a peak at  $300\text{cm}^{-1}$ ), the data indicate that the nanowires are predominantly amorphous, although the peak is sufficiently broad to support the presence of some fraction of crystalline domains (Figure 5-2). A representative high-resolution TEM image of a single nanowire shows that the crystalline domains are localized within the nanowire core (Figure 5-3).

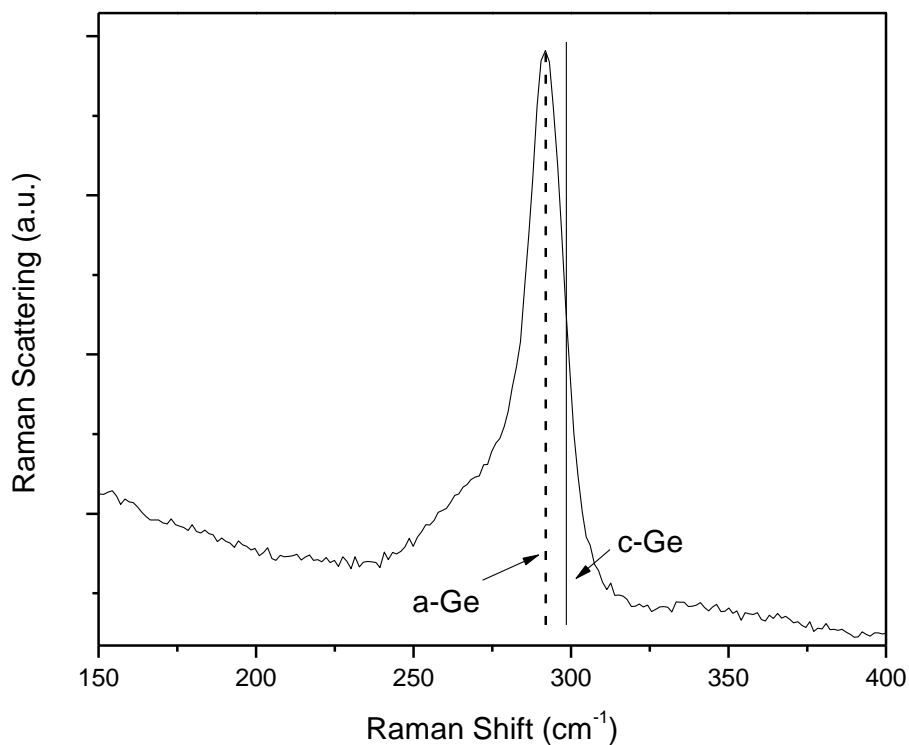


**Figure 5-2:** Raman scattering from a sample of Ge nanowires.

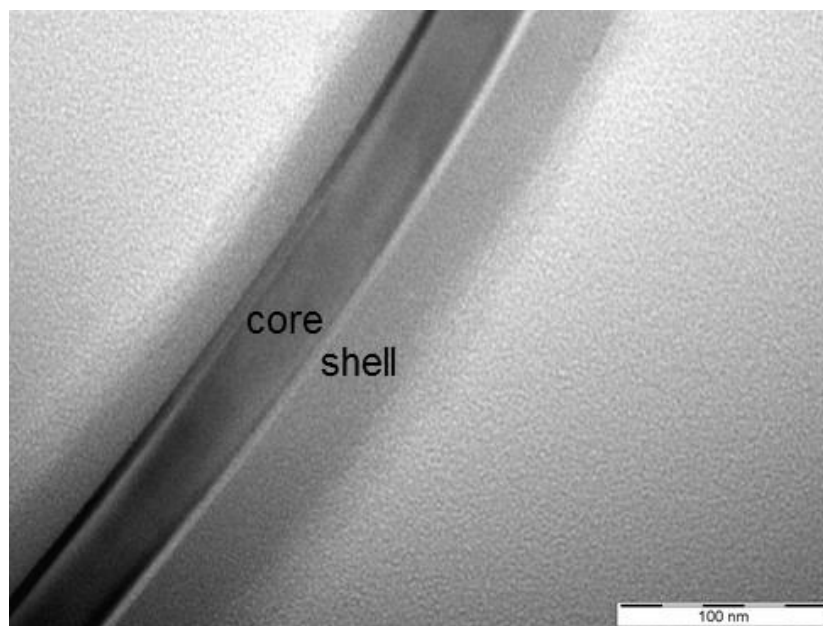


**Figure 5-3:** Transmission electron micrograph of a single germanium nanowire, illustrating the amorphous shell and crystalline core of the wires.

*5-2-2. Sample Preparation.* Germanium nanowires, synthesized by the above method, were intimately mixed with carbon black (Super P-Li, Timcal Ltd), and polyvinylidene difluoride (PVDF) used as a binder (7:2:1 mass ratio). The mixture was suspended in 50 $\mu$ L of N-methyl-2-pyrrolidinone (NMP), cast on a copper current collector, and dried under vacuum overnight. Circular electrodes were cut out from the film and used within a coin cell modified for *operando* studies (Figure 2-1). The electrolyte solution was 1M LiPF<sub>6</sub> in equal parts ethylene carbonate to diethyl carbonate (EC/DEC). Modified coin cells were assembled as previously described (Section 2-1-3).

*5-2-3. X-ray Methods.* X-ray studies were carried out at CHESS. Powder XRD measurements were performed in transmission mode at station A2 (incident energy

calibrated to the antimony K-edge, 30.491keV, or  $\lambda=0.406626\text{\AA}$ ) using a 2D amorphous silicon large-area detector (General Electric) and station F3 (incident energy calibrated to the molybdenum K-edge, 20keV, or  $\lambda=0.6199\text{\AA}$ ) using a Quantum-4 CCD area detector (ADSC). The diffraction rings were integrated radially to produce 1D diffraction patterns using the software package Fit2D<sup>24</sup>.

Sequential quantitative phase analysis<sup>25</sup> was performed on each raw diffraction pattern collected at station A2 out to  $28^\circ 2\theta$ , without any manual background subtraction or correction, using the seqGSAS utility within the GSAS/EXPGUI package<sup>26</sup>. Reflection intensities were extracted by the Rietveld method within EXPGUI. Profile fitting using the pseudo-Voigt function was performed on the first diffraction pattern of each dataset to establish reasonable profile parameters, and then these values were held for subsequent phase fraction determination. Along with the crystalline phase fractions of the relevant known Ge-Li crystal structures<sup>27</sup>, the background was refined via the least-squares method for each pattern with 15 terms in a shifted Chebyshev polynomial. The phase fractions were not restrained to sum to 100% since an unquantified amount of amorphous germanium was present initially. To remove the effect of the fluctuation of the incident beam, the phase fraction of the copper, which was a constant presence in the beampath, was also refined for each pattern and used to normalize the Ge-Li phases.

XAS data were collected at station C1 from 100eV above the edge out to  $k=12$  (around the K-edge of Ge, 11.103keV) using nitrogen-filled ion chambers. Absorption spectra were Fourier-transformed and plotted in  $r$ -space versus the voltage profile, after background subtraction and phase correction for a germanium photoabsorber, using the software program Athena employing  $k^2$ -weighting (Figure 5-4)<sup>28</sup>. Thermal disorder was not considered as a contributor to decreased amplitude in the EXAFS spectra since the experiments were performed under effectively isothermal conditions<sup>29</sup>. Additionally, absorption data between  $k=10$  and  $k=12$  were not included in the analysis, due to excessive noise from instabilities in the synchrotron that could not be addressed within the timeframe of the experiments. Fitting of the EXAFS spectra to known Ge-Li structures<sup>24</sup> was attempted, but due to the weak scattering power of lithium, distinct atomic correlation distances were not obtained.

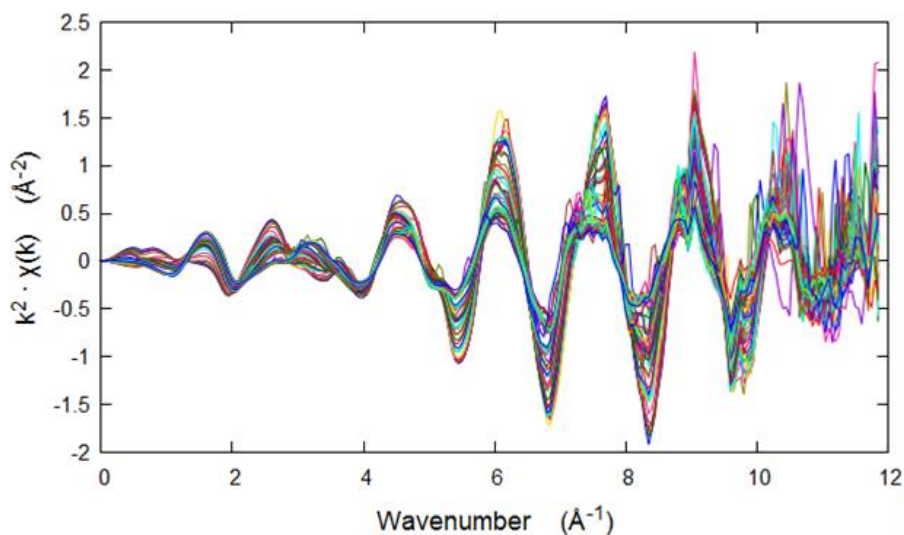


**Figure 5-4:** Overlaid EXAFS data in  $k$ -space,  $k^2$ -weighted, for full discharge. Each colored line is a different spectrum. Fourier transformation was carried out on data from  $k=3.000$  to  $9.983$  since the data become noisy after  $k=10$ .

For analysis of the XANES region (Figure 5-5), the position of the absorption edge ( $E_0$ ) was set to the zero of each spectrum's second derivative (Figure 5-6), and the position of each absorption coefficient maximum ( $E_{\text{max}}$ ), also known as the “white line” peak, was tabulated in Athena.

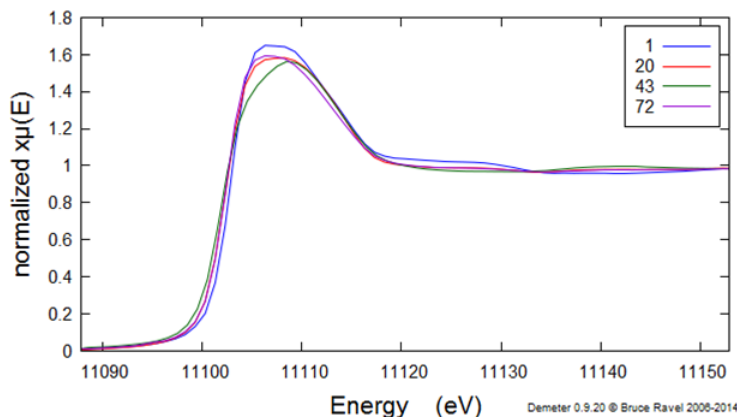


**Figure 5-5:** Selected Ge K-edge XANES spectra from the cell cycled to 0.01V, illustrating the shift in the absorption edge and in the “white line” peak position. The scan number for each XANES spectrum is consistent with the EXAFS spectra in Figure 15-14B.

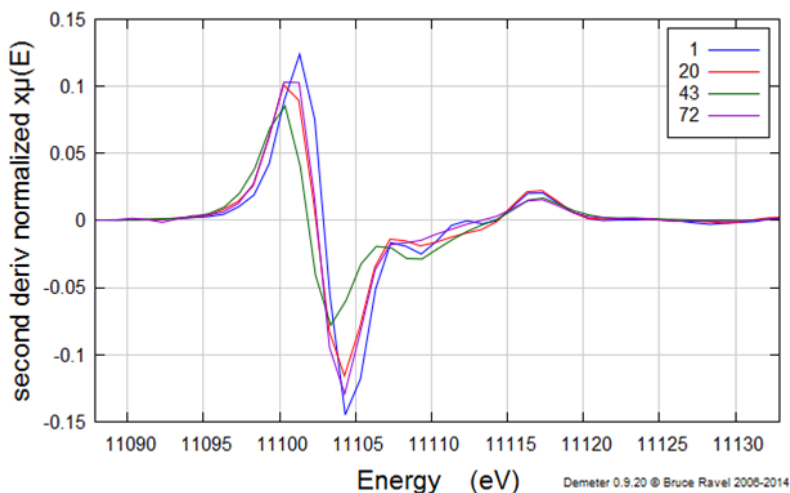


**Figure 5-6:** Second derivative of selected Ge K-edge absorption spectra from the cell cycled to 0.01V. Each  $E_0$  was selected from its  $y = 0$  intercept. The scan number for each spectrum is consistent with the EXAFS spectra in Figure 15-14B.

*5-2-1. Electrochemistry.* In all cases, the assembled coin cell was mounted in the beam path and attached to a VersaSTAT 3 potentiostat/galvanostat (Princeton Applied Research). Chronopotentiometric cycling of separate coin cells at current densities equivalent to an effective C-rate of 0.036, 0.06, and 0.086 (60, 100, and 143mA/g, respectively) between 0.01 and 3V allowed for the exploration of the full range of Ge/Li interactions by XRD and XAS. Further investigation of structural dependence on depth of discharge was carried out at 0.086C (143mA/g) between 0.3 and 3V. Extended coin cell testing was carried out on a multichannel battery cycler (Arbin) between 0.01 and 3V and between 0.3V and 3V.

### **5-3. Results**

*5-3-1. Diffraction.* From our initial XRD studies at 30keV, we found that crystalline domains exist within the nanowires prior to voltage cycling. While discharging at a very slow rate (60mA/g), the crystalline domains remained virtually untouched (Figure 5-7A). There is only a slight decrease in the Ge diffraction peak heights, and the specific capacity of the discharge is 1114mAh/g. When cycling another cell at a slightly higher rate (100mA/g), we were surprised to observe a higher discharge capacity (1364mAh/g). By increasing the electrochemical driving force, more of the active material became kinetically accessible to lithium insertion. Also, there was a dramatic decrease in peak height near the end of the more rapid discharge,

which indicated that the crystalline domains within the nanowires become amorphous when fully inserted with lithium ions (Figure 5-7B).

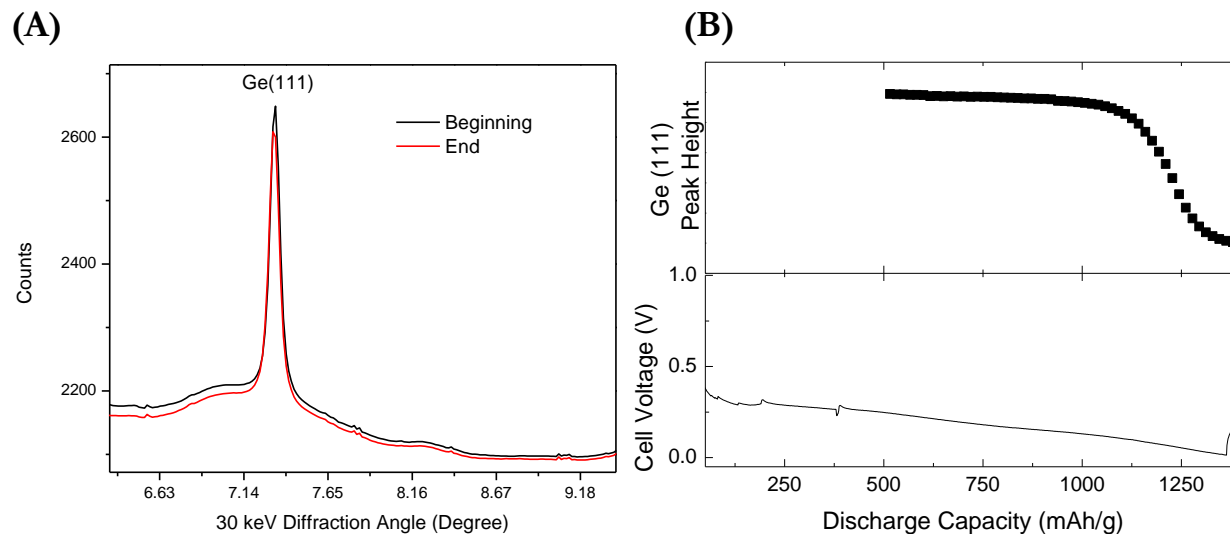


**Figure 5-7:** (A) Ge(111) peak at the beginning and end of a 60mA/g rate discharge. (B) Intensity of Ge(111) peak plotted with the corresponding discharge profile at 100mA/g rate.

A full voltage cycle with diffraction patterns obtained at regular intervals at 20keV allowed for a more detailed analysis of the transitions in structures. Each diffraction pattern was normalized to the peak intensity at  $2.27^\circ$  which corresponds to a constant presence of Kapton. This internal reference allowed for the effective removal of time dependence of the incident beam intensity. Since the final scan had no distinct features, it was used for background subtraction. Remnants of the peaks from Kapton, lithium metal, nickel foam, and stainless steel appeared constantly throughout the data. The colored lines throughout the plot correspond to the indicated points of interest along the voltage cycle (Figure 5-8A, B). Patterns were compared qualitatively to those calculated from known crystal structures of Ge-Li

phases<sup>27</sup>. From this comparison (Figure 5-8C), we saw that the peaks from crystalline Ge remained constant in intensity until 0.2V (second red indicator), at which point the Ge peaks faded. Broad features that arose during the end of the discharge (third red indicator) matched those of Ge<sub>2</sub>Li<sub>7</sub>. At the end of a brief hold at 0.01V (second green indicator), peaks corresponding to Ge<sub>4</sub>Li<sub>15</sub> appeared and persisted until the end of the final plateau in the recharge (third blue indicator). The next scan looked like Ge<sub>2</sub>Li<sub>7</sub>, then and the subsequent four looked like Ge<sub>4</sub>Li<sub>7</sub>. For the remainder of the charge, the system was amorphous. Delithiation appeared to be occurring heterogeneously because the broad features from Ge<sub>2</sub>Li<sub>7</sub> remained evident even as Ge<sub>4</sub>Li<sub>15</sub> formed. Obtaining diffraction patterns at regular intervals throughout two full voltage cycles allowed us to probe structural transitions in even more detail. Each diffraction pattern was normalized to the counts recorded in an upstream ion chamber at the time of acquisition to account for the time dependence of the incident beam intensity. To eliminate image hangover from the GE detector, a dark image was obtained after each diffraction snapshot. In addition, a background diffraction pattern was collected from a coin cell containing all components except for the germanium thin film. The polymer binder and carbon black additive did not contribute significantly to the diffracted intensity. The dark image and background pattern were then subtracted from each scan for the purpose of plotting. For ease of examination of state-of-charge and diffraction pattern, the processed XRD patterns were plotted as a contour plot versus voltage profile from 3 to 15° 2θ. Figure 5-9 presents *operando* XRD patterns

zoomed into the region of interest at 30keV of a germanium nanowire cell over the course of two full discharge/charge cycles. Patterns were fit to known crystal structures of Ge-Li phases<sup>24</sup> (Figure 5-8C). The small peaks at 9.4° and 13.3° correspond to the (110) and (200) peaks of metallic lithium, respectively, while the black lines correspond to the constant presence of copper and nickel phases, from the cell components, that were subtracted. XRD showed that crystalline domains are present within the nanowires prior to voltage cycling. The peaks arising from Ge remained constant in intensity until 0.5V (scan number 50), at which point the Ge peaks began to decrease in amplitude. Having direct evidence from Raman scattering and TEM that there was a significant proportion of amorphous germanium present at the surface of the nanowires, we interpreted the lack of changes in the crystalline germanium diffraction peaks during initial lithiation as an indication that lithium was incorporated preferentially within the amorphous domains of the nanowire. It would not be reasonable (due to the amount of charge involved) to attribute 60% of the cell's discharge capacity to some other mechanism such as solid-electrolyte interface (SEI) formation or lithiation of the conductive carbon additive.

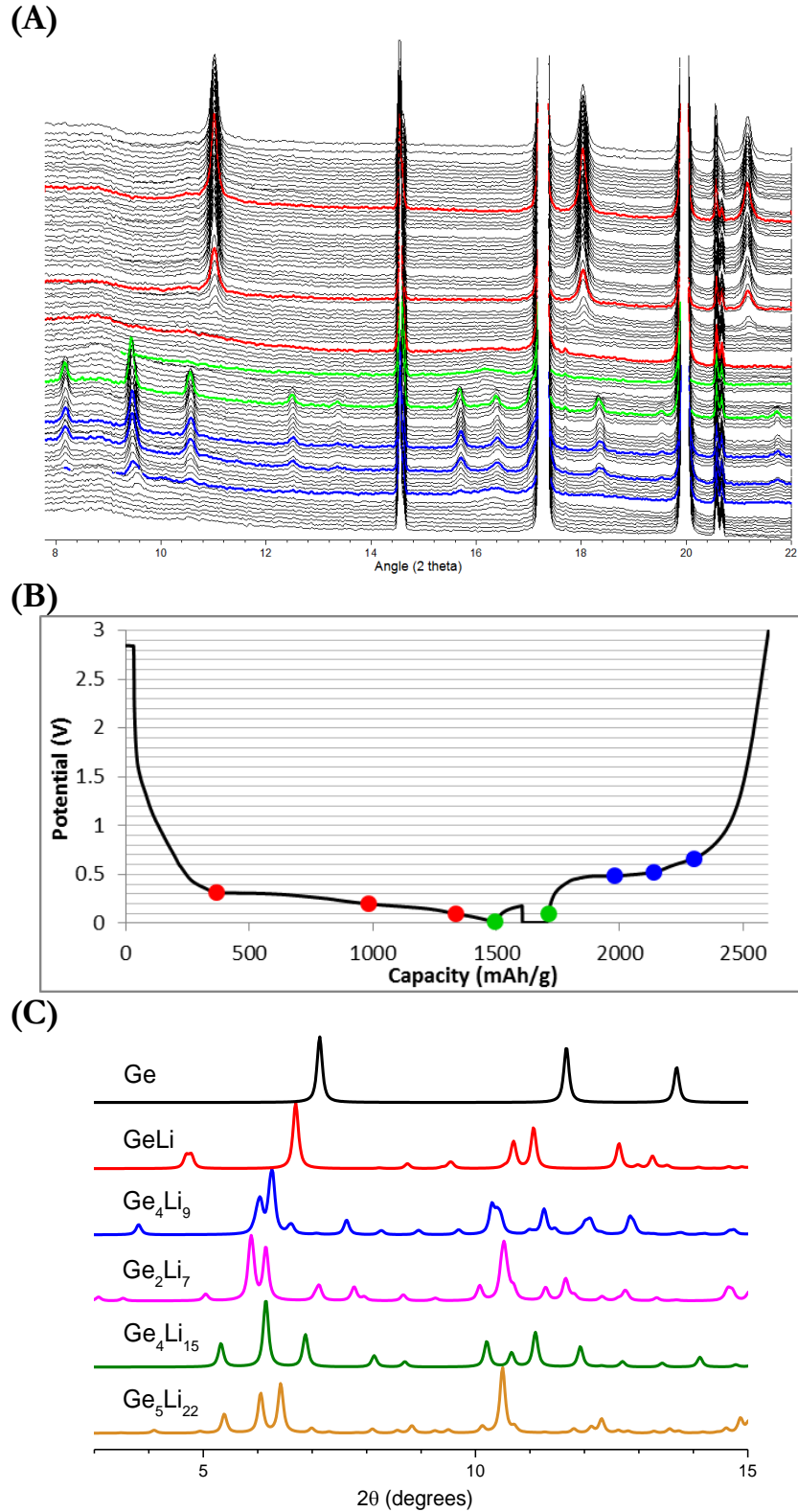


**Figure 5-8:** (A) XRD data for a germanium nanowire battery over the course of a full discharge/charge cycle. (B) Corresponding voltage profile. (C) Calculated XRD patterns of known Ge-Li alloy phases.

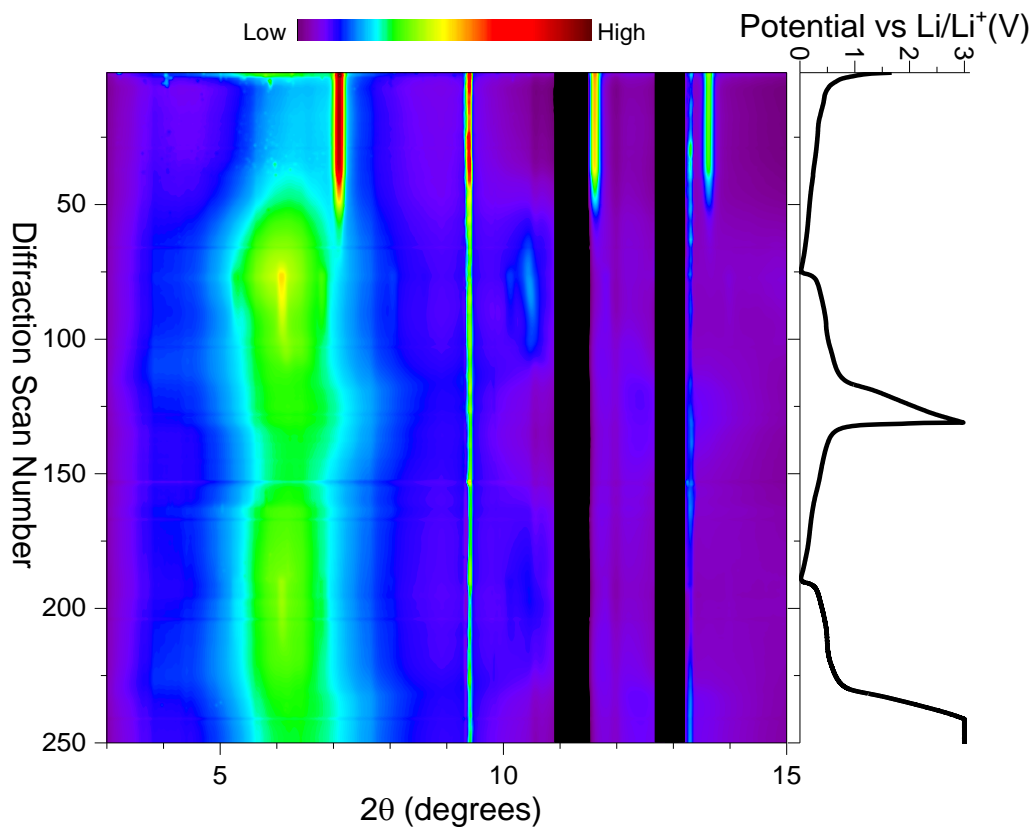


**Figure 5-9:** XRD patterns of germanium nanowire battery over the course of two full discharge/charge cycles.

While the germanium peaks decreased, broad features arose at lower diffraction angles, corresponding to an increased d-spacing within the crystal structure of the nanowires, as lithium was electrochemically inserted. Sequential refinement of the scale factor for each known Ge-Li phase gave the proportion of each known phase (Figure 5-10). Although  $\text{Ge}_3\text{Li}_{22}$  is the most lithiated thermodynamic phase in the Ge-Li phase diagram, we did not observe any intensity that could be attributed to that phase. This is a common observation in the study of silicon and germanium lithiation, and it is attributed to the kinetics of the system<sup>7,9,11</sup>. Even as most of the crystalline Ge

persisted during the first portion of the discharge (around scan number 25), GeLi, Ge<sub>4</sub>Li<sub>9</sub>, and Ge<sub>4</sub>Li<sub>15</sub> phases began to emerge. This would indicate that once the amorphous Ge domains were electrochemically lithiated, they began to crystallize into whichever lithiated phase was kinetically most accessible. The appearance of Ge<sub>2</sub>Li<sub>7</sub> did not occur until the intensity of the crystalline Ge peaks trailed off precipitously (scan number 50). We interpret the evolution of the scattering patterns as an indication that the lithiation proceeded heterogeneously and involved several lithiated stages.

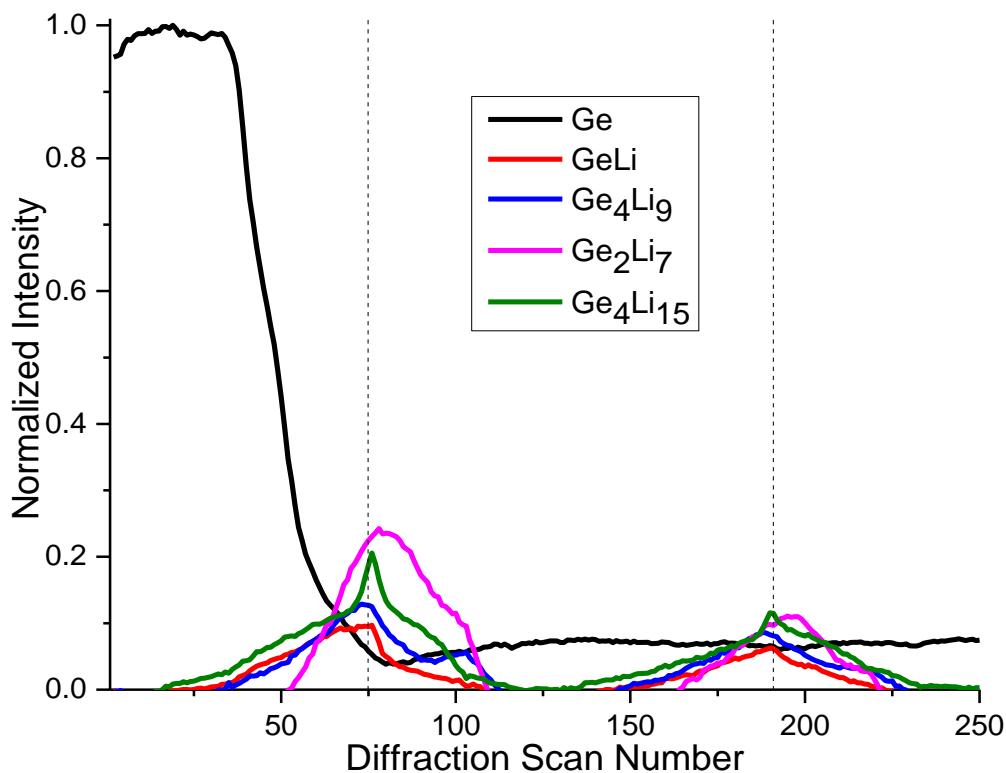


**Figure 5-10:** Phase analysis of each diffraction pattern from two full discharge/charge cycles. Dashed lines indicate the points at which the voltage reaches its minimum throughout the cycling. The electrochemistry is the same as in Figure 5-9.

The proportions of the lithiated phases reached a maximum at full discharge (scan number 75). The presence of crystalline  $\text{Ge}_4\text{Li}_{15}$  is most apparent as indicated by the sharp increase in its phase fraction, though the other phases were still present. Upon recharge, features from the lithiated phases began to decrease while there was a slight return of some crystalline Ge intensity. For the remainder of the charge cycle, sharp diffraction peaks from Ge were no longer evident, indicating that a significant fraction of the initially crystalline cores of the wires had become predominantly amorphous or that the average crystallite domain size was very small.

This is supported by the fact that the sum of the apparent crystalline phase fractions decreased. During the second cycle, it was apparent that the disorder within the system had increased since the proportions of lithiated phases diminished. Again, the transformation proceeded through crystalline lithiated phases up to  $\text{Ge}_4\text{Li}_{15}$ , although domains were smaller as evidenced by the decreased intensity and increased widths of the diffraction peaks. However, there was no evidence indicating the recovery of much crystalline germanium upon recharge, even after the cell potential was held at 3V, until less than  $20\mu\text{A}$  of current were being passed.

To better understand the relationship between depth of (dis)charge and the evolution of the Ge nanowire crystal structure, we studied XRD patterns collected while cycling a battery to a shallower depth of discharge corresponding to 0.3V

(Figure 5-11). Cycling within this limited potential range decreased the practical capacity of the cell by 60%.

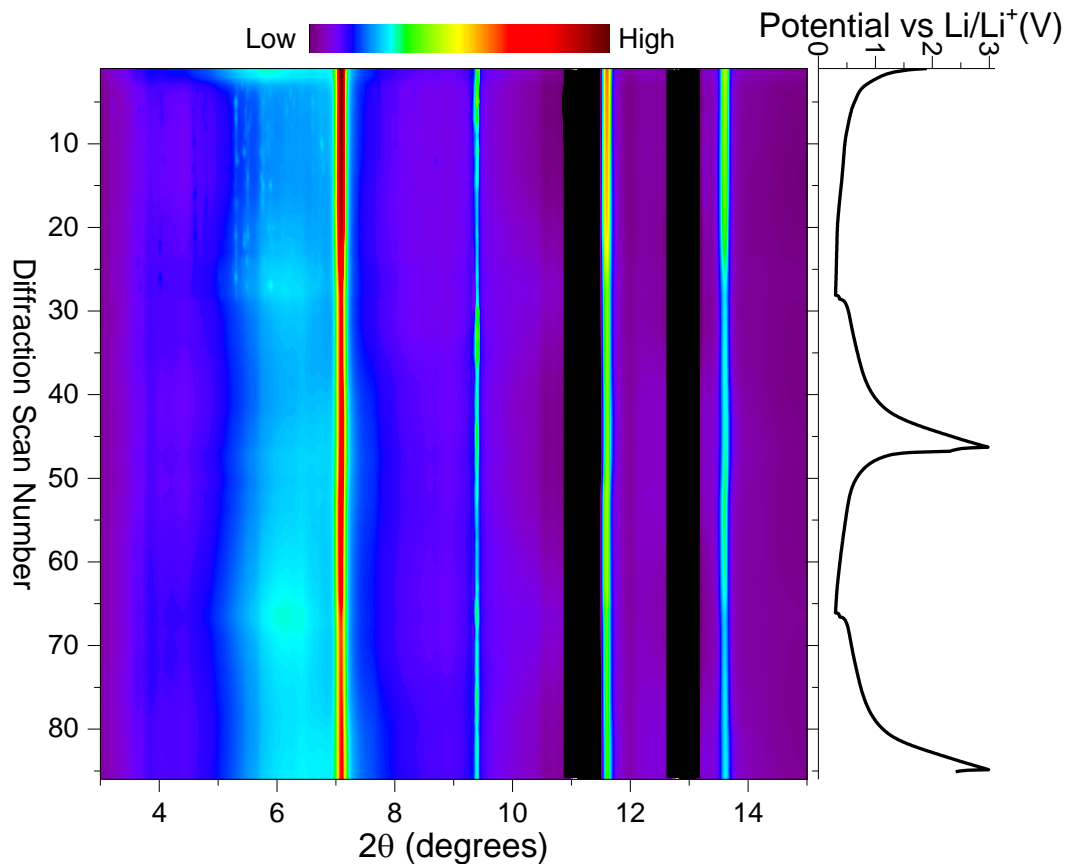


**Figure 5-11:** XRD patterns for a germanium nanowire battery over the course of two discharge/charge cycles to 0.3V showing the persistence of the Ge diffraction peaks.

Once again, the methodology of quantitative phase analysis allowed for a more accessible visualization of the changes in the system as a function of state-of-charge (Figure 5-12). As shown in the previous case, the initial crystallinity remained constant until 0.5V (scan number 15). Between 0.5 and 0.3V, the broad features from a combination of lithiated phases appeared, even as the germanium peaks persisted, albeit at a lower intensity. The germanium phase fraction remained constant during

the first recharge (scan numbers 24 to 42). Surprisingly, there was a slight increase in the germanium peaks' intensity during the second discharge (around scan number 50). Although somewhat speculative on our part, we attribute this increase in crystalline germanium to the reorganization of germanium atoms near the crystalline core even as more lithium was inserted into the amorphous shell. Crystallinity within the nanowires could be maintained, but the proportions of the lithiated phases grew with each discharge. This indicated that the shallow discharge depth and subsequent preservation of the crystalline core slowed down the rate of amorphization, but it would not be enough to prevent gradual amorphization of the nanowires after several cycles.

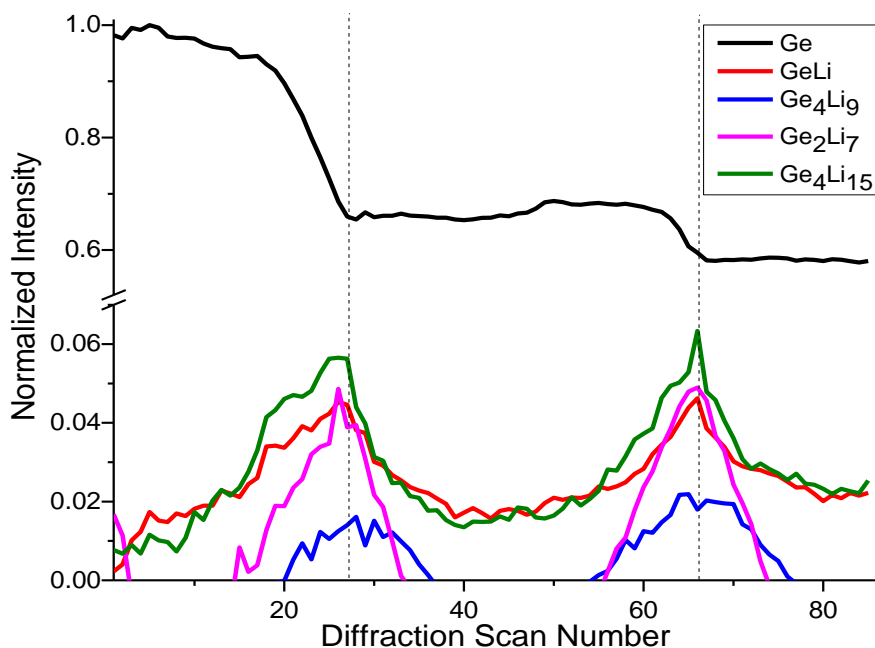


**Figure 5-12:** Phase analysis of each diffraction pattern over the course of two discharge/charge cycles to 0.3V. The lithiated phases are presented on an expanded scale. Dashed lines indicate the points at which the voltage reaches its minimum throughout the cycling. The electrochemistry is the same as in Figure 5-11.

5-3-2. *Absorption.* The transitions observed via XRD were supported by EXAFS analysis of XAS data at both current densities of 100 mA/g (Figure 5-13A) and 143 mA/g (Figure 5-13B). Throughout the discharge, three coordination shells were clearly present at R-values of 2.4, 4.0, and 4.7Å, corresponding to highly-ordered (i.e. crystalline) germanium. Amorphous germanium tends to only show the first shell<sup>15</sup>. (The apparent “shell” at 3.3Å arose from the ringing of the Fourier transform and should not be considered in the analysis.) The amplitude of the first shell remained constant until 0.5V, after which it decreased in tandem with the voltage. This is consistent with XRD evidence of the loss of crystallinity in the Ge wire cores. The first shell position did not shift appreciably, and the second and third shell intensities faded by the end of the discharge. Within the various known Ge-Li alloy structures, the nearest neighbors to a Ge point scatterer are all around a distance of 2.5Å. Static disorder and lithium proximity within the alloy would both contribute to a decreased first shell amplitude. Since a lithium atom has a significantly lower electron density than a germanium atom, the intensity of the backscattered photoelectron will be greatly diminished. Given the similarity in electrochemistry among samples, the low-voltage region of the cycle likely had major contributions from the Ge<sub>4</sub>Li<sub>15</sub> phase. By the end of the charge, only the shell at 2.4Å remained, which indicated that the germanium was amorphized upon removal of lithium. The EXAFS amplitudes decayed more rapidly during discharge when the higher current density was applied, consistent with the XRD data.

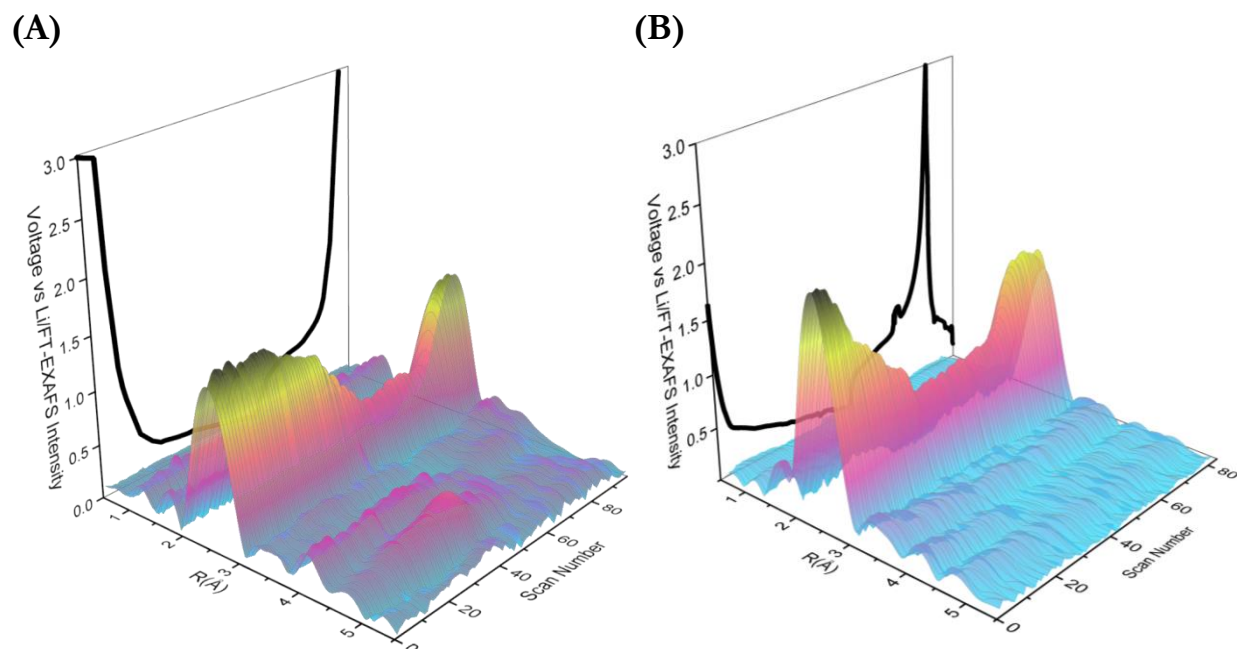


**Figure 5-13:** Fourier-transformed EXAFS region at Ge K-edge over the course of a full discharge/charge cycle at current densities of **(A)** 100mA/g and **(B)** 143 mA/g.

In examining the EXAFS spectra from the first cycle of a coin cell cycled to 0.3V, we found that, similarly to the case of full discharge, the first shell amplitude remained steady up to 0.5V (Figure 5-14A). The second and third discharge/charge cycles, however, showed a strikingly different response in the EXAFS spectra (Figure 5-14B). The first shell amplitude tracked the voltage while the second and third shells persisted throughout several cycles to 0.3V, which confirmed the retention of some crystallinity. This meant that the decrease in the first shell peak height was likely due to the incorporation and removal of weakly backscattering lithium ions. If overall static disorder were increasing significantly, the higher-order scattering peaks would fade as they did in the fully discharged cell. Since EXAFS analysis gives an average picture of the photoabsorber's chemical environment, the data show that when the

cell is cycled to a shallow cutoff voltage, some crystalline germanium domains persist while the nanowires incorporate lithium. Both amorphous and crystalline Ge will exhibit a first-shell peak. Since the amplitude is dependent on static disorder and lithium content, there will not be much change in the first shell until a significant amount of amorphization of the crystalline core or lithiation has taken place. On subsequent cycles, changes brought about by (de)lithiation are more clearly discernable because enough of the crystalline core has been amorphized.

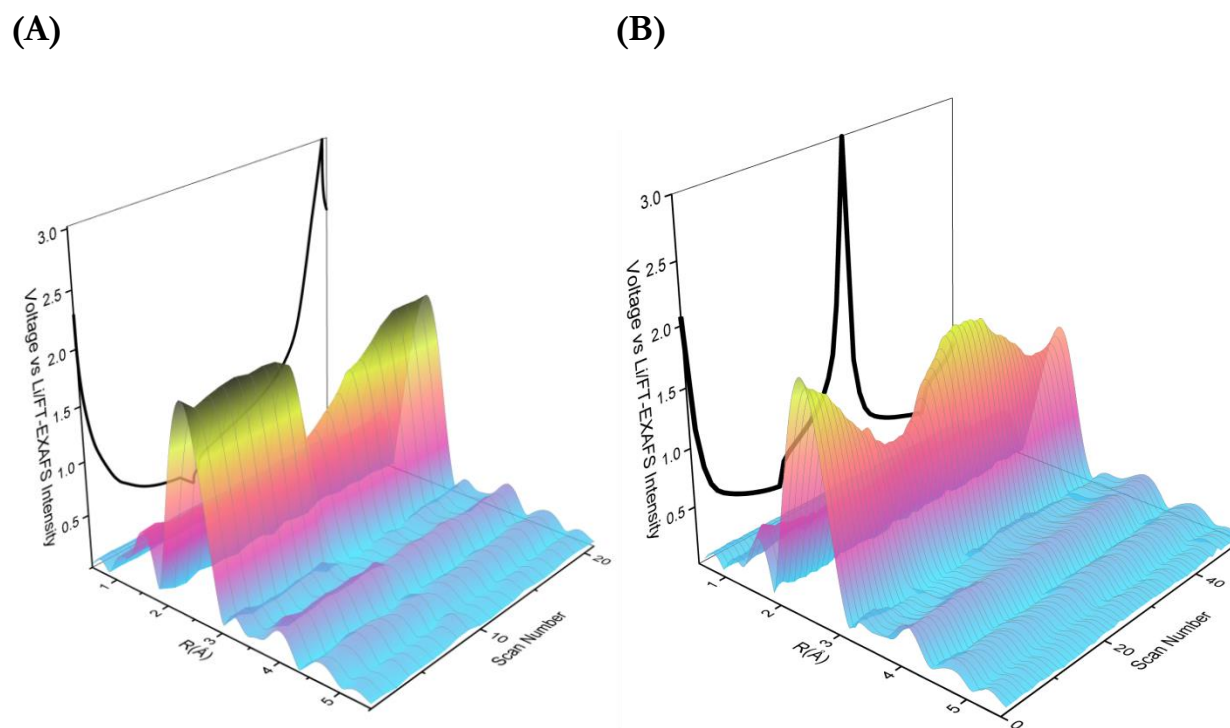


**Figure 5-14:** Fourier-transformed EXAFS region at Ge K-edge over the course of (A) the initial and (B) two successive discharge/charge cycles to 0.3V.

Variations in the XANES region of the absorption spectra as a function of the state-of-charge (Figure 5-15) further support the fact that germanium's local chemical environment is changing throughout cycling. Upon discharge,  $E_0$  gradually shifts to

lower energy, indicating Ge reduction<sup>16,17</sup>. At deeper discharge, more of the germanium is being reduced, and thus the average oxidation state is less positive. This leads to a larger shift in the edge position for discharge to 0.01V (Figure 5-15A) than to 0.3V (Figure 5-15B). Only in the case of shallow cycling, does  $E_0$  reach its original value upon recharge. Upon discharge,  $E_{\max}$  gradually shifts to higher energy, indicating greater electron density in the previously unoccupied density of states<sup>16,18</sup>. Again, the magnitude of these changes is scaled by the depth of discharge.

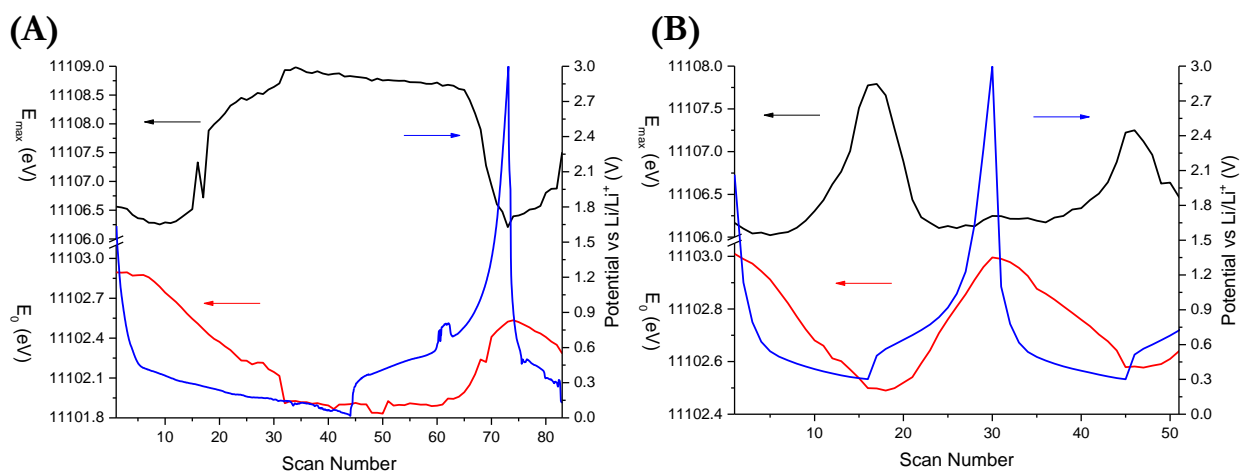


**Figure 5-15:**  $E_{\max}$  (black),  $E_0$  (red), and cell potential (blue) of the XANES region corresponding to the absorption spectra that contributed to **(A)** Figure 15-13B and **(B)** Figure 15-14B, respectively.

*5-3-3. Cycling.* The two voltage cutoff ranges implemented in the *operando* studies were used to test how the preservation of the crystalline core impacted cyclability. The first 10 cycles with the lower voltage cutoff had significantly better capacity retention than those of the cell cycled to full depth of discharge. Surprisingly, however, the practical capacity faded much more quickly for the coin cell with the limited voltage range upon extended cycling. This result is analogous to what was found in the

*operando* organic work (Chapter 3): the system that is the best-behaved electrochemically might not be as well-defined structurally. Though we were able to limit amorphization by limiting the voltage window, loss of crystallinity was clearly not the operative mechanism of long-term capacity fade. In fact, one might surmise that fully amorphized material would cycle more readily since lithiation appeared to be more facile into the amorphous shell of the germanium nanowires than into the crystalline core.

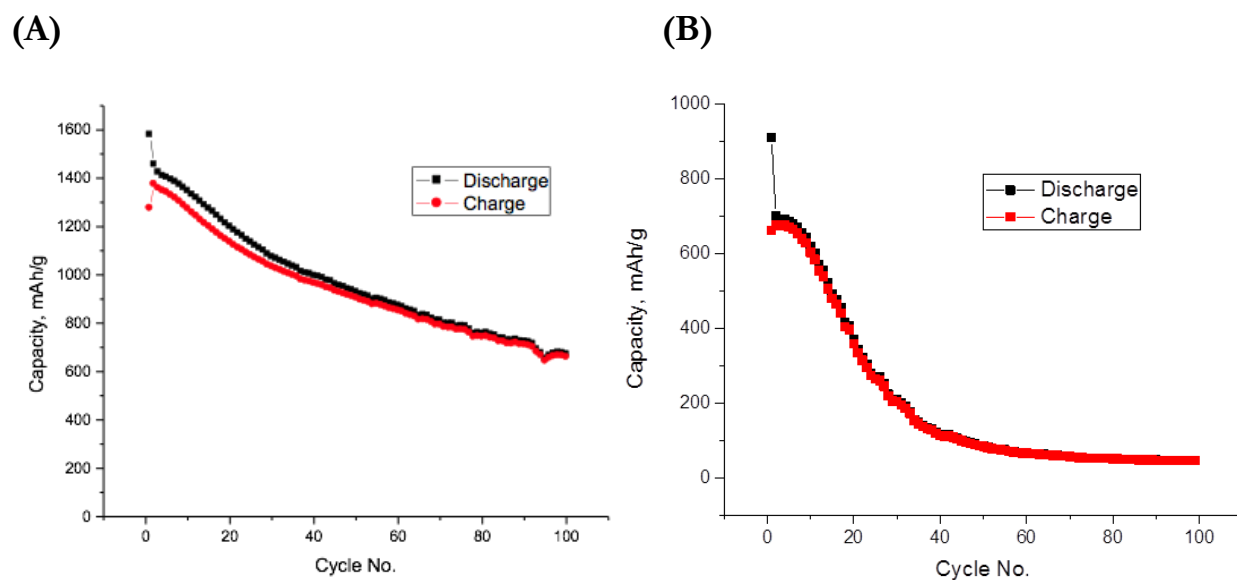


**Figure 5-16:** Extended galvanostatic cycling data with voltage cutoff ranges of 3V to (A) 0.01V and (B) 0.3V.

#### 5-4. Discussion

The delayed decay in the crystalline germanium peaks both in the XRD and EXAFS data during the first discharge, whether to full or intermediate depth, suggests that lithium is preferentially incorporated within the initial amorphous regions of the nanowire. Early studies indicated that as lithium diffuses into germanium, it is

attracted to vacancy sites. The density of vacancies or dislocations will affect the rate of lithium diffusion<sup>3</sup>. By its very nature, amorphous germanium should have more vacancies than crystalline germanium, so ion pairing between  $\text{Li}^+$  and “negative” vacancies will be more favorable in amorphous Ge. Lithium acts as an interstitial impurity within the germanium matrix. Since the initial crystallinity of the nanowire is not uniform, heterogeneous lithiation is likely to occur<sup>5</sup>.

Additionally, the electrochemical insertion and removal of lithium ions into crystalline germanium domains will leave the host in an amorphous state if driven to full discharge. The volume expansion, on the atomic scale, that occurs in the transition from germanium to  $\text{Ge}_4\text{Li}_{15}$  is too large to prevent amorphization, and cannot be avoided by nanostructuring. However, this “breaking-in” process can be delayed if the battery is kept from cycling too deeply or quickly, though this limits the overall capacity of the cell by 60%. In the case of incomplete charge/discharge (i.e. cycling to 0.3V vs 0.01V vs Li), the preserved crystalline domains might serve as nucleation points for recrystallization of germanium as the lithium is removed. A similar phenomenon occurs in the case of cycling silicon to an intermediate cutoff voltage<sup>7</sup>. However, not all capacity is lost, meaning that molecular structural integrity need not be maintained for charge storage. As shown in the cycling data, capacity fade over many cycles cannot be ascribed to merely the loss of crystallinity.

Our analysis of the XRD data hinges on several assumptions: (i) that the anode material is homogenous near the window; (ii) that the only crystalline domains within

the beam path are Ge, Ni, Cu, Li, and Kapton; and (iii) that the rest of the system is unaffected by the incident X-rays. If the anode were not uniform, our observations would only apply to the small area of the cell probed by the X-ray beam. We do not believe that to be the case, since the electrochemistry matches the phase transitions quite well. Also, shifting the beam position to a previously unexposed region of the cell yielded essentially the same diffraction patterns. All the peaks that are apparent correspond to known phases of the cell materials, so we feel confident that the XRD data support our conclusions. Since atomic positions were held at published values during the phase analysis, it is possible that there are other Ge-Li configurations present.

There is always the concern that the high flux of X-ray photons through the cell could lead to radiation damage, but we limited the exposure of the sample cell as much as possible during XRD data collection by taking short (~60 second) scans every ten minutes and closing the shutter while the battery cycled. Since each discharge/charge cycle takes several hours to complete, these snapshots still give a full picture of the dynamics of the process. Though the X-ray exposure is constant during XAS measurements, the spectroscopic changes occur in tandem with the electrochemistry and not with the extent of X-ray exposure.

## 5-5. Conclusions

We have studied the phase transformations within germanium nanowires throughout the course of LIB cycling using *operando* X-ray techniques. Such observations could only be made using *operando* analysis. We are able to track every structural change along the voltage cycle to gain mechanistic insights. The combination of XRD and EXAFS/XANES analysis during charge/discharge of a Ge/Li battery allows for the identification of reaction mechanisms in this inorganic electrical energy storage system. Our analysis revealed that amorphous regions within germanium nanowires are preferentially lithiated before crystalline regions. Within the scope of this work, limiting the cell discharge depth or current density avoids full lithiation but maintains some degree of crystallinity in the nanowires.

## REFERENCES

1. Chan, C. K.; Zhang, X. F.; Cui, Y. *Nano Lett.* **2008**, *8*, 307-309.
2. Morin, F. J.; Reiss, H. *J. Phys. Chem. Solids* **1957**, *3*, 196–209.
3. Calzecchi, F.; Gondi, P. *J. Appl. Phys.* **1971**, *42*, 4718-4723.
4. Carter, J. R.; Swalin, R. A. *J. Appl. Phys.* **1960**, *31*, 1191-1200.
5. St. John, M. R.; Furgala, A. J.; Sammells, A. F. *J. Electrochem. Soc.* **1982**, *129*, 246-250.
6. Key, B.; Morcrette, M.; Tarascon, J.-M.; Grey, C. P. *J. Am. Chem. Soc.* **2010**, *133*, 503–512.
7. Fuller, C. S.; Severiens, J. C. *Phys. Rev.* **1954**, *96*, 21-25s.
8. Baggetto, L.; Notten, P. H. L. *J. Electrochem. Soc.* **2009**, *156*, A169-A175.
9. Baggetto, L.; Hensen, E. J. M.; Notten, P. H. L. *Electrochim. Acta* **2010**, *55*, 7074-7079.
10. Lim, L.; Liu, N.; Cui, Y.; Toney, M. *Chem. Mater.* **2014**, *26*, 3739-3746.
11. Graetz, J.; Ahn, C. C.; Yazami, R.; Fultz, B. *J. Electrochem. Soc.* **2004**, *151*, A698-A702.
12. Seo, M.-H.; Park, M.; Lee, K. T.; Kim, K.; Kim, J.; Cho, J. *Energy Environ. Sci.* **2011**, *4*, 425-428.
13. Liu, X.; Huang, S.; Picraux, S.; Li, J.; Zhu, T.; Huang, J. Y. *Nano Lett.* **2011**, *11*, 3991-3997.
14. Chockla, A. M.; Klavetter, K. C.; Mullins, C. B.; Korgel, B. A. *ACS Appl. Mater. Interfaces* **2012**, *4*, 4658–4664.
15. Seng, K.; Park, M.; Guo, Z.; Liu, H.; Cho, J. *Nano Lett.* **2013**, *1236*, 2–8.
16. Mullane, E.; Kennedy, T.; Geaney, H.; Dickinson, C.; Ryan, K. M. *Chem. Mater.* **2013**, *25*, 1816–1822.
17. Kim, H.; Son, Y.; Park, C.; Cho, J.; Choi, H. C. *Angew. Chem. Int. Ed.* **2013**, *52*, 5997–6001.

- 
18. Sayers, D.; Stern, E.; Lytle, F. *Phys. Rev. Lett.* **1971**, *27*, 1204-1207.
  19. Ward, M. J.; Rugar, P. A; Murphy, M. W.; Yiu, Y.-M.; Baines, K. M.; Sham, T. K. *Chem. Commun.* **2010**, *46*, 7016–7018.
  20. Lucovsky, G.; Washington, J. P.; Miotti, L.; Paesler, M. *Phys. Status Solidi C* **2010**, *7*, 844-847.
  21. Bertini, L.; Ghigna, P.; Scavini, M.; Cargnoni, F. *Phys. Chem. Chem. Phys.* **2003**, *5*, 1451–1456.
  22. Hanrath, T.; Korgel, B. A. *J. Am. Chem. Soc.* **2002**, *124*, 1424-1429.
  23. Schlecht, S.; Yosef, M.; Fröba, M. *Z. Anorg. Allg. Chem.* **2004**, *630*, 864–868
  24. Hammersley, A. P.; Svensson, S. O.; Hanfland, M.; Fitch, A. N.; Häusermann, D. *High Pressure Res.*, **1996**, *14*, 235–248.
  25. Bish, D. L.; Howard, S. A. *J. Appl. Crystallogr.* **1988**, *21*, 86–91.
  26. Toby, B. H. *J. Appl. Cryst.* **2001**, *34*, 210-213.
  27. Sangster, J.; Pelton, A. D. *J. Phase Equilibria* **1997**, *18*, 289-294.
  28. Ravel, B.; Newville, M. *J. Synchrotron Rad.* **2005**, *12*, 537-541.
  29. Dalba, G.; Fornasini, P.; Grisenti, R.; Rocca, F.; Chambouleyron, I.; Graeff, C. F. *O. J. Phys: Condens. Matter* **1997**, *9*, 5875-5888.

## CHAPTER 6

# EXPERIMENTAL AND CALCULATED X-RAY ABSORPTION ANALYSIS OF LITHIUM-SULFUR SPECIES TO SUPPORT *OPERANDO* STUDIES

### 6-1. Introduction

As a positive electrode (cathode) material in LIBs, sulfur has been touted as highly promising. (Some call it seductive!) The theoretical capacity, as derived from the full 16-electron reduction from elemental sulfur ( $S_8$ ) to lithium sulfide ( $Li_2S$ ), is 1,672 mAh/g. However, researchers have been unable to attain this high capacity reversibly, and much work has gone into developing methodologies to improve performance<sup>1</sup>.

As is often the case in the Abruña lab, we focused on gaining a fundamental understanding of the electrochemical reaction mechanisms of  $S_8$  with lithium<sup>2</sup> with the intent of motivating rational developments in the control of chemical equilibria. Through *operando* XANES measurements, systematic changes in the X-ray absorption spectra were observed, but without known standards at the time of the study, more concrete assignments of specific polysulfide species to spectral features could not be obtained. In support of this previous *operando* work, I undertook the tasks of collecting spectra of sulfur-lithium “standards” and calculating absorption spectra of proposed polysulfide species via the quantum chemistry package ORCA. These studies were intended to give a more concrete basis for the description of

spectroscopic observations from the effects that different cell parameters (e.g. electrolyte composition<sup>3</sup>, cathode matrix structure<sup>4</sup>) had on chemical equilibria of lithium-sulfur battery systems.

## 6-2. Experimental Details

*6-2-1. XANES measurements.* Due to the low energy of the sulfur K-edge (2.472keV), measurements were carried out at the 9-BM-B station of the Advanced Photon Source (APS) at Argonne National Laboratory. Data were collected in a He-purged chamber to reduce air scatter via the total electron yield (TEY) method in order to decrease self-absorption effects<sup>5</sup>. 3 to 5 scans were taken per sample and averaged to reduce noise. Proportions of Li<sub>2</sub>S and S<sub>8</sub> were mixed to give nominal samples of Li<sub>2</sub>S<sub>2</sub>, Li<sub>2</sub>S<sub>3</sub>, Li<sub>2</sub>S<sub>4</sub>, and Li<sub>2</sub>S<sub>8</sub>, both as powders heated in glass tubes and 1M viscous solutions in tetraethylene glycol dimethyl ether (TEGDME), as well as powders of S<sub>8</sub> and Li<sub>2</sub>S. Each powder and solution was dispersed on sulfur-free adhesive copper tape and sealed in the TEY cell in an argon-filled glove box prior to data collection. XANES spectra were collected from -10 to +25 eV around the sulfur K-edge.

*6-2-2. ORCA calculations.* Single-point and K-edge excitation calculations were carried out in ORCA<sup>6</sup>. Sample input files are given in Section 2-3-3. The molecular structures of the various polysulfide mono- and dianions most likely to be present in solution were determined by Kathleen Schwarz in the Arias group and were used in

the ORCA calculations. Since there were multiple symmetry-related sulfur sites in the structures, orbitals had to be localized to remove artifacts from the calculation<sup>7</sup>. The results were output as a series of intensity versus energy points. Without relativistic corrections, the BP86 functional used in these calculations leads to a systematic offset in the calculated peak positions by about 76eV<sup>7</sup>. The energy correction was applied to make the comparison to experimental data more apparent in a graphical plot.

### 6-3. Results

*6-3-1. XANES measurements.* By eye, the solid powder samples looked like binary mixtures, and the collected XANES spectra confirmed this (Figure 6-1). The spectra of the different mixtures appeared as a linear combination of the Li<sub>2</sub>S and S<sub>8</sub> spectra, based on the proportions present in the sample. It is possible that Li<sub>2</sub>S powder was partially hydrolyzed by contact with air, since we could smell H<sub>2</sub>S and the peak at 2482 eV has been attributed to sulfate (SO<sub>4</sub><sup>2-</sup>)<sup>8</sup>. The mixed powder samples, therefore, were not accurate standards for the sulfur species present in *operando* studies.

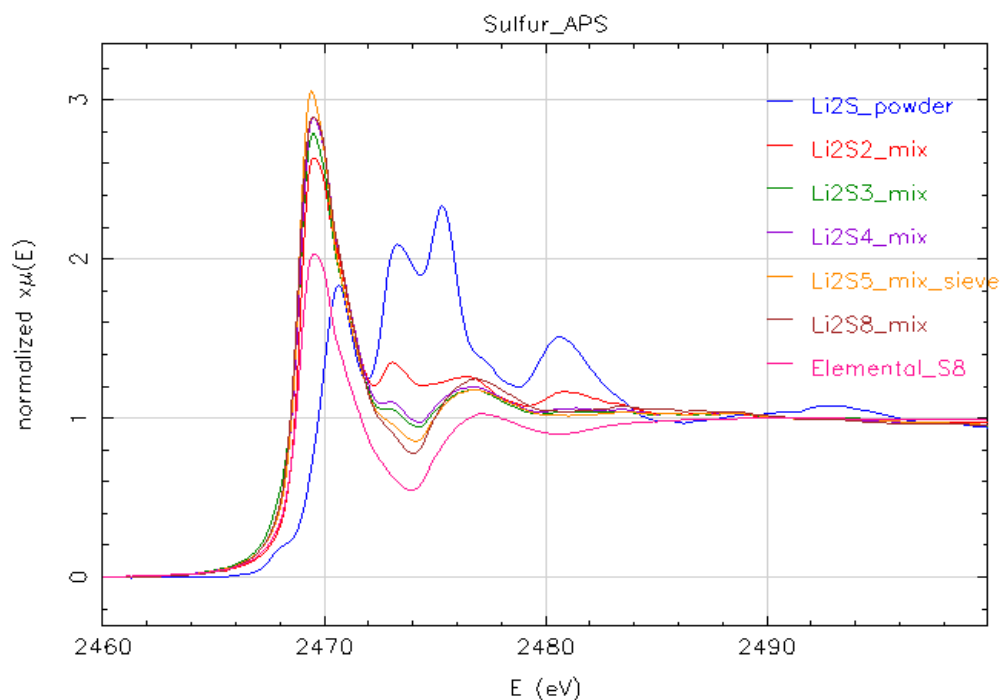


**Figure 6-1:** XANES spectra of binary mixtures of  $\text{Li}_2\text{S}$  and  $\text{S}_8$  powders.

When the various mixtures were dissolved in TEGDME, the spectral features were more similar to what was observed in *operando* measurements. This is not surprising since the intermediate species are assumed to be soluble polysulfides in the electrolyte. Equilibration into multiple polysulfide species in solution is highly likely<sup>9</sup>, so our “standards” were still mixtures, albeit more representative than the powders of what would be seen in a real battery.

As the proportion of lithium to sulfur increased (as in a battery discharge), the normalized main peak intensity decreased. Since the white line peak in sulfur K-edge absorption spectroscopy is generally attributed to the  $1s \rightarrow 3p$  transition<sup>10</sup>, the relative loss of intensity is in support of smaller-chain polysulfides dominating the solution composition. Also, a prepeak arose that was taller (proportionally to the main peak) at

longer nominal polysulfide chain length (higher polysulfide). Based on the observations in the *operando* work, it was proposed that long-chain polysulfides dissociate into electroactive  $S_3^-$  during the second discharge plateau<sup>2</sup>. Peaks at higher energy grew in for the solutions with lower sulfide concentrations, which could be attributed to residual  $Li_2S$  powder or isolated small-chain polysulfides.

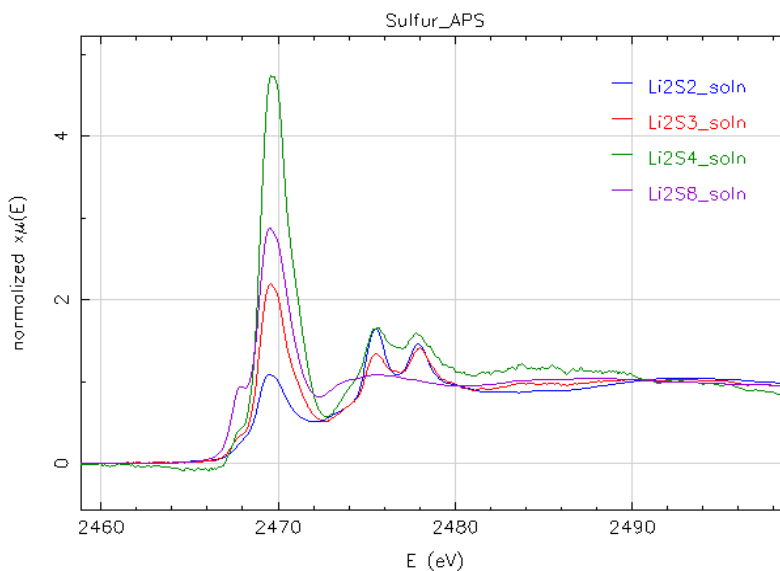


**Figure 6-2:** XANES spectra of 1M mixtures of  $Li_2S$  and  $S_8$  powders in TEGDME.

6-3-2. *Calculations.* Since the ORCA calculations were performed on individual anionic polysulfide species, they should be considered more representative of a single species. There is some peak splitting if the species is monoanionic instead of dianionic (Figure 6-3). The prepeak that arises during cycling, therefore, is likely from  $S_2^-$  or  $S_3^-$ . The peaks at higher energy (2476eV) arise at low voltages in the *operando* studies and at low polysulfide concentration ex-situ, indicating that  $S_2^-$  and  $S_2^{2-}$  are likely contributing to the spectra (Figure 6-3A).

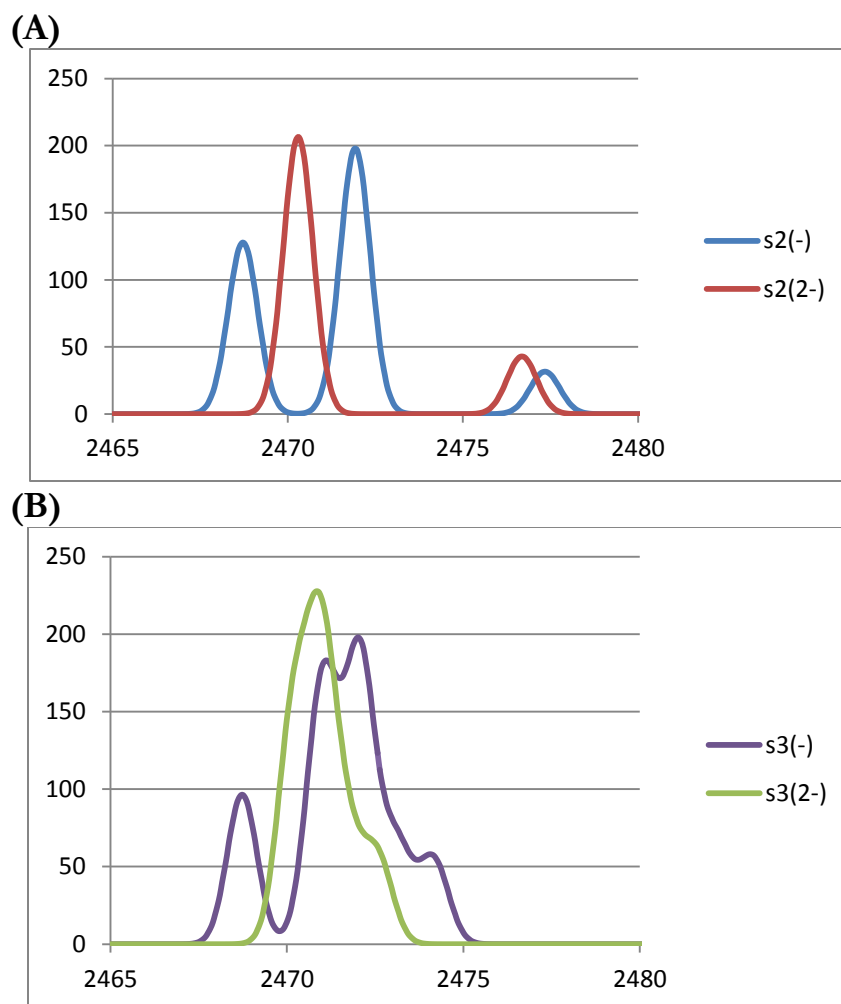


**Figure 6-3:** (A) Calculated XANES spectra of  $S_2^-$  (blue)  $S_2^{2-}$  (red), (B)  $S_3^-$  (green), and  $S_3^{2-}$  (purple) species.

The longer the polysulfide chain, the higher the energy of the main peak in the XANES (Figure 6-4). This was not resolvable in the “standards” spectra, but it is evident in the *operando* measurements<sup>2</sup>. Also, the longer polysulfide chains have a higher white line intensity, in accordance with experiment. Calculations were limited to these species not only for ease of analysis, but also because they were predicted to be the main contributors to spectral features.

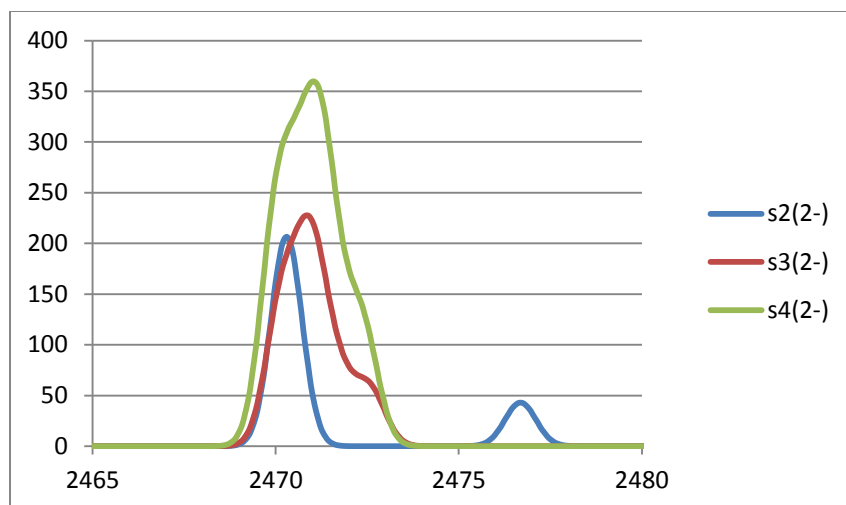


**Figure 6-4:** Calculated XANES spectra of the  $S_2^{2-}$  (blue),  $S_3^{2-}$  (red), and  $S_4^{2-}$  (green) species.

### 6-3. Discussion

After this study was performed, Nazar et al. used the more stable sodium polysulfides,  $Na_2S_2$  and  $Na_2S_4$ , as standards, and performed linear combination fitting of the resultant XANES spectra to tease out the intermediate polysulfide phases that arise during cycling<sup>10</sup>. They did not attribute any features to  $S_3^-$  because they did not have a corresponding standard, but our results seemed to support its existence during cycling. Both *operando* XANES studies referenced here raise interesting and complementary points about the reaction mechanisms within a Li-S battery. However, the full story still remains elusive.

The subtlety of the shifts, both computationally and experimentally, leads to the inability of concrete spectral resolution at this moment in time. Though XANES

measurements have chemical specificity, the likelihood that multiple polysulfide species are present concurrently within an operational battery precludes full assignment of each peak to a distinct chemical species.

#### **6-4. Conclusions**

Through this work, I gained experience in computational methods for determining XANES spectra. ORCA should be more widely implemented to predict XANES shifts and peak shapes that arise in *operando* battery measurements. As was also noted in Chapter 4, sample preparation is also extremely important if one is aiming to collect representative datasets. In future, well-informed work is to be conducted on the impact of cathode architecture on sulfur reactions, more fundamental chemical investigation into the role of carbon mesostructure on polysulfide intermediates and products is required.

## REFERENCES

---

1. Fang, X.; Peng, H. *Small* **2015**, *11*, 1488–1511.
2. Lowe, M. A.; Gao, J.; Abruña, H. D. *RSC Adv.* **2014**, *4*, 18347.
3. Gao, J.; Lowe, M. A.; Kiya, Y.; Abruña, H. D. *J. Phys. Chem. C* **2011**, *115*, 25132–25137.
4. Werner, J. G.; Johnson, S. S.; Vijay, V.; Wiesner, U. *Chem. Mater.* **2015**, ASAP.
5. Jalilehvand, F. *Chem. Soc. Rev.* **2006**, *35*, 1256–1268.
6. F. Neese, *WIREs Comput. Mol. Sci.*, **2012**, *2*, 73–78.
7. George, S. D.; Neese, F. *Inorg. Chem.* **2010**, *49*, 1849–1853.
8. Pickering, I. J.; Prince, R. C.; Divers, T.; George, G. N. *FEBS Lett.* **1998**, *441*, 11–14.
9. Vijayakumar, M.; Govind, N.; Walter, E.; Burton, S. D.; Shukla, A.; Devaraj, A.; Xiao, J.; Liu, J.; Wang, C.; Karim, A.; Thevuthasan, S. *Phys. Chem. Chem. Phys.* **2014**, *16*, 10923–10932.
10. Cuisinier, M.; Cabelguen, P. E.; Evers, S.; He, G.; Kolbeck, M.; Garsuch, A.; Bolin, T.; Balasubramanian, M.; Nazar, L. F. *J. Phys. Chem. Lett.* **2013**, *4*, 3227–3232.

## CHAPTER 7

# APPLICATION OF X-RAY METHODS TO CHARACTERIZE ENERGY STORAGE MATERIALS IN GENERAL

### 7-1. Introduction

I entered the Abruña lab not even knowing how X-rays were generated or how they could be used to probe energy storage materials. Over the past five years, my work on my main projects on germanium and anthraquinone provided me the opportunity to gain a staggering amount of synchrotron experience. With each run, I became more skilled at preparing for beamtime, as well as at collecting and analyzing high-quality data. Herein, I will describe how I was able to apply the skills I learned in order to begin the study of other emergent energy storage materials and systems with powder XRD, to uncover subtleties that arose in XRD measurements, to gain experience in other X-ray techniques that were new to me, and to assist others with their electrochemical X-ray experiments.

### 7-2. Lithium Vanadium Oxide Insertion

Lithium vanadate ( $\text{Li}_3\text{VO}_4$ ) has been studied as an alternative anode material in LIBs<sup>1</sup>. Very stable cycling between 0.2-3.0V gave a capacity of nearly 300mAh/g for 25 cycles. Yi Shi, our collaborator, synthesized  $\text{Li}_3\text{VO}_4$  microboxes<sup>2</sup> and with them

was able to achieve greater than 350mAh/g for more than 50 cycles within the same voltage window. When the battery was cycled all the way to 0V versus Li, an extra 100mAh/g of capacity were gained. A conversion reaction was proposed as responsible:  $\text{Li}_3\text{VO}_4 + 2\text{Li} \leftrightarrow \text{LiVO}_2 + 2\text{Li}_2\text{O}$ .

We collected *operando* XRD at 0.1C for this material (Figure 7-1). We elected to try using the Pilatus 300K detector on a diffractometer arm to see if we could get improved peak resolution as compared to the GE area detector used in previous studies (Chapters 3 and 5). The data processing steps required in using the Pilatus 300K were somewhat cumbersome because Python code had to be written in order to stitch together all four detector positions and normalize each scan to its own incident flux. Therefore, the lines present in the *operando* plot indicate the incomplete compensation for each intensity variation during beam fills. Even so, we were able to see distinct evidence of phase transitions throughout cycling. The initial peaks from  $\text{Li}_3\text{VO}_4$  persisted through the first plateau at 0.75V versus Li, after which they began to fade. By the end of the second plateau at 0.5V, the parent  $\text{Li}_3\text{VO}_4$  peaks were gone and new peaks grew in. Below 0.2V, a third set of peaks grew in once the second set disappeared, and then upon subsequent cycling, the reaction toggled between the second and third peaks sets.

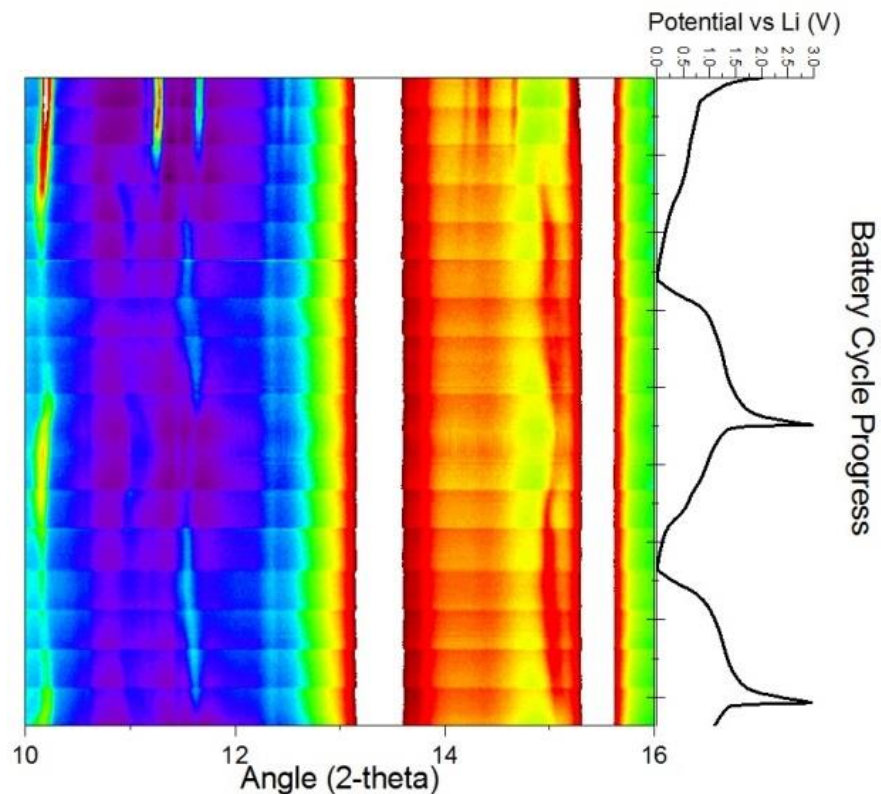


**Figure 7-1:** *Operando* XRD of  $\text{Li}_3\text{VO}_4$  battery cycling to 0V vs  $\text{Li}/\text{Li}^+$  at 0.1C.

When we cycled the battery at 1C, the initial peaks only shifted slightly in tandem with the output voltage (Figure 7-2). No new peaks developed. The lattice seemed to expand and contract in all directions equally at this faster C-rate. Also, it was easier to see that the overall background intensity increased during the end of the recharge plateau. This can also be observed in the organic work (Chapter 3). We believe the electrolyte has the most disorder at this point in the cycle, which would lead to higher diffuse scattering. Further investigations would be required to tease out the implications of this phenomenon.

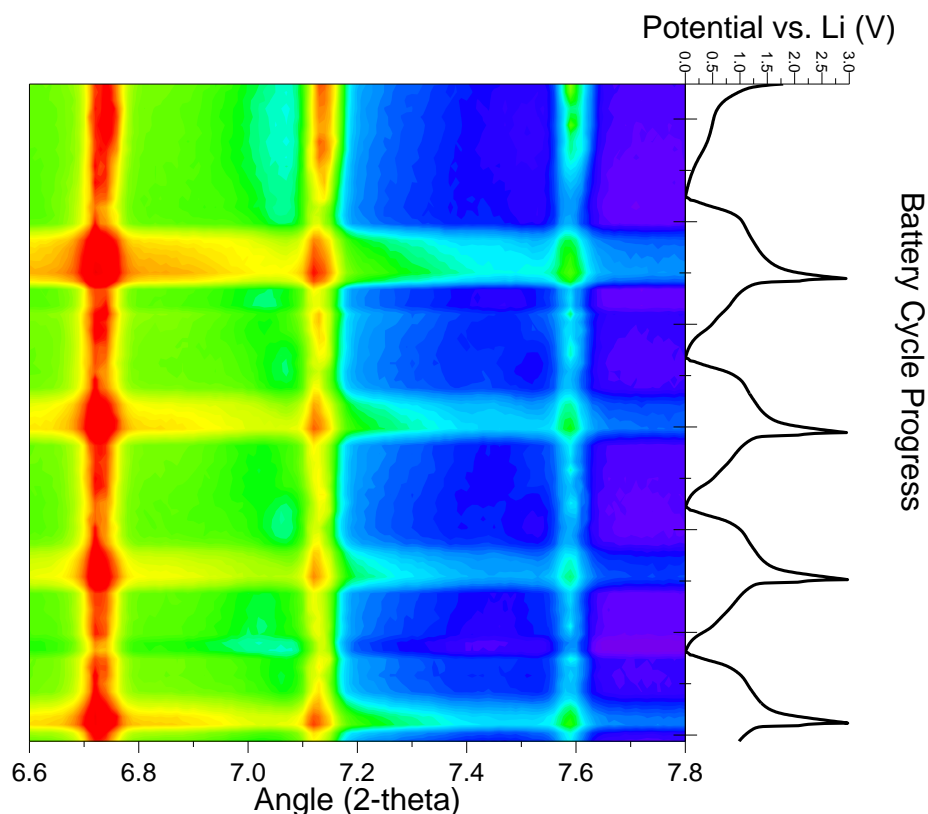


**Figure 7-2:** Zoomed-in region of *operando* XRD of  $\text{Li}_3\text{VO}_4$  battery cycled to 0V versus  $\text{Li}/\text{Li}^+$  at 1C.

We scoured the Inorganic Crystal Structure Database (ICSD), hunting for a lithiated vanadate phase that had the proper unit cell to fit the new peaks that were observed during the 0.1C cycling experiment. Unfortunately, we could not find a match, though we did uncover many possible vanadate phases for possible future investigation. When more powder XRD data were collected using the Pilatus 6M detector and applying a low voltage hold, however (Figure 7-3), we were able to isolate peak sets that corresponded to a c-axis lattice expansion of the original  $\text{Li}_3\text{VO}_4$  unit cell (Figure 7-4). The initial cell parameters (in Å),  $a = 6.33$   $b = 5.45$   $c = 4.96$ , changed to  $a = 6.31$   $b = 5.48$   $c = 5.15$  by the point of the low voltage hold.

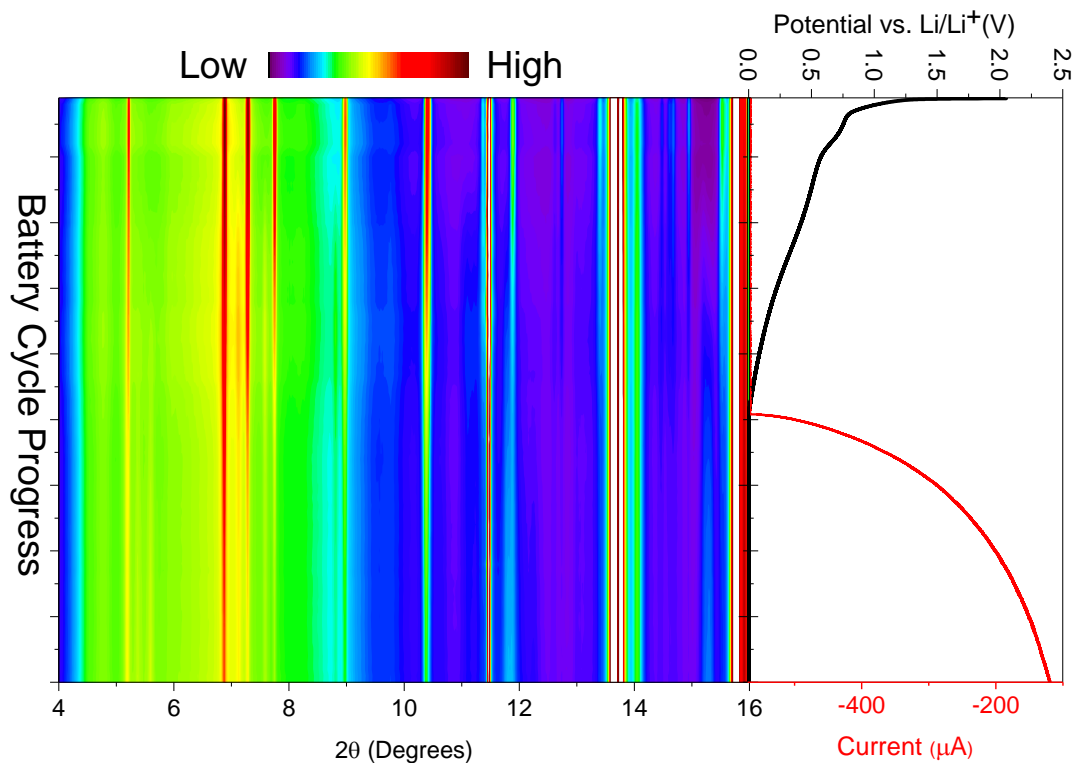


**Figure 7-3:** *Operando* XRD of  $\text{Li}_3\text{VO}_4$  discharged and then held at 0V versus Li.

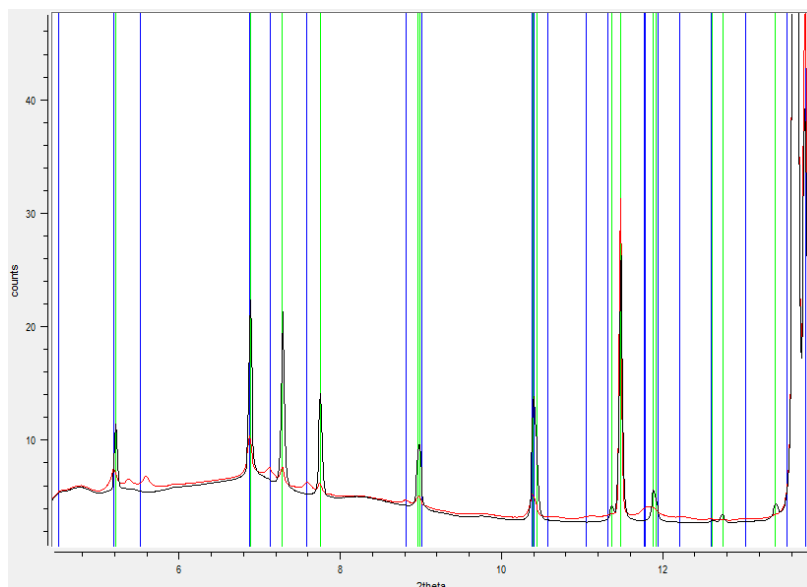


**Figure 7-4:** Peak assignment of the first (black pattern, green lines) and last (red pattern, blue lines) scan of Figure 7-3, based on the cell parameters reported above.

With these unit cells in hand, an insertion reaction, and a fairly reversible one at that, seemed to be the only reasonable explanation. None of the proposed lithiated vanadate structures fit as well as an expansion of the c-axis of the orthorhombic cell. The extra capacity below 0.2V merely came from being able to insert more lithium! It was only evident when we had the right detector, calibration, and level of expertise. Further work will be performed to track the full reaction mechanism, but at least by having the beginning and end points, the intermediate cell parameters should be easier to tease out. These results add a deeper understanding to what has recently come forward in the literature<sup>3</sup>. Not all peaks have been accounted for with this unit cell, so there is a possibility of side products. Though the peaks at 11 and 11.5° in Figure 7-2 toggled between each other upon cycling, we believe that this is preferential intercalation to a particular lattice plane at high and low voltages, respectively.

### **7-3. Cerium Dioxide Lattice Strain**

Work on  $\text{Li}_3\text{VO}_4$  (Section 7-2) and germanium (Chapter 5) led to my interest in determining why it appeared that the lattice parameters of current collector materials (copper, nickel) were changing in concert with the direction of current flow (Figure 7-5). The hypothesis was that the peak positions were shifting due to physical movement of current collector within coin cell, induced by flow of electrolyte, or expansion/contraction of electrode material. In order to test this hypothesis, I made

an electrode film out of  $\text{CeO}_2$  powder, a material used as calibrant for sample displacement in XRD measurements<sup>4</sup>.

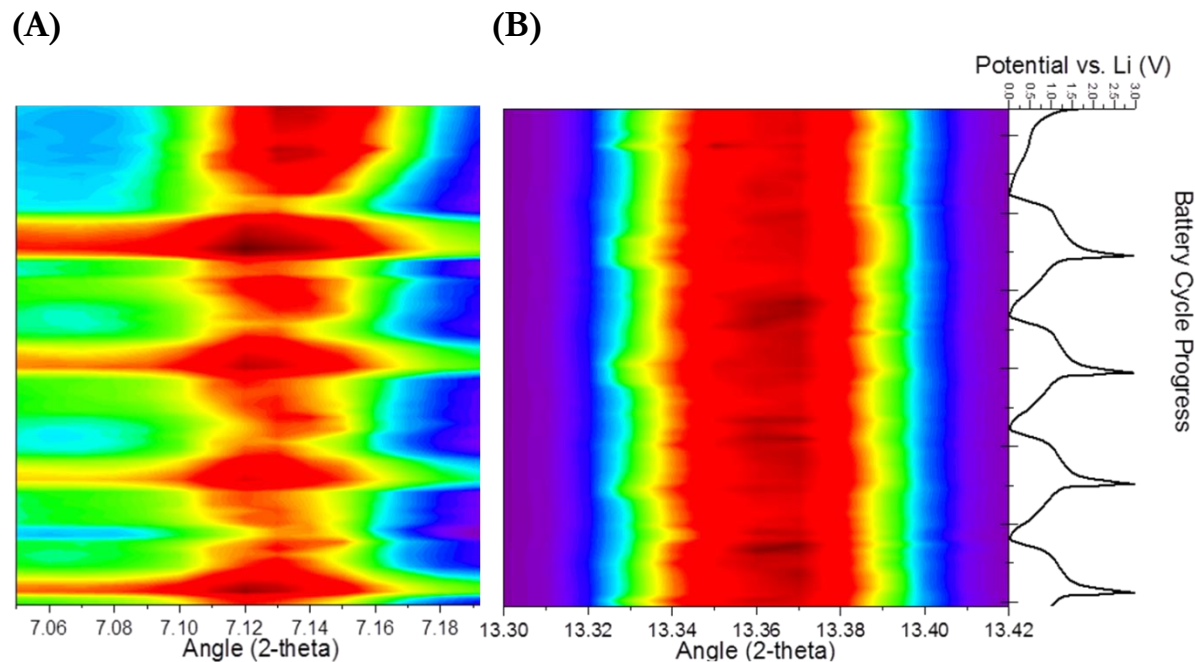


**Figure 7-5:** Shifts as a function of state-of-charge for **(A)** the  $\text{Li}_3\text{VO}_4$  (101) peak and **(B)** the Cu (111) peak.

There is some literature precedent for  $\text{CeO}_2$  battery work. It is used primarily as a coating for known metal oxide cathodes to enhance stability<sup>5,6,7,8</sup>. If used as the active material, ceria was nanostructured<sup>9</sup> or mixed with graphene<sup>10</sup>. The suggested conversion mechanisms seemed unreasonable:  $\text{CeO}_2 + 4\text{Li}^+ + 4\text{e}^- \leftrightarrow \text{Ce} + 2\text{Li}_2\text{O}^{11}$ ;  $2\text{CeO}_2 + 2\text{Li}^+ + 2\text{e}^- \leftrightarrow \text{Ce}_2\text{O}_3 + \text{Li}_2\text{O}^{10}$ . There had been no exploration of micron-scale crystallites, only “flower-like” microparticles with 9nm  $\text{CeO}_2$  “petals” for which the observed peak shift was attributed to a solid solution reaction<sup>12</sup>. I thought that the microparticles would be too large to be reactive towards lithium and therefore would

act as an internal standard for internal motion without much interference from bulk reactivity.

By carrying out *operando* XRD on a freestanding film of CeO<sub>2</sub> powder pressed on a copper foil, we saw that the copper and ceria main peaks shifted about .01° with cycling. We were surprised to find that ceria peaks broadened asymmetrically to the left, while the copper peaks did not (Figure 7-6). What appeared to be severely asymmetric peak broadening that could not be fully modeled by the Rietveld method turned out to be the growth of a new peak. By adding a significantly lattice-expanded CeO<sub>2</sub> phase that had the same peak positions as the fully shifted nano-CeO<sub>2</sub> in the literature<sup>12</sup> to the refinement, the goodness of fit improved considerably (Figure 7-7). Some small peaks grew in during cycling, but they did not match Ce metal or Ce<sub>2</sub>O<sub>3</sub>. The mechanism of CeO<sub>2</sub>'s reaction with lithium could then be considered to be a spinodal decomposition<sup>13</sup>, where most of the ceria particles remained unreacted while a small proportion was able to insert lithium.

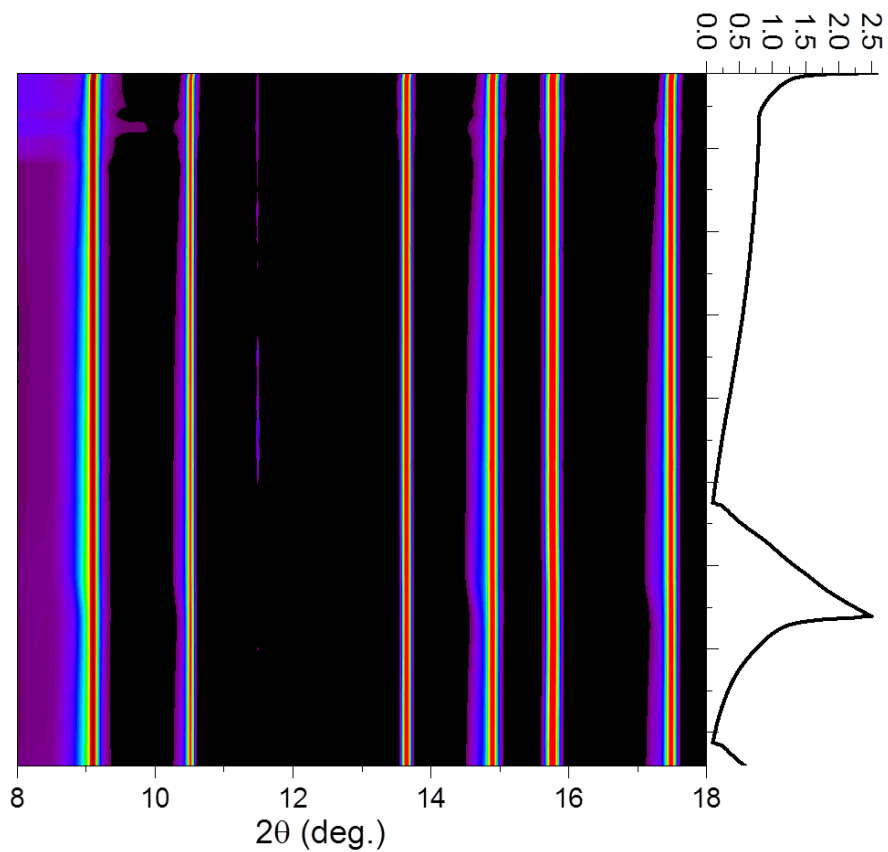


**Figure 7-6:** *Operando* XRD of  $\text{CeO}_2$  powder on copper foil.

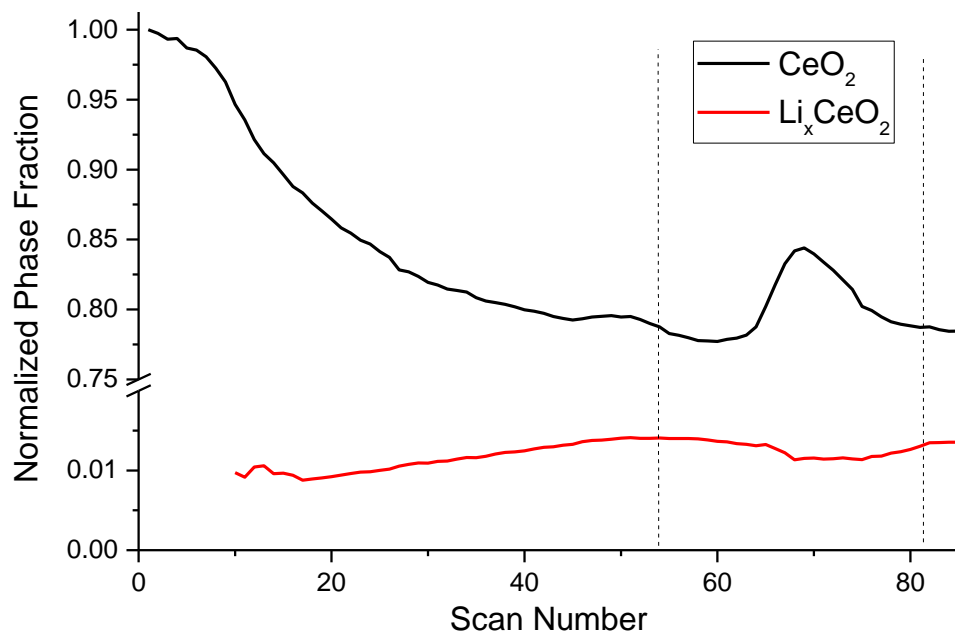


**Figure 7-7:** Sequential phase fraction analysis of  $\text{CeO}_2$  with lattice-expanded  $\text{Li}_x\text{CeO}_2$ .

What was intended to be a simple measurement to determine an accurate sample-to-detector distance, turned out to raise more questions than answers. It is still unclear just how far the current collector is moving under operating conditions because the calculations for sample displacement are based on a strict Debye-Scherrer transmission geometry<sup>14</sup>:

$$\Delta 2\theta = \frac{x \sin \theta - y \cos \theta}{R}$$

With this in mind, peak offsets that arise in *operando* XRD measurements must be considered carefully.

#### **7-4. Small-Angle X-ray Scattering of Ionomer Films**

Polymer electrolyte membranes are a defining component in low-temperature fuel cell technologies. Not only do the properties of the membrane enable fuel cells (e.g. reasonable room temperature ionic conductivity and limited transport of reactants), but the inherent membrane chemistry controls the chemistry of the fuel cell. For example, over the last several decades the standard membrane material has been a proton-conducting sulfonated fluoropolymer (Nafion), which has directed almost all significant research towards fuel cell components in highly acidic conditions. However, recent work from Professor Geoffrey Coates' lab has yielded a class of novel alkaline fuel cell membranes based on phosphonium<sup>15</sup>- and ammonium<sup>16</sup>-functionalized polyethylene that could enable fuel cell operation under

alkaline conditions. Many fuel cell components are more stable in alkaline conditions, and the faster kinetics of oxygen reduction and organic fuel oxidation may permit the use of non-precious metal electrocatalysts. Thus, the advent of alkaline anion exchange membranes (AAEMs) promises to redefine the basic material challenges and opportunities for low-temperature fuel cells.

The Coates AAEMs show greatly improved anionic conductivity when hydrated, but there is little fundamental research on how or why these changes occur. A mechanism similar to that of Nafion is proposed for the AAEMs: islands of clustered cations become interconnected by absorbed water to allow for ion transport. In the Nafion literature, the small-angle X-ray scattering (SAXS) feature that arises around  $Q=1\text{nm}^{-1}$  is attributed to anionic clusters and is termed the “ionomer peak”<sup>17</sup>. Ex-situ transmission SAXS patterns of dry membranes from the Coates group were collected on the rotating anode setup in the Gruner lab. A peak at  $Q=1$  and  $1.5\text{nm}^{-1}$  (corresponding to domains spaced at  $d=6$  and  $4\text{nm}$ ) arose in the scattering patterns for the phosphonium- and ammonium-based polymers, respectively (Figure 7-8).

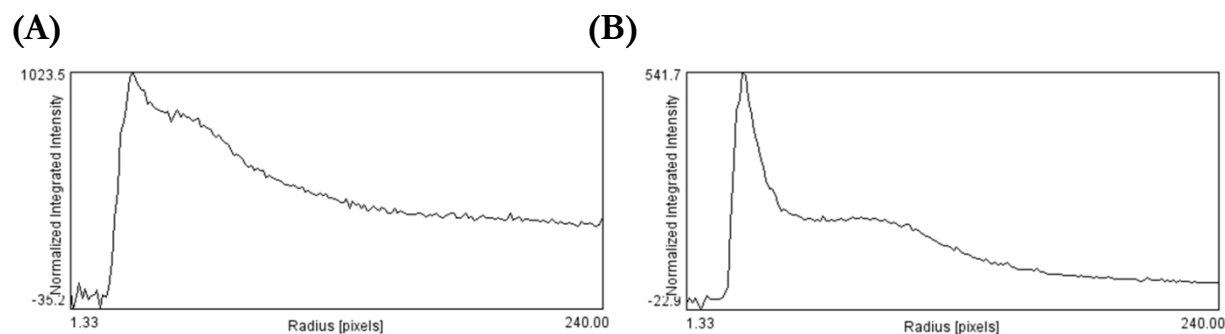


**Figure 7-8:** 1D plots of SAXS data from **(A)** phosphonium and **(B)** ammonium freestanding ionomer membranes.

For better resolution and faster data collection, we repeated the measurements of the freestanding films at CHESS. Small-angle X-ray scattering (SAXS) measurements were collected on a MedOptics fiber-coupled CCD camera area detector at the D1 station with an incident photon energy of 10.734 keV (1.155 Å). The freestanding membrane samples were mounted in a custom-made cell and data were collected in transmission mode. Measurements of ionomers spin-cast onto silicon wafers were carried out at grazing incidence (GISAXS) in a hydration chamber, a measurement that could only be carried out at CHESS. We examined phosphonium and ammonium ionomers, as well as Nafion as a control.

The phosphonium samples did not have well-defined “ionomer peaks”, but the ammonium and Nafion samples did (Figure 7-9). This might indicate that well-ordered microstructure is not essential for hydroxide conduction. It could also be that there was a lack of phase contrast between the cationic groups and the polymer backbone. For the ammonium polymer samples, the d-spacings ranged from 3-5 nm,

with the deliberately wetted sample having the highest d-spacing. As reported elsewhere<sup>17</sup>, the d-spacing increases in wet Nafion when compared to dry Nafion.

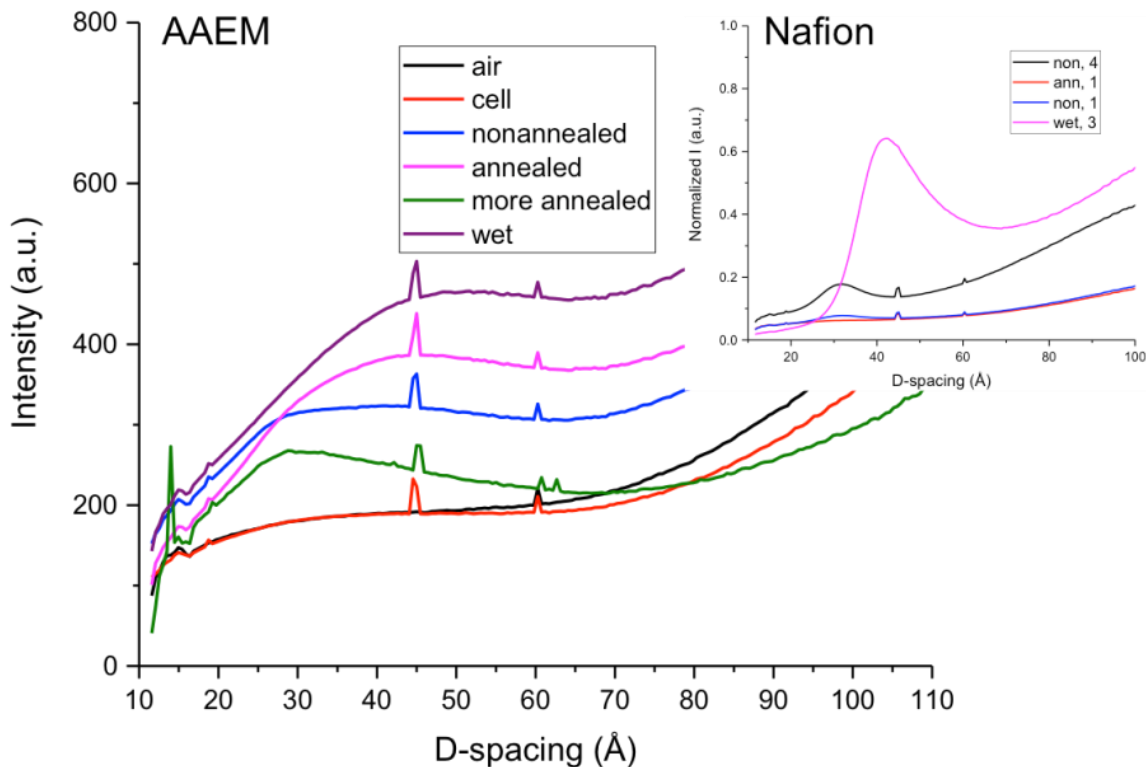


**Figure 7-9:** SAXS plots in d-spacing of freestanding membranes of ammonium ionomer and Nafion (inset) with differing pretreatments.

Within the hydration chamber, we were able to observe a slight decrease in  $Q$  of the ammonium as the film took up water. The change was much more dramatic in Nafion, perhaps because the domains ostensibly have a higher degree of ordering.

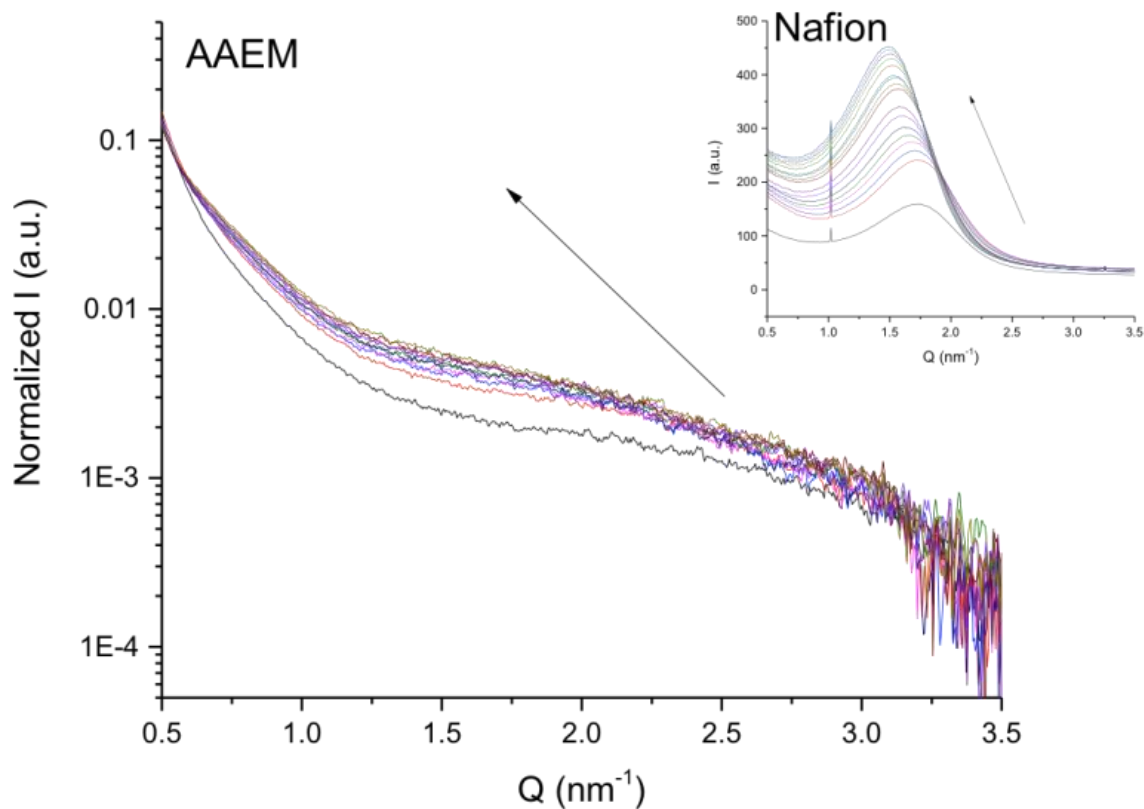


**Figure 7-10:** GISAXS plots, in Q-spacing, of *in situ* hydration of ionomer thin films of ammonium and Nafion (inset) as a function of increasing time/degree of water uptake.

These studies gave evidence of ordering in the ammonium microstructure on the same scale as that of Nafion, in spite of a different backbone. The ordered feature changed with hydration, which strongly suggests it is related to the conduction mechanism. There have been decades of research on the microstructure of Nafion, and still there is no consensus on the true structure<sup>18</sup>. For these new materials, it is worth collecting data to build a model that will guide modifications to improve performance.

## 7-5. Collaborative Synchrotron Efforts

Beyond all of the research in which I took the lead role, there were several projects to which I contributed my unique expertise in combining X-ray and electrochemical techniques. These include (in chronological order):

- In support of Dr. Deli Wang’s research: EXAFS measurements of Pd<sub>3</sub>Au, Cu<sub>3</sub>Au and Au-decorated PdCoCu nanoparticles for oxygen reduction reaction catalysis. A manuscript is forthcoming.
- With Dr. Michael Lowe: *operando* XAS of Li-S cells with different electrolytes (DOL:DME; TEGDME; with and without lithium nitrate additive); XANES of MnO-C composites from the Archer group; XRD of cycled Li-S cells from the startup company NOHMs to detect crystalline Li<sub>2</sub>S.
- In support of Kenneth Hernandez-Burgos and Xin Huang’s research, *in situ* grazing-incidence diffraction of Mg electrodeposition.
- In support of Dr. Jie Gao’s research, *operando* XRD of “VN”, which turned out to be (NH<sub>4</sub>)(VO)(V<sub>2</sub>O<sub>7</sub>).
- In support of James Pastore’s research, *operando* XRD and XAS of MnF<sub>2</sub> and NbN.
- In support of Prof. Fulvio of the University of Puerto Rico’s research, *in situ* SAXS/WAXS of ionic liquid (de)intercalation within carbon nanotube fabrics.

## REFERENCES

1. Li, H.; Liu, X.; Zhai, T.; Li, D.; Zhou, H. *Adv. Energy Mater.* **2013**, *3*, 428–432.
2. Shi, Y.; Wang, J. Z.; Chou, S. L.; Wexler, D.; Li, H. J.; Ozawa, K.; Liu, H. K.; Wu, Y. P. *Nano Lett.* **2013**, *13*, 4715–4720.
3. Liang, Z.; Lin, Z.; Zhao, Y.; Dong, Y.; Kuang, Q.; Lin, X.; Liu, X.; Yan, D. J. *Power Sources* **2015**, *274*, 345–354.
4. Hart, M. L.; Drakopoulos, M.; Reinhard, C.; Connolley, T. J. *Appl. Crystallogr.* **2013**, *46*, 1249–1260.
5. Minakshi, M.; Nallathamby, K.; Mitchell, D. R. G. *J. Alloys Compd.* **2009**, *479*, 87–90.
6. Kim, K.; Ha, H. W.; Yun, N. J.; Kim, M. H.; Woo, M. H. *Electrochim. Acta* **2006**, *51*, 3297–3302.
7. Ha, H. W.; Yun, N. J.; Kim, K. *Electrochim. Acta* **2007**, *52*, 3236–3241.
8. Liu, M.; Lin, C.; Gu, Y.; Yang, T.; Gong, Z.; Yin, G.; Gao, X.; Zhou, X.; Wen, W. *J. Phys. Chem. C* **2014**, *118*, 14711–14722.
9. Sasidharan, M.; Gunawardhana, N.; Yoshio, M.; Nakashima, K. *Chem. Lett.* **2012**, *41*, 386–388.
10. Su, Q.; Chang, L.; Zhang, J.; Du, G.; Xu, B. *J. Phys. Chem. C* **2013**, *117*, 4292–4298.
11. Pang, H.; Chen, C. *RSC Adv.* **2014**, *4*, 14872.
12. Hua, C.; Fang, X.; Yang, Z.; Gao, Y.; Wang, Z.; Chen, L. *Electrochem. Comm.* **2012**, *25*, 66–69.
13. Liu, H.; Strobridge, F. C.; Borkiewicz, O. J.; Wiaderek, K. M.; Chapman, K. W.; Chupas, P. J.; Grey, C. P. *Science* **2014**, *344*, 1252817.
14. McCusker, L. B.; Von Dreele, R. B.; Cox, D. E.; Louër, D.; Scardi, P. J. *Appl. Crystallogr.* **1999**, *32*, 36–50.

- 
15. Noonan, K. J. T.; Hugar, K. M.; Kostalik, H. A.; Lobkovsky, E. B.; Abruña, H. D.; Coates, G. W. *J. Am. Chem. Soc.* **2012**, *134*, 18161–18164.
16. Kostalik, H. A. IV.; Clark, T. J.; Robertson, N. J.; Mutolo, P. F.; Longo, J. M.; Abruña, H. D.; Coates, G. W. *Macromolecules* **2010**, *43*, 7147-7150.
17. Kim, M. H.; Glinka, C. J.; Grot, S. A.; Grot, W. G. *Macromolecules* **2006**, *39*, 4775–4787.
18. Gebel, G.; Diat, O. *Fuel Cells* **2005**, *5*, 261–276.

## CHAPTER 8

### CONCLUSIONS AND FUTURE WORK

Throughout this dissertation, I have made it clear how critical it is to investigate dynamic electrochemical systems in their working environment in order to better understand their charge storage mechanisms. There are a few conclusions I would like to draw from my work on the organic and inorganic materials, respectively, and some directions for future work for both. In particular, great effort should be put into computationally determining the lithiated crystal structure of organic cathode materials. Also, X-ray techniques can be expanded to gain even more chemical, structural and compositional information about materials for energy storage. In general, what I have presented here will serve to expand the use of different and exciting X-ray techniques to understand a wide and increasingly complex variety of electrochemical transformations.

#### **8-1. Organics**

It is critical that more is learned about how organic crystals store charge. My work showed that one must consider solid-state interactions when considering the viability of a candidate molecule. Our group studies several electroactive organic motifs computationally and experimentally, and it would be ideal if we could correlate crystal structure with electrochemical performance for our whole catalogue of

materials. In the organic battery community at large, focus should be put on understanding molecular crystal packing on a theoretical and practical level.

Also, I have used GISAXS to study variations in microstructure of ionomer films with incorporation of water. It would not be too large of a stretch to electropolymerize thin films of conducting polymers on flat substrates, and then monitor structural changes of the polymers under controlled potential or current. We would be able to gain deeper understanding of how the supercapacitor materials store charge based on microstructural observations.

## 8-2. Inorganics

Some preliminary work was conducted using X-ray emission spectroscopy (XES). We collected XES for  $\text{LiCoO}_2$  electrodes within coin cell batteries held at varying potentials: <4V, 4.2V, 4.6V, 4.9V. We expected to see shift in peak intensity and position, related to degree of oxidation and intermolecular distance.

Unfortunately, the data were very noisy and a clear trend was not readily apparent. Based on the progress we have made since then, the group is already working on a new project in which *operando* chemical changes in  $\text{LiFePO}_4$  are monitored via confocal X-ray fluorescence.

Also, I was able to determine that the endpoint of lithiated  $\text{Li}_3\text{VO}_4$  is lattice-expanded in the c-axis, not some new phase. Future work will determine the phase transformations throughout the entire cycle via sequential Rietveld refinement and

phase analysis to fit for the constantly changing lattice parameters. XAS measurements can also confirm our observations on  $\text{Li}_3\text{VO}_4$  as they did for germanium.

### 8-3. Publications

My personal and collaborative efforts at Cornell have led to the following publications:

1. DeBlase, C. R.; **Silberstein, K. E.**; Truong, T.; Abruña, H. D.; Dichtel, W. R.  $\beta$ -Ketoenamine-Linked Covalent Organic Frameworks Capable of Pseudocapacitive Energy Storage. *J. Am. Chem. Soc.* **2013**, *135*, 16821–1682.
2. **Silberstein, K. E.**; Lowe, M. A.; Richards, B.; Gao, J.; Hanrath, T.; Abruña, H. D. *Operando* X-Ray Scattering and Spectroscopic Analysis of Germanium Nanowire Anodes in Lithium-Ion Batteries. *Langmuir* **2015**, *31*, 2028-2035.
3. DeBlase, C. R.; Hernandez-Burgos, K.; **Silberstein, K. E.**; Rodriguez-Calero, G. G.; Bisbey, R. P.; Abruña, H. D.; Dichtel, W. R. Rapid and Efficient Redox Processes within 2D Covalent Organic Framework Thin Films *ACS Nano* **2015**, *9*, 3178-3183.